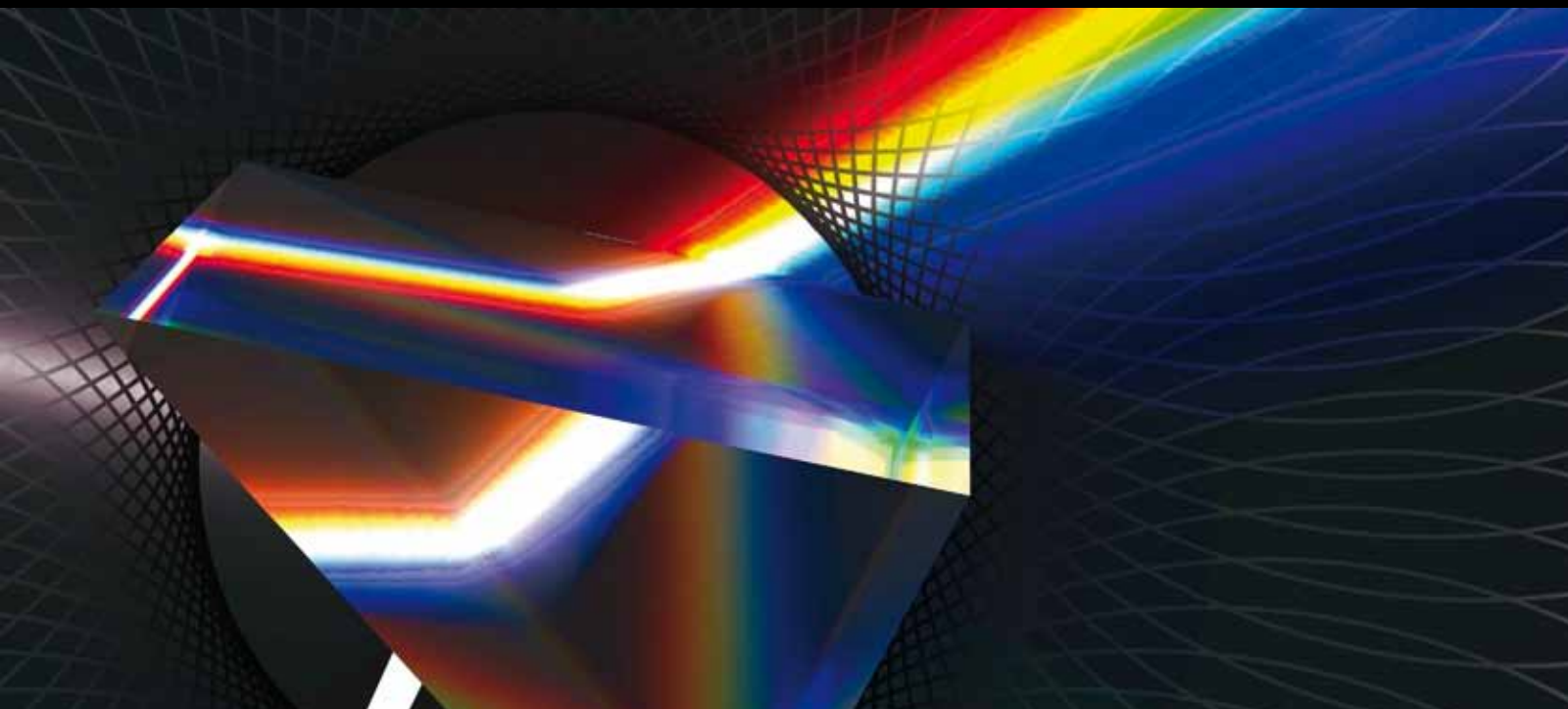


# ADVANCED TECHNIQUES IN BIOMEDICAL OPTICAL IMAGING

GUEST EDITORS: NANQUANG CHEN, BAOHONG YUAN, AND JAVIER A. JO





---

# **Advanced Techniques in Biomedical Optical Imaging**

International Journal of Optics

---

## **Advanced Techniques in Biomedical Optical Imaging**

Guest Editors: Nanguang Chen, Baohong Yuan,  
and Javier A. Jo



---

Copyright © 2012 Hindawi Publishing Corporation. All rights reserved.

This is a special issue published in “International Journal of Optics.” All articles are open access articles distributed under the Creative Commons Attribution License, which permits unrestricted use, distribution, and reproduction in any medium, provided the original work is properly cited.

## Editorial Board

Alejandro Aceves, USA  
Fortunato Tito Arcchi, Italy  
Victor Arrizon, Mexico  
Gaetano Assanto, Italy  
Jose Azana, Canada  
Ole Bang, Denmark  
Randy A. Bartels, USA  
Augusto Belendez, Spain  
E. Bernabeu, Spain  
Le Nguyen Binh, Germany  
Keith J. Blow, UK  
A. D. Boardman, UK  
Wojtek J. Bock, Canada  
Neil Broderick, UK  
Hrvoje Buljan, Croatia  
A. Cartaxo, Portugal  
Giulio Cerullo, Italy  
K. S. Chiang, Hong Kong  
W. C. H. Choy, Hong Kong  
David Coutts, Australia  
Ilaria Cristiani, Italy  
Michael J. Damzen, UK  
Vittorio Degiorgio, Italy  
Cornelia Denz, Germany  
Ivan Djordjevic, USA  
Niloy K. Dutta, USA  
Robert G. Elliman, Australia

Charles M. Falco, USA  
Mahmoud Fallahi, USA  
Pietro Ferraro, Italy  
Mário F. Ferreira, Portugal  
Rashid A. Ganeev, Uzbekistan  
Hooshang Ghafouri-Shiraz, UK  
Ivan Glesk, UK  
Qihuang Gong, China  
N. A. Halliwell, UK  
Sang-Kook Han, Republic of Korea  
Sulaiman Wadi Harun, Malaysia  
W. F. Hsieh, Taiwan  
Mark Humphrey, Australia  
Nicusor Iftimia, USA  
Mohammed N. Islam, USA  
Chennupati Jagadish, Australia  
Wonho Jhe, Korea  
Mirosław A. Karpierz, Poland  
Yu S. Kivshar, Australia  
Wieslaw Krolikowski, Australia  
Nayot Kurukitkoson, Thailand  
R. Leitgeb, Switzerland  
Gong Ru Lin, Taiwan  
Michael E. Marhic, UK  
Lorenzo Marrucci, Italy  
John McInerney, Ireland  
Andrea Melloni, Italy

Adam Miranowicz, Poland  
Roberto Morandotti, Canada  
Uwe Morgner, Germany  
Dragomir Neshev, Australia  
Jean-Michel Nunzi, Canada  
Takashige Omatsu, Japan  
Wolfgang Osten, Germany  
Ben Ovryn, USA  
Nicolae C. Panoiu, UK  
Vittorio M. N. Passaro, Italy  
Gang-Ding Peng, Australia  
Reji Philip, India  
Armando Nolasco Pinto, Portugal  
Adrian Podoleanu, UK  
Jianan Qu, Hong Kong  
Chenggen Quan, Singapore  
Marek Samoc, Poland  
John T. Sheridan, Ireland  
Ping Shum, Singapore  
Mohammad Taghizadeh, UK  
R. P. Tatam, UK  
Markus E. Testorf, USA  
Mustapha Tlidi, Belgium  
Stefano Trillo, Italy  
Stefan Wabnitz, Italy  
Boris Y. Zeldovich, USA

## Contents

**Advanced Techniques in Biomedical Optical Imaging**, Nanguang Chen, Baohong Yuan, and Javier A. Jo  
Volume 2012, Article ID 308628, 2 pages

**Diffuse Optical Imaging Using Decomposition Methods**, Binlin Wu, M. Alrubaiee, W. Cai, M. Xu,  
and S. K. Gayen  
Volume 2012, Article ID 185435, 12 pages

**Volumetric Diffuse Optical Tomography for Small Animals Using a CCD-Camera-Based Imaging System**, Zi-Jing Lin, Haijing Niu, Lin Li, and Hanli Liu  
Volume 2012, Article ID 276367, 10 pages

**Megavoltage X-Ray Imaging Based on Cerenkov Effect: A New Application of Optical Fibres to Radiation Therapy**, A. Teymurazyan and G. Pang  
Volume 2012, Article ID 724024, 13 pages

**Development of Automatic 3D Blood Vessel Search and Automatic Blood Sampling System by Using Hybrid Stereo-Autofocus Method**, Eiji Nakamachi, Yusuke Morita, and Yoshifumi Mizuno  
Volume 2012, Article ID 258626, 11 pages

**Effect of Fluorescent Particle Size on the Modulation Efficiency of Ultrasound-Modulated Fluorescence**, Yuan Liu, Baohong Yuan, and Joseph Vignola  
Volume 2012, Article ID 260709, 7 pages

**Multilayer Mie Scattering Model for Investigation of Intracellular Structural Changes in the Nucleolus and Cytoplasm**, S. Saltsberger, I. Steinberg, and I. Gannot  
Volume 2012, Article ID 947607, 9 pages

**Dual-Source Swept-Source Optical Coherence Tomography Reconstructed on Integrated Spectrum**, Shoude Chang, Youxin Mao, and Costel Flueraru  
Volume 2012, Article ID 565823, 6 pages

## Editorial

# Advanced Techniques in Biomedical Optical Imaging

Nanguang Chen,<sup>1</sup> Baohong Yuan,<sup>2</sup> and Javier A. Jo<sup>3</sup>

<sup>1</sup> Department of Bioengineering, National University of Singapore, 7 Engineering Drive 1, Singapore 117574

<sup>2</sup> Bioengineering Department, University of Texas at Arlington, 500 UTA BLVD, Arlington, TX 76010, USA

<sup>3</sup> Department of Biomedical Engineering, Texas A&M University, 3120 TAMU, College Station, TX 77843-3120, USA

Correspondence should be addressed to Nanguang Chen, [biecng@nus.edu.sg](mailto:biecng@nus.edu.sg)

Received 4 March 2012; Accepted 4 March 2012

Copyright © 2012 Nanguang Chen et al. This is an open access article distributed under the Creative Commons Attribution License, which permits unrestricted use, distribution, and reproduction in any medium, provided the original work is properly cited.

Numerous novel optical imaging techniques have been developed in the past decade for widespread basic biological research and clinical applications. While optical microscopy remains as an indispensable tool for high-resolution cellular or subcellular imaging, a larger imaging depth achieved with scattered light is becoming more and more attractive for noninvasive imaging of large human organs. For example, diffuse optical tomography (DOT) has been extensively investigated for potential applications in breast cancer detection, brain function study, and small animal whole-body imaging. Optical coherence tomography (OCT) is also one of hot research areas. Besides its successful application in ophthalmology, OCT is expected to play an increasingly important role in blood vessel evaluation and skin cancer diagnosis.

Four out of seven papers published in this special issue are related to optical imaging with scattered light. Image reconstruction is an integrated component of DOT. B. Wu et al. simplified the reconstruction process to a blind source separation (BSS) problem in their paper entitled “*Diffuse optical imaging using decomposition methods.*” Three matrix decomposition methods (Independent Component Analysis, Principal Component Analysis, and Nonnegative Matrix Factorization) were used to localize targets embedded in a turbid medium. The targets were considered as uncorrelated or independent virtual sources that led to perturbations in the detected diffusive light intensity. While these methods do not directly provide tomographic images, the high accuracy in localizing small heterogeneities may be valuable for detecting tumors in their early stages.

Z.-J. Lin et al. reported a CCD-based DOT system for volumetric imaging of small animals in their paper entitled “*Volumetric diffuse optical tomography for small animals using a CCD-camera-based imaging system.*” With a 12-bit CCD camera, the optical signal from regions up to 20 mm in

depth can be detected by pixel binning. In addition, a depth compensation algorithm is integrated in their system for improved image quality. Because of its simplicity, low-cost, and portability of such a system, a CCD-camera-based DOT may become a highly appropriate imaging tool for preclinical studies involving small animals. For example, their approach may be used to localize and evaluate tumors embedded in a small animal.

Diabetes is one of major global health problems, which affects almost one-fifth of the world population. Self-monitoring of blood glucose is critical for maintaining the health of diabetic patients. E. Nakamachi et al. developed a 3D blood vessel search system combined with an automatic blood sampling system, which were integrated into a point-of-care system for medical care in their paper entitled “*Development of automatic 3D blood vessel search and automatic blood sampling system by using hybrid stereo-autofocus method.*” They adopted the hybrid stereo-autofocus method to detect the 3D location of blood vessels. When detecting a 0.5 mm diameter blood vessel embedded in the depth range of 0.5–2.5 mm, the localization precision was 63  $\mu\text{m}$  on average. The combined system was evaluated with phantoms to demonstrate its potential in real medical applications.

Light scattering from biological cells has been used as a diagnostic tool for diseases in superficial tissues. Simulating the scattering process is very important for understanding and predicting the scattering patterns. S. Saltsberger et al. presented an analytical model of a multilayer spherical scattering cell in their paper entitled “*Multilayer Mie scattering model for investigation of intracellular structural changes in the nucleolus and cytoplasm.*” They developed and implemented a multilayer Mie-like model to treat the scattering of light from biological cells, whose internal structures are spherically symmetric. It was shown that the multilayer model provided

similar results as the finite-difference time-domain (FDTD) method, which is more computationally expensive.

Combining optical imaging with other image modalities, such as ultrasound, X-ray, and MRI, has attracted considerable interest recently. For example, the field of photoacoustic imaging has been growing rapidly in the past few years. Y. Liu et al. investigated a different approach to combine fluorescence imaging with ultrasound, which offers better penetration and spatial resolution in their paper entitled "*Effect of fluorescent particle size on the modulation efficiency of ultrasound-modulated fluorescence.*" They studied the effect of fluorescent particle size on the modulation depth of ultrasound modulated fluorescence. According to their results, there was a moderate twofold increase in the modulation depth when the fluorescent particle size increased from 5 nm to 1  $\mu\text{m}$ . The authors suggested that other approaches should be explored to significantly improve the modulation efficiency.

While the basic principle of optical coherence tomography (OCT) is straightforward, there is a continuous drive to search for the optimal implementations. Swept source optical coherence tomography is the proven choice of higher imaging speed and better sensitivity. S. Chang et al. proposed a method to reconstruct OCT images from the combined spectral data obtained from two swept sources in their paper entitled "*Dual-source swept-source optical coherence tomography reconstructed on integrated spectrum.*" It was demonstrated that their method resulted in OCT images with richer spectral and resolution information than any of the individually reconstructed OCT images. This method may be generalized for a swept source OCT system with multiple swept sources.

It is exciting to see that optical imaging methods start to play a role in radiation therapy, which uses Megavoltage (MV) X-ray beams to kill cancer cells. A critical issue in radiation therapy is how to guide the radiation dose towards the tumor while minimizing the harm to the surrounding normal tissues. A. Teymurazyan and G. Pang proposed a novel design of MV X-ray detectors for accurate locating the target in the treatment room before the start of radiation therapy in their paper entitled "*Megavoltage X-ray imaging based on Cerenkov effect: A new application of optical fibres to radiation therapy.*" Their design was based on the Cerenkov effect. The proposed detector consists of a matrix of optical fibres aligned with the incident X-rays and coupled to an active matrix flat panel imager (AMFPI) for image readout. X-ray energy absorbed in optical fibres is converted into visible light for improved detection sensitivity. Monte Carlo simulation was used to study imaging and dosimetric characteristics of such a detector. The simulation results showed that the proposed detector had a zero-frequency detection quantum efficiency more than an order of magnitude higher than that of current electronic portal imaging device (EPID) systems, while achieving a spatial resolution comparable to that of video-based EPIDs. The proposed detector is also less sensitive to scattered X-rays from patients than existing EPIDs.

Nanguang Chen  
Baohong Yuan  
Javier A. Jo

## Research Article

# Diffuse Optical Imaging Using Decomposition Methods

Binlin Wu,<sup>1</sup> M. Alrubaiee,<sup>1</sup> W. Cai,<sup>1</sup> M. Xu,<sup>2</sup> and S. K. Gayen<sup>1</sup>

<sup>1</sup>Department of Physics, The City College and The Graduate Center of The City University of New York, 160 Convent Avenue, New York, NY 10031, USA

<sup>2</sup>Department of Physics, Fairfield University, 1073 North Benson Road, Fairfield, CT 06824, USA

Correspondence should be addressed to Binlin Wu, bwu@sci.cuny.cuny.edu

Received 25 September 2011; Revised 5 December 2011; Accepted 8 December 2011

Academic Editor: Baohong Yuan

Copyright © 2012 Binlin Wu et al. This is an open access article distributed under the Creative Commons Attribution License, which permits unrestricted use, distribution, and reproduction in any medium, provided the original work is properly cited.

Diffuse optical imaging (DOI) for detecting and locating targets in a highly scattering turbid medium is treated as a blind source separation (BSS) problem. Three matrix decomposition methods, independent component analysis (ICA), principal component analysis (PCA), and nonnegative matrix factorization (NMF) were used to study the DOI problem. The efficacy of resulting approaches was evaluated and compared using simulated and experimental data. Samples used in the experiments included Intralipid-10% or Intralipid-20% suspension in water as the medium with absorptive or scattering targets embedded.

## 1. Introduction

Diffuse optical imaging (DOI) for detection and retrieval of location information of targets in a highly scattering turbid medium may be treated as a blind source separation (BSS) problem [1, 2]. Various matrix decomposition methods, such as, independent component analysis (ICA) [3], principal component analysis (PCA) [4], and nonnegative matrix factorization (NMF) [5, 6] have been developed for solving the BSS problem and retrieving desired information.

Xu et al. adapted ICA of information theory to develop optical tomography using independent component analysis (OPTICA) and demonstrated its application for diffuse imaging of absorptive, scattering, and fluorescent targets [7–11]. ICA assumes the signals from different targets to be *independent* of each other and optimizes a relevant measure of independence to obtain the ICs associated with different targets. The position coordinates of targets in three dimensions are determined from the individual components separately.

PCA assumes that the PCs contributing to the signal are *uncorrelated* and explain the most variance in the signal. PCA has been widely used in various applications, such as spectroscopy [12], face recognition [13], and neuroimaging [14]. NMF seeks to factorize a matrix into two nonnegative matrices (component signals and weights) and requires the

contributions to signal and the weights of the components to be *non-negative*. It does not imply any relationship between the components. NMF has also been widely used in biological analysis [15] and spectral analysis [16].

The objective of this study is to test and compare the efficacy of these algorithms when used to solve the DOI problem. Results are presented and compared using simulated data and experimental data using absorptive and scattering targets embedded in model scattering media. Our interest in solving the DOI problem derives from the need for a noninvasive modality for detecting, locating, and diagnosing breast tumors in early stages of growth.

The remainder of the paper is organized as follows. In Section 2, the formalisms of the three methods are introduced. Section 3 evaluates the resulting imaging approaches using simulated data. The approaches are further examined in Section 4 for experimental data acquired using absorptive and scattering targets embedded in model scattering media. Section 5 summarizes and discusses the results.

## 2. Formalism

**2.1. Blind Source Separation Problem.** Blind source separation (BSS), also known as blind signal separation, is a general problem in information theory that seeks to separate different individual signals from the measured signals, which

are weighted mixtures of those individual signals. Assuming  $M$  individual signals,  $s_j(t)$ ,  $j = 1, \dots, M$ , are linearly mixed instantaneously, the BSS problem is modeled as follows. The dimension of  $s_j(t)$  is  $N_s$ , the number of sampling times. In this study,  $t$  will be replaced by spatial positions of the excitation light sources. A total of  $N_d$  detectors sense  $N_d$  different mixtures of  $s_j(t)$ . The mixture measured by the  $i$ th detector can be presented as  $x_i(t) = \sum_{j=1}^M a_{ij}s_j(t)$ , or  $X = AS$ , in a matrix notation, where  $A \in R^{N_d \times M}$  is a mixing or weighting matrix,  $S \in R^{M \times N_s}$ ,  $X \in R^{N_d \times N_s}$ , and  $M < \min(N_s, N_d)$ . The objective of BSS is to retrieve the signals  $s_j(t)$  and their weights,  $a_{ij}$ . ICA, PCA, and NMF are statistical analysis methods used to solve the BSS problem.

**2.2. Diffuse Optical Imaging Problem.** In DOI, one measures the signal at the sample boundary, which includes a weighted mixture of contributions from embedded targets. One uses the diffusion approximation [17–19] of the radiative transfer equation [20, 21] as the forward model to describe light propagation in a highly scattering turbid medium. The perturbation in the light intensity distribution measured on the boundary of the sample due to the presence of the targets (which are localized inhomogeneities in the optical properties within the sample volume) may be written, in the first-order Born approximation, as [22, 23]

$$\Delta\phi(\mathbf{r}_d, \mathbf{r}_s) = - \int G(\mathbf{r}_d, \mathbf{r})\delta\mu_a(\mathbf{r})cG(\mathbf{r}, \mathbf{r}_s)d^3\mathbf{r} - \int \delta D(\mathbf{r})c\nabla_{\mathbf{r}}G(\mathbf{r}_d, \mathbf{r}) \cdot \nabla_{\mathbf{r}}G(\mathbf{r}, \mathbf{r}_s)d^3\mathbf{r}, \quad (1)$$

where  $\mathbf{r}_s$ ,  $\mathbf{r}_d$ , and  $\mathbf{r}$  are the positions of a source of unit power, detector and target, respectively;  $G(\mathbf{r}, \mathbf{r}_s)$  and  $G(\mathbf{r}_d, \mathbf{r})$  are the Green's functions that describe light propagation from the source to the target and from the target to the detector, respectively;  $\delta\mu_a$  and  $\delta D$  are the differences in absorption coefficient and diffusion coefficient between the targets and the background medium, respectively; and  $c$  is the light speed in the medium.

A multisource illumination and multidetector signal acquisition scheme is used to acquire light transmitted through a scattering medium. For small absorptive targets, a perturbation data matrix is constructed using  $-\Delta\phi$  for all sources. The elements of the data matrix pertaining to absorptive targets represented by the first term in (1) may be written in a discrete form as

$$X_{ij} = \sum_{m=1}^M G^d(\mathbf{r}_i, \mathbf{r}_m)\tau_m G^s(\mathbf{r}_m, \mathbf{r}_j) \quad (2)$$

$$(i = 1, 2, \dots, N_d; j = 1, 2, \dots, N_s),$$

where  $\mathbf{r}_i$ ,  $\mathbf{r}_j$ , and  $\mathbf{r}_m$  are the locations of the  $i$ th detector,  $j$ th source and  $m$ th target, respectively;  $N_s$ ,  $N_d$ , and  $M$  are the numbers of sources, detectors, and targets, respectively;  $\tau_m = \delta\mu_a(\mathbf{r}_m)c\delta V_m$  is the optical absorption strength of the  $m$ th target of volume  $\delta V_m$ ;  $G^s(\mathbf{r}_m, \mathbf{r}_j)$  and  $G^d(\mathbf{r}_i, \mathbf{r}_m)$  are the Green's functions that describe light propagation from  $j$ th source to  $m$ th target and from  $m$ th target to  $i$ th detector,

respectively. The number of targets is assumed to be less than that of sources and detectors,  $M < \min(N_d, N_s)$ .

The  $m$ th target may be considered to be a virtual source of strength  $\tau_m G^s(\mathbf{r}_m, \mathbf{r}_j)$  excited by the real light source located at  $\mathbf{r}_j$ . The data matrix  $X = \{X_{ij}\}$  may be considered to be a set of combinations of light signals from all virtual sources mixed by a mixing matrix  $\{G^d(\mathbf{r}_i, \mathbf{r}_m)\}$ . Therefore, this problem can be treated as a BSS problem.

As the second term in (1) suggests, each scattering target is represented by three collocated virtual sources of strength:  $\tau_m \partial_p G^s(\mathbf{r}_m, \mathbf{r}_j)$ , where  $\partial_p = \partial/\partial p$ , ( $p = x, y, z$ ), and  $\tau_m = \delta D(\mathbf{r}_m)c\delta V_m$ , is the optical scattering strength of the  $m$ th target [8]. The mixing matrices become  $\{\partial_p G^d(\mathbf{r}_i, \mathbf{r}_m)\}$  for the three virtual sources generated by the  $m$ th target. The elements of the data matrix for scattering targets may be written as

$$X_{ij} = \sum_{m=1}^M \sum_{p=\{x,y,z\}} \partial_p G^d(\mathbf{r}_i, \mathbf{r}_m)\tau_m \partial_p G^s(\mathbf{r}_m, \mathbf{r}_j). \quad (3)$$

Since one absorptive target is represented by one centrosymmetric virtual source, while three virtual sources (one centrosymmetric and two dumb-bell shaped) represent one scattering target [7, 8], the number and patterns of virtual sources may be used, in favorable situations, to identify the target as absorptive or scattering in nature. In this paper, only small targets are considered since all three algorithms are suited for small targets, and early detection, when the tumors are more amenable to treatment, is of practical interest.

**2.3. DOI as a BSS Problem.** The data matrix for the DOI problem may be written as

$$X = AS = \sum_{m=1}^M A_{im}S_{mj}, \quad (4)$$

where  $A \in R^{N_d \times M}$ ,  $S \in R^{M \times N_s}$ , and  $X \in R^{N_d \times N_s}$ . For absorptive targets,

$$A_{im} = \beta_m G^d(\mathbf{r}_i, \mathbf{r}_m), \quad S_{mj} = \alpha_m G^s(\mathbf{r}_m, \mathbf{r}_j), \quad (5a)$$

while for scattering targets,

$$A_{im} = \beta_m \partial_p G^d(\mathbf{r}_i, \mathbf{r}_m), \quad S_{mj} = \alpha_m \partial_p G^s(\mathbf{r}_m, \mathbf{r}_j). \quad (5b)$$

$\{S_{mj}\}$  ( $j = 1, 2, \dots, N_s$ ) and  $\{A_{im}\}$  ( $i = 1, 2, \dots, N_d$ ) are two-dimensional intensity distributions on the source and detector planes, respectively. Source and detector planes are the boundaries of the sample through which light enters and exits the sample volume, respectively. The scaling factors  $\beta_m$  and  $\alpha_m$  are related to the target optical strength,  $\tau_m = \alpha_m \beta_m$ .

The location of the target and the scaling factors can be retrieved using a least squares fitting via

$$\operatorname{argmin}_{\alpha_m, \beta_m, \mathbf{r}_m} \left\{ \sum_j \left[ \alpha_m^{-1} S_{mj} - G^s(\mathbf{r}_m, \mathbf{r}_j) \right]^2 + \sum_i \left[ \beta_m^{-1} A_{im} - G^d(\mathbf{r}_i, \mathbf{r}_m) \right]^2 \right\}, \text{ or} \quad (6a)$$

$$\operatorname{argmin}_{\alpha_m, \beta_m, \mathbf{r}_m} \left\{ \sum_p \left\{ \sum_j \left[ \alpha_m^{-1} S_{mj} - \partial_p G^s(\mathbf{r}_m, \mathbf{r}_j) \right]^2 + \sum_i \left[ \beta_m^{-1} A_{im} - \partial_p G^d(\mathbf{r}_i, \mathbf{r}_m) \right]^2 \right\} \right\}, \quad (6b)$$

for absorptive and scattering targets, respectively. However, when a scattering target is embedded deep in a turbid medium, only the  $\tau_m \partial_z G^s(\mathbf{r}_m, \mathbf{r}_j)$  virtual source remains significant. So, only  $p = z$  may be used for fitting in (6b) [8].

**2.3.1. ICA.** OPTICA assumes that the virtual sources are *independent* of each other [8]. So, they can be retrieved through an iterative process which seeks to maximize the independence among the components. In practice, the independent components are found by maximizing some measure of non-Gaussianity, such as kurtosis (the fourth-order cumulant), of the unmixed components. A Matlab program for ICA was adopted from <http://sccn.ucsd.edu/eeglab/>. The location of the target can be retrieved by fitting the independent component intensity distributions (ICIDs) to Green's functions or derivatives of Green's functions using (6a) and (6b).

**2.3.2. PCA.** PCA assumes that the virtual sources are uncorrelated so that the correlation (covariance) between them is ideally zero and minimal in practice. The covariance matrix of  $S$ ,  $\operatorname{cov}(S)$  should be diagonal. The general process of PCA is as follows. The data matrix  $X = AS + \mathcal{N}$ , where  $\mathcal{N}$  is random noise added to the data,  $A$  and  $S$  the same as defined in (4). When  $S$  is mean centered, elements of the mean-centered matrix  $S'$  are defined as

$$S'_{mj} = S_{mj} - \frac{1}{N_s} \sum_{j=1}^{N_s} S_{mj}. \quad (7a)$$

Similarly,

$$X'_{ij} = X_{ij} - \frac{1}{N_s} \sum_{j=1}^{N_s} X_{ij}. \quad (7b)$$

PCA looks for a matrix  $P$  that decomposes  $X$  into virtual sources,  $S = PX$ . It also holds that  $S' = PX'$ , since  $P$  is just a rotation matrix which does not change the center of the data.

$$\operatorname{cov}(S) = S' S'^T = (PX')(PX')^T = PX' X'^T P^T = \Lambda, \quad (8)$$

where  $\Lambda = \operatorname{diag}\{\lambda_1, \lambda_2, \dots\}$ . The eigenvalues  $\lambda_m$  are variances in the covariance matrix. Therefore,  $X' X'^T P^T = P^T \Lambda$ , where  $P^T$  is orthonormal. PCA is realized by eigenvalue decomposition (EVD) of the covariance matrix of  $X$ . The eigenvectors with leading eigenvalues (largest variances) are selected to be the PCs using the  $L$ -curve [24].

Since  $X = P^T S \approx AS$ ,  $A$  is determined as a matrix including only PCs.  $S$  is calculated as  $S \approx (A^T A)^{-1} A^T X$ . Rows of  $S$  and columns of  $A$  represent principal component intensity distributions (PCIDs) on the source plane and detector plane, respectively and are proportional to the images of the virtual sources projected on the source and detector planes. The target positions are determined using (6a) and (6b).

**2.3.3. NMF.** NMF is a group of multivariate analysis algorithms that factorize a matrix  $X$  into  $A$ , and  $S : X = AS$ ,  $A$  and  $S$  are nonnegative [6]. Unlike ICA and PCA, NMF does not imply any relationship between the retrieved components; instead, it just enforces non-negativity constraints on  $A$  and  $S$ . There are various algorithms developed to solve NMF, such as the multiplicative update method [5] and alternating least squares method [25, 26].

In the multiplicative update implementation of NMF,  $A$  and  $S$  can be found by minimizing the square of Euclidean distance  $\|X - AS\|^2$  as the cost function, where  $A \geq 0$  and  $S \geq 0$ , using the multiplicative update rule:

$$A_{ik} \leftarrow A_{ik} \frac{(XS^T)_{ik}}{(ASS^T)_{ik}}, \quad (9a)$$

$$S_{kj} \leftarrow S_{kj} \frac{(A^T X)_{kj}}{(A^T A S)_{kj}}. \quad (9b)$$

The alternating least squares implementation of NMF uses alternate least squares steps to estimate  $A$  (or  $S$ ), and use that estimate to optimize  $S$  (or  $A$ ), repeating the alternative steps until the desired optimization is obtained. Nonnegativity is ensured by setting any negative element of  $A$  or  $S$  equal to 0.

An NMF toolbox was obtained from <http://cogsys.imm.dtu.dk/toolbox/> to perform NMF computation. A built-in command *nmmf* is also available in Matlab (R2011a).

NMF algorithm requires that the non-negativity assumption must hold in the problem. In particular, for absorptive targets, when  $X$  is constructed with  $-\Delta\phi$ ,  $\tau_m$  should be positive, that is, the targets should be more absorbing than the background. If the targets have weaker attenuation properties than the background,  $X$  needs to be constructed with  $+\Delta\phi$  instead. For scattering targets,  $X$  should be treated similarly to keep its elements positive.

When NMF is applied to a scattering target, only the centrosymmetric component shows up properly, since the other two components have dumb-bell shape which includes negative values [8]. So without any prior knowledge or some other experimental means to assess if the target is absorptive or scattering, NMF may not distinguish between the two possibilities.

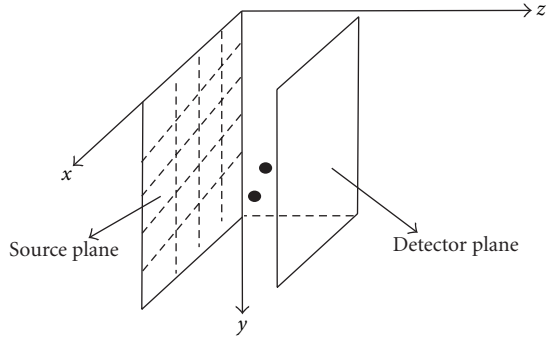


FIGURE 1: Light intensity distribution on the detector plane is recorded when a point source scans on the source plane.

The decomposition methods can be applied with different sample geometries such as slab and cylindrical geometries, and different measurement domains such as time-resolved domain, frequency domain, and continuous wave (CW). In this paper, Green's functions for slab geometry [23] with CW measurement were used for simulation and experiments.

### 3. Simulation

The sample was considered to be a 40 mm thick uniform scattering slab with lateral dimension of 80 mm  $\times$  80 mm, as shown in Figure 1. Its absorption and diffusion coefficients were taken to be  $\mu_a = 0.003 \text{ mm}^{-1}$  and  $D = 1/3 \text{ mm}$  (transport mean free path,  $l_t = 1 \text{ mm}$ ), respectively, which are similar to the average value of those parameters for human breast tissue. An absorptive and a scattering point targets were placed at (50, 60, 15) mm and (30, 30, 25) mm, respectively. The index of refraction  $n$  of the medium was taken to be 1.33. The speed of light is  $2.998 \times 10^8 \text{ m/s}$  or 299.8 mm/ns in vacuum, and 225.4 mm/ns in the medium. The absorption coefficient of the absorptive target was set to be higher than the background with  $\Delta\mu_a = 0.001 \text{ mm}^{-1}$ , while the diffusion coefficient was taken to be the same as that of background. The diffusion coefficient of the scattering target was set to be lower than the background (higher scattering coefficient) with  $\Delta D = -0.1 \text{ mm}$  ( $l_t = 0.7 \text{ mm}$ ), while the absorption coefficient was taken to be the same as that of the background. The volumes of both targets are set to be  $8 \text{ mm}^3$ . The optical strengths of the absorptive and scattering targets were  $\Delta\mu_a c \Delta V = 1.803 \text{ mm}^3/\text{ns}$  and  $\Delta D c \Delta V = -180.3 \text{ mm}^5/\text{ns}$ , respectively. The incident CW beam step scanned the sample at  $21 \times 21$  grid points covering an  $80 \times 80 \text{ mm}^2$  area, with a step size of 4 mm. Light on the opposite side was recorded at  $41 \times 41$  grid points covering the same area. Multiplicative Gaussian noise of 5% was added to the simulated data. The data matrix  $X$  was then obtained using (2) and (3) directly and analyzed using the three different algorithms.

**3.1. ICA Analysis.** One independent component for the absorptive target and three independent components for the scattering target were retrieved by ICA. The independent component intensity distributions (ICIDs) on the detector

plane are shown in Figures 2(a), 2(c), 2(d), and 2(e). Similar ICIDs were obtained on the source plane. Figure 2(g) shows the centrosymmetric ICID for the scattering target, and Figure 2(i) shows the ICID for the absorptive target, on the source plane.

The components in either the detector plane or the source plane can, in principle, be used to extract position and optical strength of the target(s). However, in our experimental arrangement signal is collected by a  $1024 \times 1024$  pixels CCD camera, while the source plane is scanned in an  $x$ - $y$  array of points, which is much smaller than the number of pixels in the CCD camera. Consequently, the resolution in the detector plane is much better, and the data set more robust than the source side. So, we used the images on the detector plane for retrieving target information using experimental data. While it would not matter in simulation, to be consistent with experimental situations, we employed detector plane images when using simulated data as well for all three algorithms. Table 1 lists the locations and strengths of the absorptive and scattering targets retrieved by fitting the spatial intensity profile of the centrosymmetric components on the detector plane to Green's functions and derivatives of Green's functions using (6a) and (6b), respectively, as shown in Figures 2(b) and 2(f). Figures 2(h) and 2(j) show the corresponding fits to the profiles on the source plane.

**3.2. PCA Analysis.** Eigenvalue equation of the covariance matrix of  $X$  was solved. The eigenvalues found by PCA were sorted in a descending order. Figure 3 shows a plot of leading 20 eigenvalues on a logarithmic scale.

First four leading eigenvalues were selected for PCs. The corresponding PCIDs were calculated. The PCIDs on the detector plane are shown in Figure 4. Similar images for PCIDs on the source plane were obtained. The scattering target has one centrosymmetric (Figure 4(a)) component and two dumb-bell shaped (Figures 4(c) and 4(d)) components, while the absorptive target has only one component (Figure 4(e)).

Figures 4(b) and 4(f) show fits to the spatial intensity profile of the centrosymmetric component of the scattering target and that of the absorptive target, respectively, to retrieve the locations of the two targets. The locations and optical strengths of the targets retrieved by PCA are also shown in Table 1.

**3.3. NMF Analysis.** The mixing matrix and virtual sources were retrieved from the data matrix  $X$  using NMF as explained in Section 2.3.3. As in the other two approaches, only one component is extracted for the absorptive target. Since NMF has a non-negativity constraint, only the centrosymmetric component for the scattering target is obtained. Nonnegative component intensity distributions (NCIDs) on detector planes are shown in Figure 5. Similar images for NCIDs on source plane were also obtained using the virtual sources in  $S$ . The results are also shown in Table 1.

**3.4. Results and Discussion.** The positions and optical strengths of the targets retrieved by ICA, PCA, and NMF

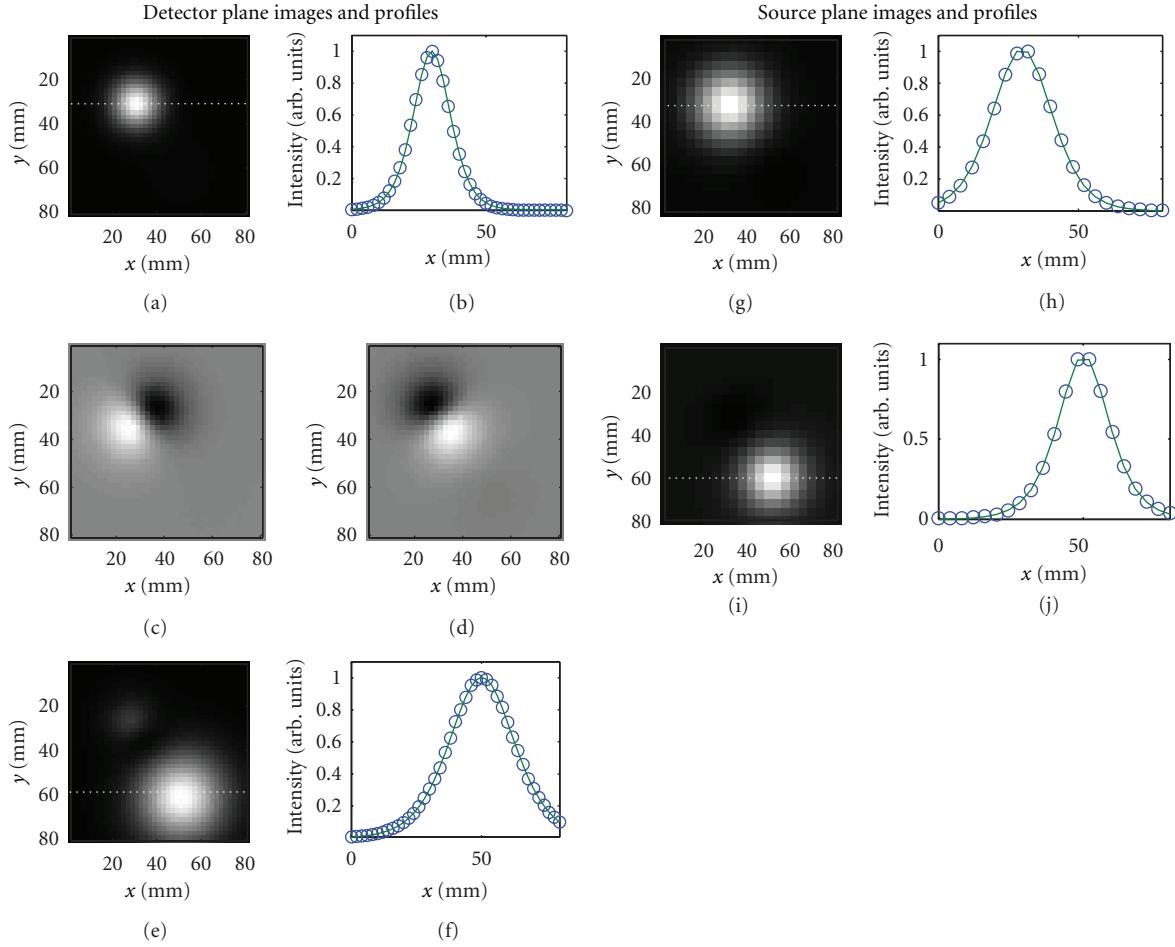


FIGURE 2: ICA-extracted two-dimensional intensity distribution on the detector plane of: (a) the centrosymmetric component; (c) and (d) dumb-bell shaped components of the scattering target; (e) the absorptive target. Similar intensity distribution on the source plane of: (g) the centrosymmetric component of the scattering target and (i) the absorptive target for comparison. Fits to the spatial intensity profile on the detector plane along the white dashed line (shown in figures) of the centrosymmetric component of the scattering target is shown in (b), and that of the absorptive target is shown in (f). Corresponding fits to spatial profiles on the source plane are displayed in (h) and (j), respectively.

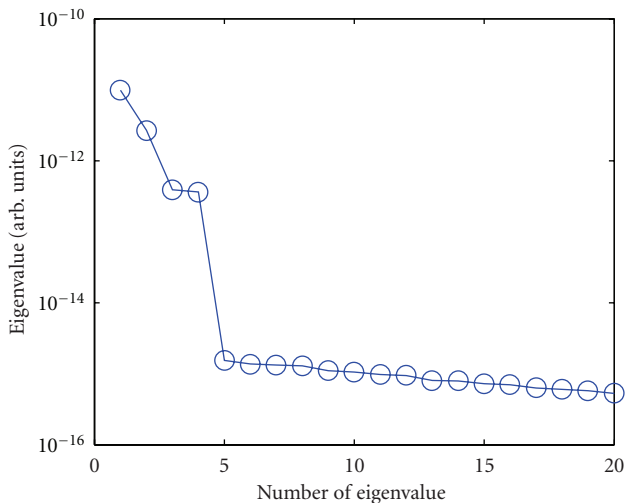


FIGURE 3: A logarithmic plot of the first 20 PCA eigenvalues.

algorithms are shown in Table 1, and compared to the known values. The retrieved results using all three algorithms from this simulated data are in excellent agreement with the known values.

### 4. Experiments

4.1. *Experimental Materials and Methods.* In this Section, the algorithms are evaluated using experimental data for absorptive and scattering targets embedded in model scattering media whose absorption and scattering properties are adjusted to mimic the average values of those parameters for human breast tissues. Two different experiments were carried out with two different samples. The first sample used a 250 mm × 250 mm × 50 mm transparent plastic container filled with Intralipid 10% suspension in water as the background medium. The concentration of Intralipid

TABLE 1: Positions and optical strengths retrieved using simulated data and ICA, PCA, and NMF algorithms.

Target	Known position (mm)	Algorithm	Fitted position (mm)	Error (mm)	Known strength*	Fitted strength*	Error (%)
Sca.	(30, 30, 25)	ICA	(29.9, 30.0, 25.1)	(0.1, 0, 0.1)	-180.3	-179.9	0.22
		PCA	(30.0, 30.0, 25.0)	(0, 0, 0)	-180.3	-180.1	0.11
		NMF	(30.0, 30.0, 25.0)	(0, 0, 0)	-180.3	-178.5	1
Abs.	(50, 60, 15)	ICA	(50.1, 60.2, 15.0)	(0.1, 0.2, 0)	1.803	1.826	1.28
		PCA	(50.1, 60.1, 14.9)	(0.1, 0.1, 0.1)	1.803	1.812	0.5
		NMF	(50.1, 60.1, 15.0)	(0.1, 0.1, 0)	1.803	1.803	0

\*The unit for absorption strength of the target is  $\text{mm}^3/\text{ns}$  and for scattering strength is  $\text{mm}^5/\text{ns}$ .

10% was adjusted to provide [27, 28] an absorption coefficient of  $\mu_a \sim 0.003 \text{ mm}^{-1}$ , and a transport mean-free path  $l_t \sim 1.43 \text{ mm}$  at 785 nm. The second sample used a similar container with dimension of  $250 \text{ mm} \times 250 \text{ mm} \times 60 \text{ mm}$  filled with Intralipid 20% suspension in water. The concentration of Intralipid 20% was adjusted to provide [27, 28]  $\mu_a \sim 0.003 \text{ mm}^{-1}$ , and  $l_t \sim 1 \text{ mm}$  at 785 nm. These optical parameters of the medium were selected to be similar to the average values of those parameters for human breast tissue. The thickness of the samples was also comparable to that of a typical compressed female human breast.

In the first experiment, two absorptive targets were embedded in the medium. The targets were  $\sim 10$ -mm diameter glass spheres filled Indocyanine green (ICG) dye dissolved in Intralipid-20% suspension in water to obtain an absorption coefficient  $\mu_a = 1.15 \text{ mm}^{-1}$  at 785 nm, and to match the background scattering coefficient of  $1.97 \text{ mm}^{-1}$ . The targets were placed at (57.2, 18.1, 20.0) mm and (19.9, 48.1, 25.0) mm, respectively.

In the second experiment, two scattering targets were embedded, which were also  $\sim 10 \text{ mm}$  diameter glass spheres, filled with Intralipid-20% suspension in water. The transport mean free path,  $l_t$  was adjusted to be 0.25 mm, with scattering coefficient  $\mu_s \approx 11 \text{ mm}^{-1}$ , and absorption coefficient  $\mu_a$  same as that of the background medium. The targets were placed in the middle plane ( $z = 30 \text{ mm}$ ) in the container with a lateral distance of 40 mm from each other (center to center).

The experimental setup is schematically shown in Figure 6. A 10 mW 785 nm diode laser beam was used to illuminate the first sample, while a 100 mW 785 nm diode laser beam was used for the second sample. The input surface (source plane) of the samples was scanned across the laser beam in an  $x$ - $y$  array of grid points to realize the multi-source interrogation of the samples. The transmitted light from the exit surface (detector plane) was recorded by a 1024 pixel  $\times$  1024 pixel (pixel size =  $24 \mu\text{m}$ ) CCD camera (Photometrics CH350) equipped with a 60 mm focal-length camera lens. Each pixel of the CCD camera can be considered to be a detector implementing the multidetector signal acquisition arrangement. A set of 16 bit 1024 pixel  $\times$  1024 pixel images were acquired. The two samples were scanned in an array of  $11 \times 12$  and  $11 \times 15$  grid points, respectively, with a step size of 5 mm in both cases. The processes of scanning and data acquisition were controlled by a personal computer. At all scan positions, raw transillumination images of the samples were recorded by the computer for further analysis.

**4.2. Analysis and Results.** A region of interest (ROI) was cropped out from each image. Then, every  $5 \times 5$  pixels in each cropped image were binned to one pixel to enhance signal-to-noise ratio. A background image was generated by calculating an average image for all scan positions to approximate the transillumination image without target(s) embedded.

This averaging method for generating background image is suitable for small targets used in our experiments, as the ratio of the volume of the sample to that of the target was quite high ( $\sim 500:1$ ). For *in vivo* imaging of tumors in early stages of growth, the breast-to-tumor volume ratio will be similarly high, and the averaging method will be applicable. Alternative approaches for generating a background image include using image of (a) a phantom that has the same average optical properties as the sample [29]; (b) the healthy contralateral breast for breast imaging [30]; (c) the sample obtained using light of wavelength for which the target(s) and the background have identical optical properties [31]. Still another approach is to compute the background using an appropriate forward model [32]. A more detailed discussion of this important issue appears in one of our earlier publications [33].

The background image was also cropped and binned corresponding to the ROI for each scan position. Perturbation in the light intensity distribution,  $\Delta\phi$  due to targets in each image was found by subtracting the background image from the image. The data matrix  $X$  was then constructed using the light intensity perturbations at all scan positions. ICA, PCA, and NMF decomposition algorithms were performed on the data matrix separately. Results are shown and discussed below.

**4.2.1. Absorptive Targets.** The images on the detector plane obtained using the ICA, PCA, and NMF algorithms are shown in Figures 7, 8, and 9, respectively. Similar images on the source plane were also obtained using all three algorithms. The right side of each figure shows the corresponding spatial intensity profile. Locations of the targets are extracted from fits to these spatial intensity profiles, as described in Section 2.3 using (6a) and (6b). The results are presented in Table 2. In Figure 7, images on the source plane are shown in (e) and (g), and Green's function fits to their spatial profiles are shown in (f) and (h) for comparison.

It follows from the comparison of the results in Table 2 that the positions retrieved by all three algorithms are in good agreement with the known positions. The errors

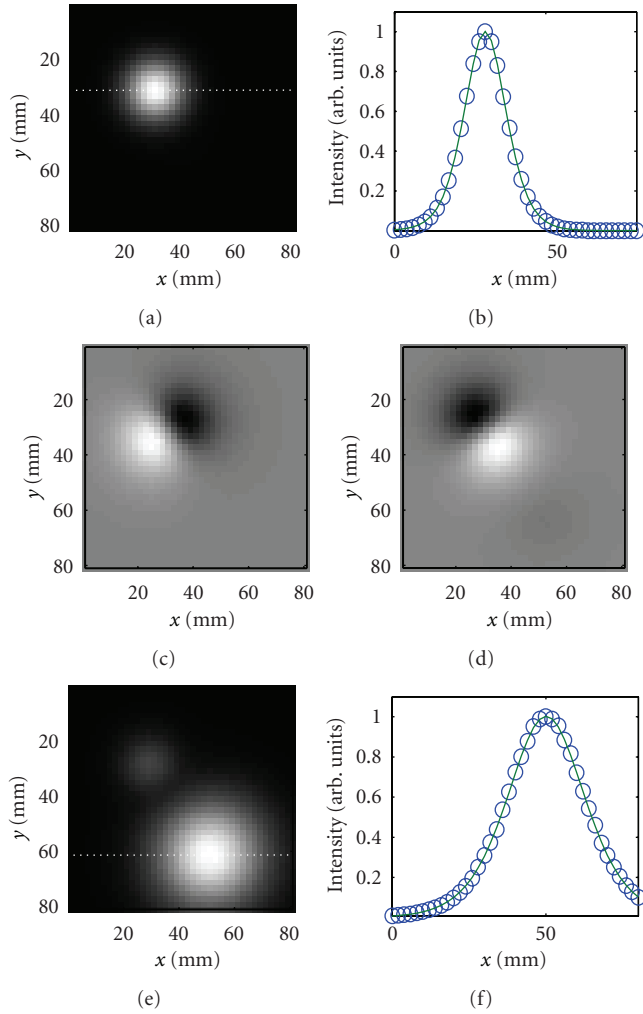


FIGURE 4: PCA-extracted two-dimensional intensity distribution on the detector plane of: (a) the centrosymmetric component; and (c) and (d) dumb-bell shaped components of the scattering target; (e) the absorptive target. Green's function fits to the spatial intensity profiles along the dashed line (shown in figures) of the (b) centrosymmetric component of the scattering target and (f) absorptive target, respectively, to retrieve the locations of the two targets.

in the retrieved locations  $(x, y, z)$  of the two targets were within 1.7 mm. The PCIDs were not totally separated. Some “residue” was observed in one PCID from the other. ICA and NMF separated two components from this dataset more clearly.

4.2.2. *Scattering Targets.* The “images” corresponding to the centrosymmetric components of the virtual sources (targets) on the detector plane obtained using the ICA, PCA, and NMF algorithms are shown in Figures 10, 11, and 12, respectively. Similar images on the source plane were also obtained. The right side of each figure shows the corresponding spatial intensity profile. Locations of the targets are extracted from fits to these spatial intensity

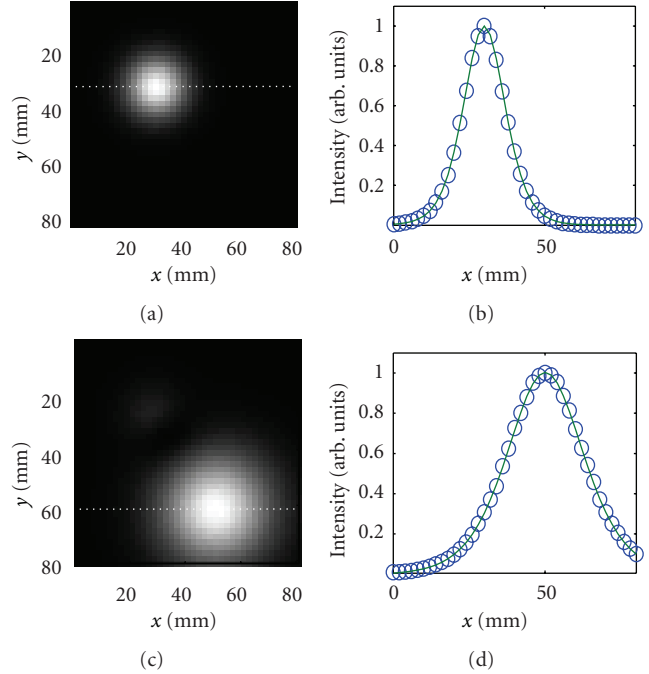


FIGURE 5: NMF-extracted two-dimensional intensity distribution on the detector plane of: (a) the centrosymmetric component of the scattering target; (c) the absorptive target. Fits to the corresponding spatial intensity profiles along the dashed line (shown in figures) are shown in (b) and (d), respectively.

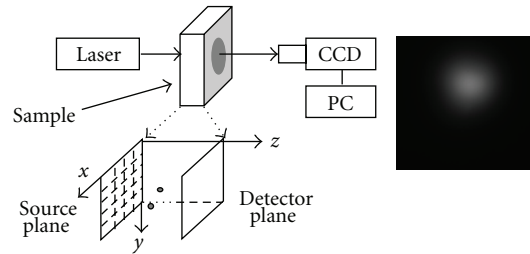


FIGURE 6: A schematic diagram of the experimental arrangement used for imaging objects embedded in a turbid medium. The inset at the bottom shows the 2D array in the input plane that was scanned across the incident laser beam; the inset to the right shows a typical raw image recorded by the CCD. (CCD: charge coupled device, and PC: personal computer).

profiles, as described in Section 2.3 using (6a) and (6b). The results are presented in Table 3.

Both targets were detected by all three algorithms. The target locations retrieved by three algorithms are shown in Table 3 and compared with known locations. Overall, all three algorithms detect and locate the scattering targets and the absorptive targets with good accuracy, the maximum deviation of any one coordinate from the known value being  $\sim 3$  mm. Since the maximum difference between the known and retrieved position coordinates was larger for the scattering targets, we calculated the squared correlation coefficient  $\gamma$  to assess the fitting quality. NMF retrieves

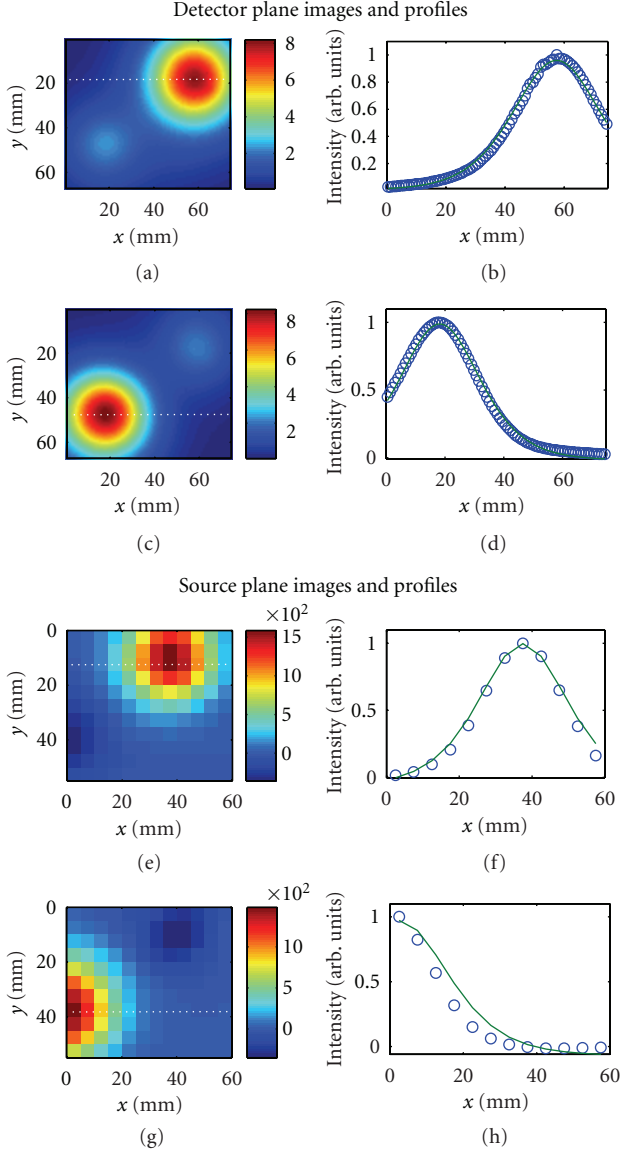


FIGURE 7: ICA-generated ICIDs on the detector plane are shown in (a) and (c); corresponding Green's function fits to the horizontal spatial profiles through the dashed lines are shown in (b) and (d). ICIDs on the source plane are shown in (e) and (g); corresponding Green's function fits to the horizontal spatial profiles through the dashed line are shown in (f) and (h).

the position coordinates better (within 0.5 mm) for the scattering Target 2 than done by ICA and PCA (deviation from known values being between 2-3 mm). NMF retrieved the position coordinates for Target 1 with 3.0 mm error in  $z$  direction, which is not as good as that done by ICA and PCA. But  $\gamma$  is 0.783 and 0.778 in the fittings for ICA and PCA, respectively, as compared to 0.993 for NMF, indicating that the quality of the fitting is better for NMF. The quality of fitting is presumably affected by the efficacy of decomposition. The decomposed NCIDs by NMF were more "clean" than those decomposed by ICA and PCA. We ascribe the observed higher errors in ICA and PCA estimates of the

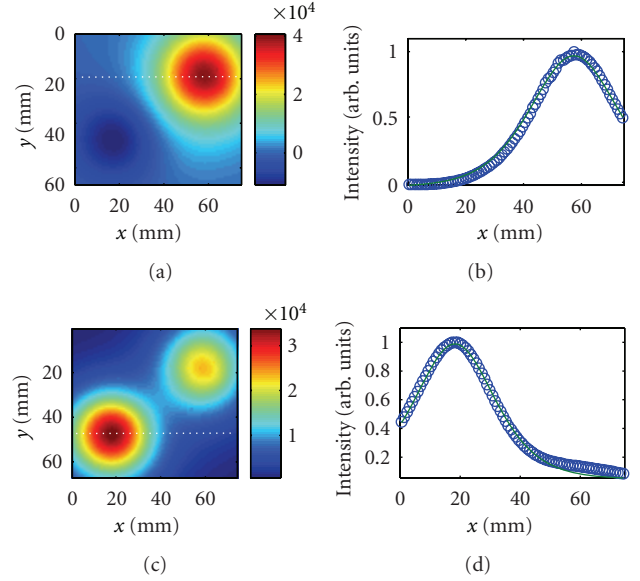


FIGURE 8: PCIDs on the detector plane are shown in (a) and (c); and corresponding Green's function fits to the horizontal spatial profiles through the dashed line are shown in (b) and (d).

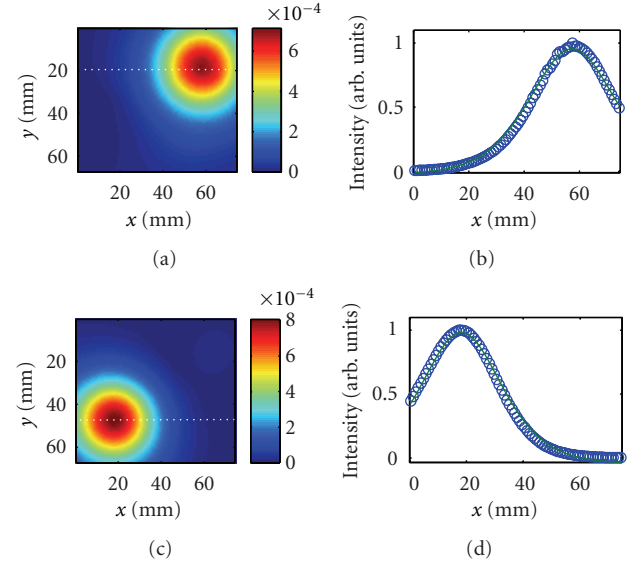


FIGURE 9: NCIDs on the detector plane are shown in (a) and (c); corresponding Green's function fits to the horizontal spatial profiles through the dashed line are shown in (b) and (d).

position coordinates of the scattering Target 2 than the NMF estimates to the interference from the other virtual source (corresponding to Target 1) in ICA (Figure 10(c)) and PCA (Figure 11(c)) images. It is commonly believed that errors in locating a scattering target are higher than that for locating an absorptive target, and the results of this study conform to that notion.

TABLE 2: Known positions versus retrieved positions of the absorptive targets using ICA, PCA, and NMF algorithms.

Target	Known position (mm)	Algorithm	Fitted position (mm)	Error (mm)
1	(57.2, 18.1, 20)	ICA	(57.4, 18.2, 21.5)	(0.2, 0.1, 1.5)
		PCA	(57.4, 18.2, 20.6)	(0.2, 0.1, 0.6)
		NMF	(57.4, 18.2, 19.5)	(0.2, 0.1, 0.5)
2	(19.9, 48.1, 25)	ICA	(18.2, 46.7, 24.7)	(1.7, 1.4, 0.3)
		PCA	(18.2, 47.6, 25.9)	(1.7, 0.5, 0.9)
		NMF	(18.2, 47.6, 23.3)	(1.7, 0.5, 1.7)

TABLE 3: Known positions versus retrieved positions of the scattering targets using ICA, PCA, and NMF algorithms.

Target	Known position (mm)	Algorithm	Fitted position (mm)	Error (mm)
1	(13.0, 28.0, 30.0)	ICA	(12.6, 28.7, 29.1)	(0.4, 0.7, 0.9)
		PCA	(12.6, 28.7, 28.6)	(0.4, 0.7, 1.4)
		NMF	(12.0, 28.5, 33.0)	(1.0, 0.5, 3.0)
2	(53.3, 28.5, 30.0)	ICA	(51.0, 31.8, 26.8)	(2.3, 3.3, 3.2)
		PCA	(50.9, 31.8, 26.7)	(2.4, 3.3, 3.3)
		NMF	(53.3, 28.0, 30.3)	(0.0, 0.5, 0.3)

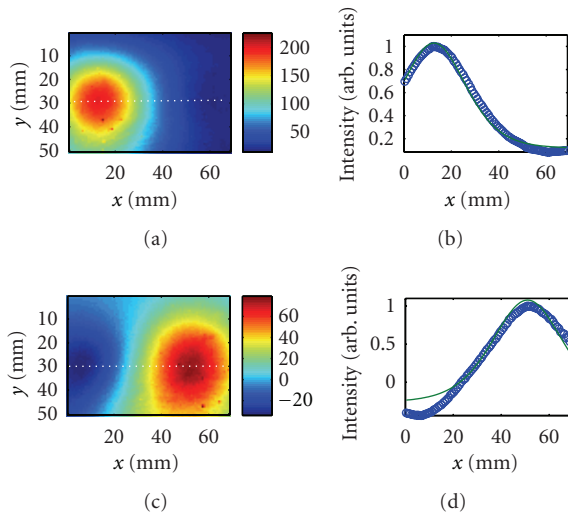


FIGURE 10: ICA-generated ICIDs on the detector plane are shown in (a) and (c); corresponding Green's function fits to the horizontal spatial profiles through the dashed line are shown in (b) and (d).

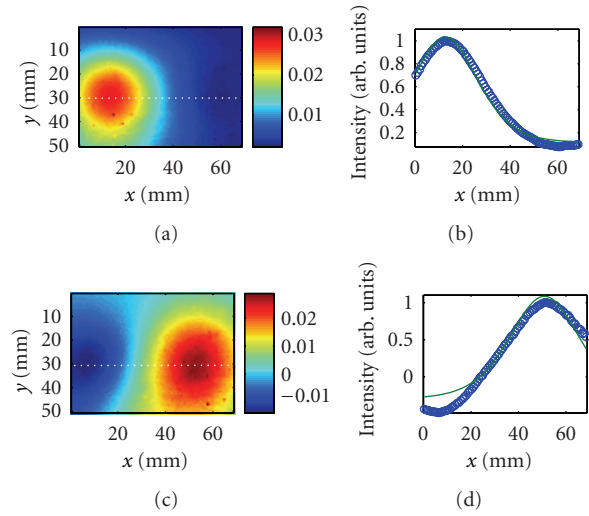


FIGURE 11: PCIDs on the detector plane are shown in (a) and (c); corresponding Green's function fits to the horizontal spatial profiles through the dashed line are shown in (b) and (d).

## 5. Summary and Discussion

Diffusive optical imaging was modeled as a BSS problem. ICA, PCA, and NMF were used to decompose the data matrix and locate the targets embedded in a highly scattering turbid medium. Only the components corresponding to the targets were extracted from a large dataset for target detection and localization.

It may be instructive to compare the objectives, scope, and computational complexity of these decomposition methods with model-based reconstruction methods. Decomposition methods obtain the 3D locations of targets (the number of targets is generally small). Based on the retrieved locations, the methods may then be further

extended to retrieve size and optical property information of the targets [9]. The common practice of model-based inverse reconstruction methods is to discretize the sample volume into  $N \times N \times N$  voxels and estimate absorption and/or scattering coefficient in each voxel iteratively. Voxels with significantly different optical properties than the surrounding are regions of interest and may be identified as targets. While estimating the optical properties, the forward model is solved repeatedly to calculate the intensity of the multiply scattered light on the sample boundary. The difference between the intensity of the multiply scattered light predicted by the forward model and the experimental measurements is minimized by seeking an optimal set of the optical properties of every voxel in the sample volume. The number of variables

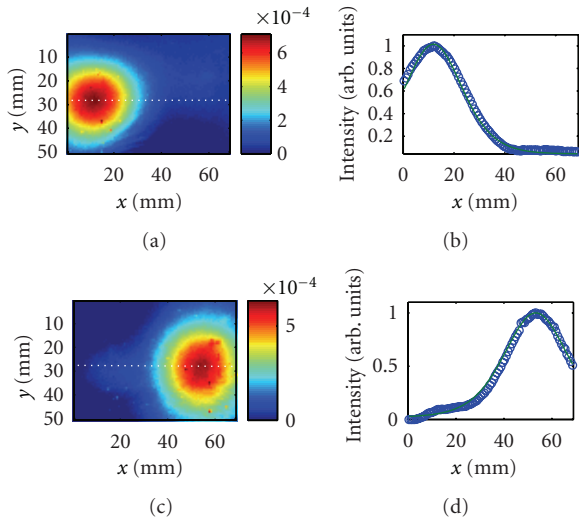


FIGURE 12: NCIDs on the detector plane are shown in (a) and (c); corresponding Green's function fits to the horizontal spatial profiles through the dashed line are shown in (b) and (d).

is thus, on the order of  $N^3$ . To determine location(s) of target(s) in three dimensions, the decomposition methods process the data matrix to retrieve the main components ( $A$  and  $S$ ). Here,  $A$  and  $S$  are two-dimensional matrices with the number of unknowns on the order of  $N^2$ . The number of unknowns is, hence, reduced  $N$  times in the decomposition methods compared to the model-based approaches, which leads to a substantial saving in the computational time when  $N$  is large. No repeated solution of the forward model is involved in decomposition methods. Consequently, decomposition methods are considerably faster.

A comparison of the computational complexity of these two types of approaches may shed further light on their relative computation economy. For a model-based iterative reconstruction method, an equation of the form  $b = Wx$  is solved to find the targets, where  $W$  is a weight matrix of size  $N_d N_s \times N_v$ ,  $N_d$ ,  $N_s$ , and  $N_v$  are the numbers of detectors, sources and voxels, respectively,  $b$  is an  $N_d N_s \times 1$  vector describing the perturbation in the detected light intensity due to the presence of targets, and  $x$  is the perturbation in the optical properties from the background values with dimension of  $N_v \times 1$ . The computational complexity is typically  $O(N_d N_s N_v^2)$  for a single iteration. For the decomposition approach,  $b$  is written as a 2D matrix  $X$  with dimension  $N_d \times N_s$ . To decompose matrix  $X$ , the computational complexity per iteration is typically of order  $O(N_d N_k)$  for ICA [34], and  $O(N_d N_s N_k)$  for NMF [16], where  $N_k$  is the number of components that relates to the number of targets and is usually a small number. For PCA using SVD, the complexity is  $O(N_s^2 N_k)$  [34]. The computational complexity of the intrinsic iterative process involved in the matrix decomposition algorithms is much lower than that in the model-based inverse reconstruction methods.

All three matrix decomposition methods presented in this manuscript can potentially be used in *in-vivo* real-time breast cancer imaging. The three algorithms have

different assumptions, which may lead to different favored conditions. In this study, the algorithms were evaluated using simulative and experimental data using model scattering media and absorptive and scattering targets. The  $(x, y, z)$  positions of the targets were retrieved with good accuracy. The decomposition provided by ICA is “cleaner” than that of the PCA. PCA did not clearly separate the two absorptive targets used in the first experiment. NMF decomposition seems to provide residue-free “cleaner” images than the other two methods in this study. However, since NMF is based on nonnegativity assumption, the results might deteriorate when such a non-negativity assumption does not hold well. While continuous wave measurements were used in the work presented in this paper, the approaches could be used with frequency domain and time domain measurements as well.

The work presented here focuses on detecting and locating small targets, which derive impetus from the need to detect tumors in early stages of growth when those are more amenable to treatment. All three methods are applicable for extended targets as well and are expected to provide the “center of optical strength” as the location of the target.

All three approaches are applicable for both scattering and absorbing targets and may be used in clinical setting. The contrast between a tumor and surrounding normal tissue can be due to differences in absorption, scattering, or both absorption and scattering properties and may depend significantly on the wavelength of light used. However, *a priori* knowledge of the optical characteristics (absorptive or scattering) is not crucial. As has been shown in (2) and (3), the expression for elements of the data matrix for absorptive targets involves Green's Functions  $G$ , while that for scattering targets involves  $\partial G / \partial z \approx -\kappa G$ , where  $\kappa = \sqrt{\mu_a / D}$  in CW [9]. This relationship with  $G$  provides basis for detection and localization of target(s), whether contrast is due to absorption, scattering, or both. We are using transillumination geometry, which is one of the approaches used by other researchers, and adequate signal for *in vivo* breast imaging is obtained [29, 35–38].

In this paper, we presented results when the approaches were used to detect and obtain three-dimensional location information of the targets. We have demonstrated, while developing OPTICA that a backprojection formalism can be further implemented to get a cross-section image of the target [11], or the retrieved target locations can be fed into other DOI methods as *a priori* information to get three-dimensional tomographic images. Since the approaches are suited for small targets, this hold promise for detecting and locating breast tumors in early stages of growth, which is crucially important for effective treatment. Further work involving *ex vivo* (model) and *in vivo* imaging of cancerous breast will be needed to establish the full potential of these approaches.

## Acknowledgment

The paper is supported in part by US Army Medical Research and Materiel Command under Contract no. W81XWH-07-1-0454.

## References

- [1] X. R. Cao and R. W. Liu, "General approach to blind source separation," *IEEE Transactions on Signal Processing*, vol. 44, no. 3, pp. 562–571, 1996.
- [2] J. F. Cardoso, "Blind signal separation: statistical principles," *Proceedings of the IEEE*, vol. 86, no. 10, pp. 2009–2025, 1998.
- [3] A. Hyvärinen, J. Karhunen, and E. Oja, *Independent Component Analysis*, Wiley, New York, NY, USA, 2001.
- [4] I. T. Jolliffe, *Principal Component Analysis*, Springer, New York, NY, USA, 1986.
- [5] D. D. Lee and H. S. Seung, "Learning the parts of objects by non-negative matrix factorization," *Nature*, vol. 401, no. 6755, pp. 788–791, 1999.
- [6] M. W. Berry, M. Browne, A. N. Langville, V. P. Pauca, and R. J. Plemmons, "Algorithms and applications for approximate nonnegative matrix factorization," *Computational Statistics and Data Analysis*, vol. 52, no. 1, pp. 155–173, 2007.
- [7] M. Xu, M. Alrubaiee, S. K. Gayen, and R. R. Alfano, "Optical imaging of turbid media using independent component analysis: theory and simulation," *Journal of Biomedical Optics*, vol. 10, no. 5, Article ID 051705, 2005.
- [8] M. Xu, M. Alrubaiee, S. K. Gayen, and R. R. Alfano, "Three-dimensional localization and optical imaging of objects in turbid media with independent component analysis," *Applied Optics*, vol. 44, no. 10, pp. 1889–1897, 2005.
- [9] M. Xu, M. Alrubaiee, S. K. Gayen, and R. R. Alfano, "Optical diffuse imaging of an ex vivo model cancerous human breast using independent component analysis," *IEEE Journal on Selected Topics in Quantum Electronics*, vol. 14, no. 1, pp. 43–49, 2008.
- [10] M. Alrubaiee, M. Xu, S. K. Gayen, M. Brito, and R. R. Alfano, "Three-dimensional optical tomographic imaging of scattering objects in tissue-simulating turbid media using independent component analysis," *Applied Physics Letters*, vol. 87, no. 19, Article ID 191112, pp. 1–3, 2005.
- [11] M. Alrubaiee, M. Xu, S. K. Gayen, and R. R. Alfano, "Localization and cross section reconstruction of fluorescent targets in ex vivo breast tissue using independent component analysis," *Applied Physics Letters*, vol. 89, no. 13, Article ID 133902, 2006.
- [12] D. L. Massart, B. G. M. Vandeginste, S. M. Deming, Y. Michotte, and L. Kaufman, *Chemometrics: A Textbook*, Elsevier, Amsterdam, The Netherlands, 1988.
- [13] M. Turk and A. Pentland, "Eigenfaces for recognition," *Journal of Cognitive Neuroscience*, vol. 3, no. 1, pp. 71–86, 1991.
- [14] L. K. Hansen, J. Larsen, F. A. Nielsen et al., "Generalizable patterns in neuroimaging: how many principal components?" *NeuroImage*, vol. 9, no. 5, pp. 534–544, 1999.
- [15] J. P. Brunet, P. Tamayo, T. R. Golub, and J. P. Mesirov, "Metagenes and molecular pattern discovery using matrix factorization," *Proceedings of the National Academy of Sciences of the United States of America*, vol. 101, no. 12, pp. 4164–4169, 2004.
- [16] V. P. Pauca, J. Piper, and R. J. Plemmons, "Nonnegative matrix factorization for spectral data analysis," *Linear Algebra and Its Applications*, vol. 416, no. 1, pp. 29–47, 2006.
- [17] A. Ishimaru, "Diffusion of a pulse in densely distributed scatterers," *Journal of the Optical Society of America*, vol. 68, no. 8, pp. 1045–1050, 1978.
- [18] K. Furutsu, "Diffusion equation derived from the space-time transport equation," *Journal of the Optical Society of America*, vol. 70, no. 4, pp. 360–366, 1980.
- [19] M. S. Patterson, B. Chance, and B. C. Wilson, "Time resolved reflectance and transmittance for the non-invasive measurement of tissue optical properties," *Applied Optics*, vol. 28, no. 12, pp. 2331–2336, 1989.
- [20] S. Chandrasekhar, *Radiative Transfer*, Clarendon Press, Oxford, UK, 1950.
- [21] A. Ishimaru, *Wave Propagation and Scattering in Random Media*, vol. 1 of *Single Scattering and Transport Theory*, Academic, New York, NY, USA, 1978.
- [22] S. R. Arridge and J. C. Schotland, "Optical tomography: forward and inverse problems," *Inverse Problems*, vol. 25, Article ID 123010, 2009.
- [23] S. R. Arridge, "Photon-measurement density functions. Part I: analytical forms," *Applied Optics*, vol. 34, no. 31, pp. 7395–7409, 1995.
- [24] P. C. Hansen, "Analysis of discrete ill-posed problems by means of the L-curve," *SIAM Review*, vol. 34, pp. 561–580, 1992.
- [25] P. Paatero and U. Tapper, "Positive matrix factorization: a non-negative factor model with optimal utilization of error estimates of data values," *Environmetrics*, vol. 5, no. 2, pp. 111–126, 1994.
- [26] P. Paatero, "The multilinear engine: a table-driven, least squares program for solving multilinear problems, including the n-way parallel factor analysis model," *Journal of Computational and Graphical Statistics*, vol. 8, no. 4, pp. 854–888, 1999.
- [27] H. J. van Staveren, C. J. M. Moes, J. van Marle, S. A. Prahl, and M. J. C. van Gemert, "Light scattering in Intralipid-10% in the wavelength range of 400–1100 nm," *Applied Optics*, vol. 31, pp. 4507–4514, 1991.
- [28] C. Bordier, C. Andraud, E. Charron, J. Lafait, M. Anastasiadou, and A. De Martino, "Illustration of a bimodal system in Intralipid-20% by polarized light scattering: experiments and modeling," *Applied Physics A*, vol. 94, no. 2, pp. 347–355, 2009.
- [29] T. Nielsen, B. Brendel, R. Ziegler et al., "Linear image reconstruction for a diffuse optical mammography system in a noncompressed geometry using scattering fluid," *Applied Optics*, vol. 48, no. 10, pp. D1–D13, 2009.
- [30] Y. Ardeshirpour, M. Huang, and Q. Zhu, "Effect of the chest wall on breast lesion reconstruction," *Journal of Biomedical Optics*, vol. 14, no. 4, p. 044005, 2009.
- [31] B. W. Pogue, M. S. Patterson, H. Jiang, and K. D. Paulsen, "Initial assessment of a simple system for frequency domain diffuse optical tomography," *Physics in Medicine and Biology*, vol. 40, no. 10, pp. 1709–1729, 1995.
- [32] A. Poellinger, J. C. Martin, S. L. Ponder et al., "Near-infrared laser computed tomography of the breast. First clinical experience," *Academic Radiology*, vol. 15, no. 12, pp. 1545–1553, 2008.
- [33] B. Wu, W. Cai, M. Alrubaiee, M. Xu, and S. K. Gayen, "Time reversal optical tomography: locating targets in a highly scattering turbid medium," *Optics Express*, vol. 19, no. 22, pp. 21956–21976, 2011.
- [34] T. Ristaniemi and J. Joutsensalo, "Advanced ICA-based receivers for block fading DS-SSMA channels," *Signal Processing*, vol. 82, no. 3, pp. 417–431, 2002.
- [35] M. Cutler, "Transillumination as an aid in the diagnosis of breast lesions," *Surgery, Gynecology and Obstetrics*, vol. 48, pp. 721–729, 1929.
- [36] R. Choe, A. Corlu, K. Lee et al., "Diffuse optical tomography of breast cancer during neoadjuvant chemotherapy: a case study with comparison to MRI," *Medical Physics*, vol. 32, no. 4, pp. 1128–1139, 2005.
- [37] A. Pifferi, P. Taroni, A. Torricelli, F. Messina, R. Cubeddu, and G. Danesini, "Four-wavelength time-resolved optical

- mammography in the 680-980-nm range,” *Optics Letters*, vol. 28, no. 13, pp. 1138–1140, 2003.
- [38] B. J. Tromberg, B. W. Pogue, K. D. Paulsen, A. G. Yodh, D. A. Boas, and A. E. Cerussi, “Assessing the future of diffuse optical imaging technologies for breast cancer management,” *Medical Physics*, vol. 35, no. 6, pp. 2443–2451, 2008.

## Research Article

# Volumetric Diffuse Optical Tomography for Small Animals Using a CCD-Camera-Based Imaging System

Zi-Jing Lin,<sup>1</sup> Haijing Niu,<sup>2</sup> Lin Li,<sup>1</sup> and Hanli Liu<sup>1</sup>

<sup>1</sup>Department of Bioengineering, Joint Graduate Program between University of Texas at Arlington and University of Texas Southwestern Medical Center, University of Texas at Arlington, Arlington, TX 76019, USA

<sup>2</sup>State key Laboratory of Cognitive Neuroscience and Learning, Beijing Normal University, Beijing 10875, China

Correspondence should be addressed to Hanli Liu, hanli@uta.edu

Received 15 July 2011; Revised 21 October 2011; Accepted 24 October 2011

Academic Editor: Javier A. Jo

Copyright © 2012 Zi-Jing Lin et al. This is an open access article distributed under the Creative Commons Attribution License, which permits unrestricted use, distribution, and reproduction in any medium, provided the original work is properly cited.

We report the feasibility of three-dimensional (3D) volumetric diffuse optical tomography for small animal imaging by using a CCD-camera-based imaging system with a newly developed depth compensation algorithm (DCA). Our computer simulations and laboratory phantom studies have demonstrated that the combination of a CCD camera and DCA can significantly improve the accuracy in depth localization and lead to reconstruction of 3D volumetric images. This approach may present great interests for noninvasive 3D localization of an anomaly hidden in tissue, such as a tumor or a stroke lesion, for preclinical small animal models.

## 1. Introduction

Over the last decade, diffuse optical tomography (DOT) has become an emerging medical imaging modality [1, 2], which permits near infrared (NIR) light (650–900 nm) to penetrate deep tissues in several centimeters noninvasively. This technique has been investigated for several clinical applications, particularly for monitoring of functional brain activities [3–5] and detection of breast cancer [6, 7]. The fundamental principle of DOT is that the detected NIR signals reflect optical properties of the underlying biological tissues [8, 9] and that the spatial distribution of such measured optical properties can be used to reconstruct optical tomographic images.

In the meantime, small animal models have been often utilized in preclinical research in order to investigate a variety of human diseases. Commonly used modalities to image small animals include magnetic resonance imaging (MRI) [10], computed tomography (CT) [11], positron emission tomography (PET) [12], and single photon emission computed tomography (SPECT) [13]. As compared to MRI and CT, DOT is able to provide functional sensitivity; as compared to CT, PET, and SPECT, DOT is radiation-free. More recently, DOT has become an imaging methodology

in preclinical studies for certain diseases, such as stroke [14] and cancer [15].

To date, fiber-based and charge-coupled device- (CCD-) camera-based DOT techniques are well developed and widely performed in both human and animal studies. A fiber-based DOT system has several advantages, namely, being compatible with different geometry and shape of a measured organ and having low noise because of direct contact of fibers on the tissue surface. However, a limited surface space on small animals is often a constraint to place many fiber optodes and thus restricts the spatial resolution of reconstructed images. A CCD-camera-based DOT system eliminates such a problem since the CCD camera can serve as a detector array with possible thousands of virtual detectors and cover a wide field of view (FOV). Moreover, such a DOT system is simpler and more portable with lower cost, as compared to a fiber-based DOT system.

While DOT is a promising tool to image diseases noninvasively, one major limitation exists due to scattering nature of photons traveling in tissue. Namely, strong light scattering of biological tissue causes the detection sensitivity of DOT to attenuate exponentially with increased depth, resulting in poor depth localization in DOT. A variety of efforts have been made by different research groups to improve the accuracy

in depth localization. A layer-based sigmoid adjustment (LSA) method was introduced to balance the sensitivity contrast in depth by directly adjusting the forward sensitivity matrix [16]. Spatially variant regularization (SVR) [17] was also introduced to compensate the decrease in measurement sensitivity with increase of depth by modifying the penalty term of regularization along depth. SVR has been utilized in the frequency-domain and CW-based DOT techniques for imaging human breast cancer and brain functions. Recently, we have developed a depth compensation algorithm (DCA) to significantly improve the accuracy of DOT in depth localization, as demonstrated by both laboratory phantom and human brain measurements [18, 19], using fiber-based DOT systems.

In this study, we wish to demonstrate the feasibility and improvement of three-dimensional (3D) volumetric DOT for small animal imaging by using CCD-camera-based DOT in combination with DCA. Our results are based on computer simulations and laboratory phantom experiments, confirming that the combination of a CCD camera and DCA is an effective approach for 3D volumetric images to be utilized in preclinical research.

## 2. Materials and Methodology

### 2.1. Implementation of a CCD-Camera-Based DOT System.

We implemented a CCD-camera-based, NIR spectroscopic imaging system, which consisted of a broadband light source, a multiplexer, a 6-filter wheel, and a high-speed CCD camera (Figure 1(a)) with a pixel matrix of  $496 \times 656$ . Such a system allowed us to acquire the transmitted/reflected NIR signals from living tissues at specific wavelengths so as to obtain hemodynamic signals within a time scale of a hundred milliseconds. We performed CCD-camera calibration by utilizing laboratory tissue phantoms (Figure 1(b)) in order to (a) calibrate the CCD camera for its nonuniformity and to (b) examine the stability and linearity of the calibrated camera.

### 2.2. Correction of the CCD-Camera-Based DOT System.

Numbers of factors affect the results of a CCD image. These factors include (1) small electric signals seen by the camera without any optical input, or dark current, (2) pixel-to-pixel sensitivity variations, and (3) nonuniform illumination of the CCD chip due to vignetting and dust. Flat field correction is a common technique [20] that can be used to obtain improved quality of CCD images. The flat field technique removes the effects due to dark current, pixel-to-pixel sensitivity variations, uneven illumination, and nonuniformity caused by vignetting and dust.

During the process of correction, we collected two types of images besides taking raw object images: (1) dark images without any optical input and (2) reference images with planer illumination. The dark images were needed to correct the electric current that flows through each pixel of the CCD array without any optical input. The planer-illuminated reference images were obtained by uniformly illuminating a highly reflecting reference plate, which has a reflectivity of

98% and a dimension of  $200 \times 200 \text{ mm}^2$ . To approximately achieve a planer illumination, we used a white light lamp and placed it 1.5 meters away from the measurement site, with a good amount of light intensity, without saturating the camera.

The procedures used to perform flat field correction in this study are listed below: first, take a dark image by blocking the camera's entrance completely, followed by taking object images with a point-source illumination from one side of the object (see Figure 1(b)). The integration times were kept the same for both situations. Second, take a reference image with a planer illumination followed by the corresponding dark image, also using the same integration time for both. Then, corrected object images can be obtained with the following equation:

$$I = K \frac{O - D_O}{R - D_R}, \quad (1)$$

where  $I$  represents the corrected image,  $R$  is the reference image from the reference plate,  $O$  is the raw object image,  $D_O$  and  $D_R$  represent dark images taken with the corresponding integration times for the object and reference plate, respectively, and  $K$  is a constant and usually is equal to the intensity averaged over the area of reference image. To demonstrate the necessity of correcting a raw image, Figure 2 shows the cross-section profiles along  $X$  axis and  $Y$  axis of a CCD image before and after flat field correction. It is noticed that the center of FOV detects much higher light intensity than the edges before correction. After the correction, it is clearly shown that the uniformity on the edges is much improved while the correction is not perfect.

For quantitative comparison, we calculated maximal relative deviations between the central intensity and the intensity at the edge of the images for both the raw and corrected images, using the following expression:

$$\text{relative deviation} = \frac{\text{central intensity}}{\text{intensity at the edge}}, \quad (2)$$

The estimated maximal values of relative deviations were 40% and 10% for the raw image and corrected image, respectively. In most of the image regions, such deviations in the corrected images were less than 10%.

### 2.3. Stability and Linearity of the CCD Camera System.

To check the stability of the CCD camera system, repeated measurements were taken at different times. We utilized a 1% Intralipid solution (Baxter Healthcare Corporation, Deerfield, IL) as a testing medium and took optical readings as the baseline images ( $I_B$ ) at time "0", followed by other images ( $I_M$ ) taken 1 minute, 5 minutes, 10 minutes, 30 minutes, 1 hour, and 1 day after the baseline measurement using the same experimental conditions (i.e., the same integration time). Each of the images was calibrated or corrected with the flat field correction and averaged over all the pixels per image to obtain an averaged light intensity for each respective image. Then, a ratio between the averaged intensity from each set of  $I_M$  and the averaged intensity from  $I_B$  (the baseline image) was obtained for all cases,

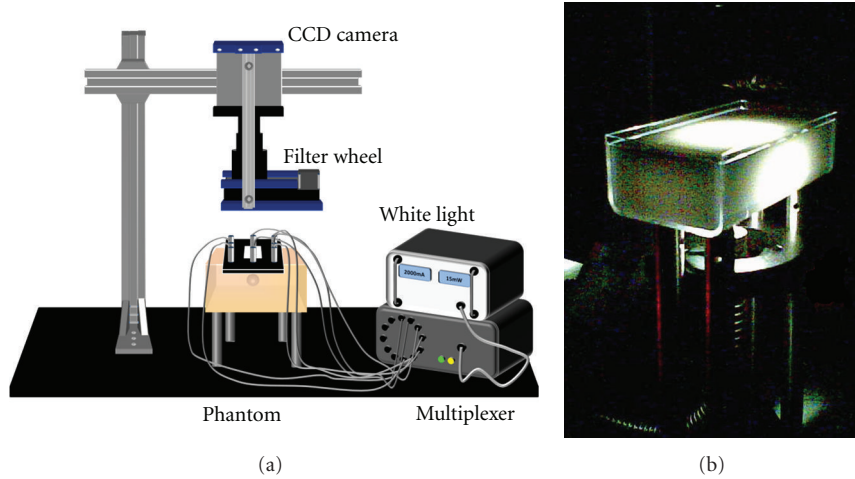


FIGURE 1: (a) Schematic diagram of a CCD-camera-based DOT system for laboratory measurement; (b) a tissue phantom which was sitting on the phantom supporter with the illumination light coming from the bottom.

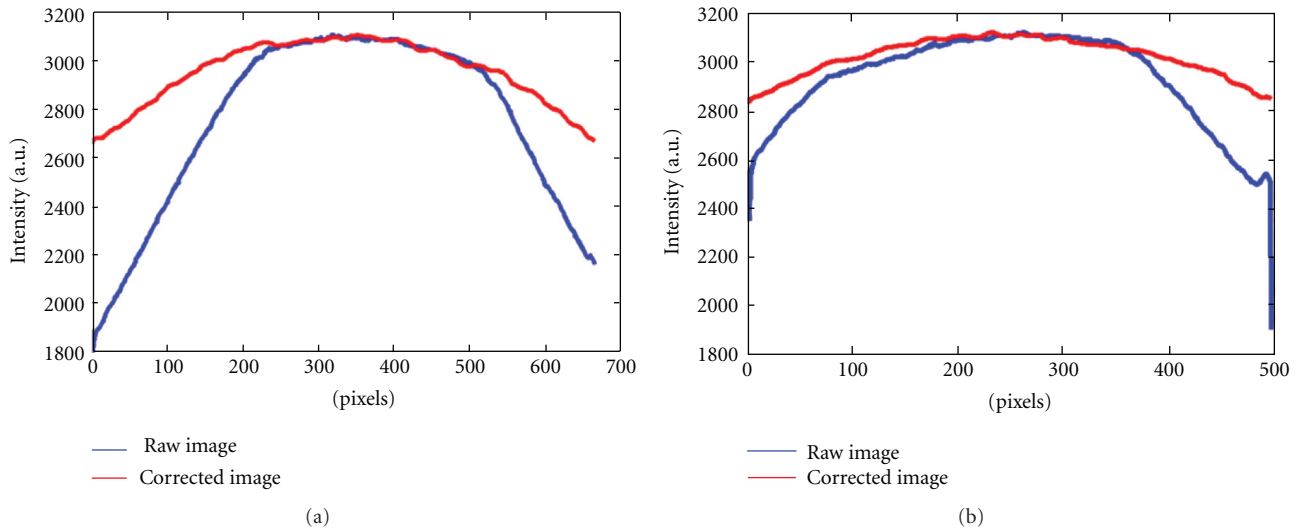


FIGURE 2: The cross-section profile of intensity from the raw and corrected image along (a) X axis and (b) Y axis.

as shown in Figure 3(a). It is very clear that the image intensities taken at different time intervals are fluctuated less than 1% of that of the baseline image, confirming good stability of the CCD camera system. Similar experiments were repeated using a 1.5% Intralipid solution to increase the light scattering property of the testing medium. The results are very consistent with the results from 1% Intralipid solution, demonstrating that a CCD camera has high stability with a fluctuation of intensity less than 1%.

In addition, we checked whether the intensity of light source could affect the results. We took numerous images using the same Intralipid concentration, but with different intensities of the light source. The averaged intensity of an image taken at light source level 5 was selected as the baseline,  $I_B$ ; the ratios between the averaged intensities from other images,  $I_M$ , with different light source levels to the chosen baseline,  $I_M/I_B$ , are shown in Figure 3(b). This set

of tests confirms that the level of the light source does not significantly affect the relative changes of our CCD camera output. Namely, the camera provides stable output images, independent of variable light levels.

Furthermore, to test the linearity of the CCD camera system, we performed two experiments: (1) one was to determine the image intensity changes versus absorption changes within the testing medium, and (2) the other one was to obtain the relationship between the image intensity measured versus changes in light scattering property within the testing medium. The tissue-mimic Intralipid solution was held in an acrylic box, which had a dimension of  $10 \text{ cm} \times 5 \text{ cm} \times 3 \text{ cm}$  (length  $\times$  width  $\times$  height). The acrylic box was wrapped by black tape except the top side of the box to prevent light from passing through the box wall.

For absorption changes, the experiments were performed using 1% Intralipid solutions with addition of  $10 \mu\text{L}$ ,  $20 \mu\text{L}$ ,

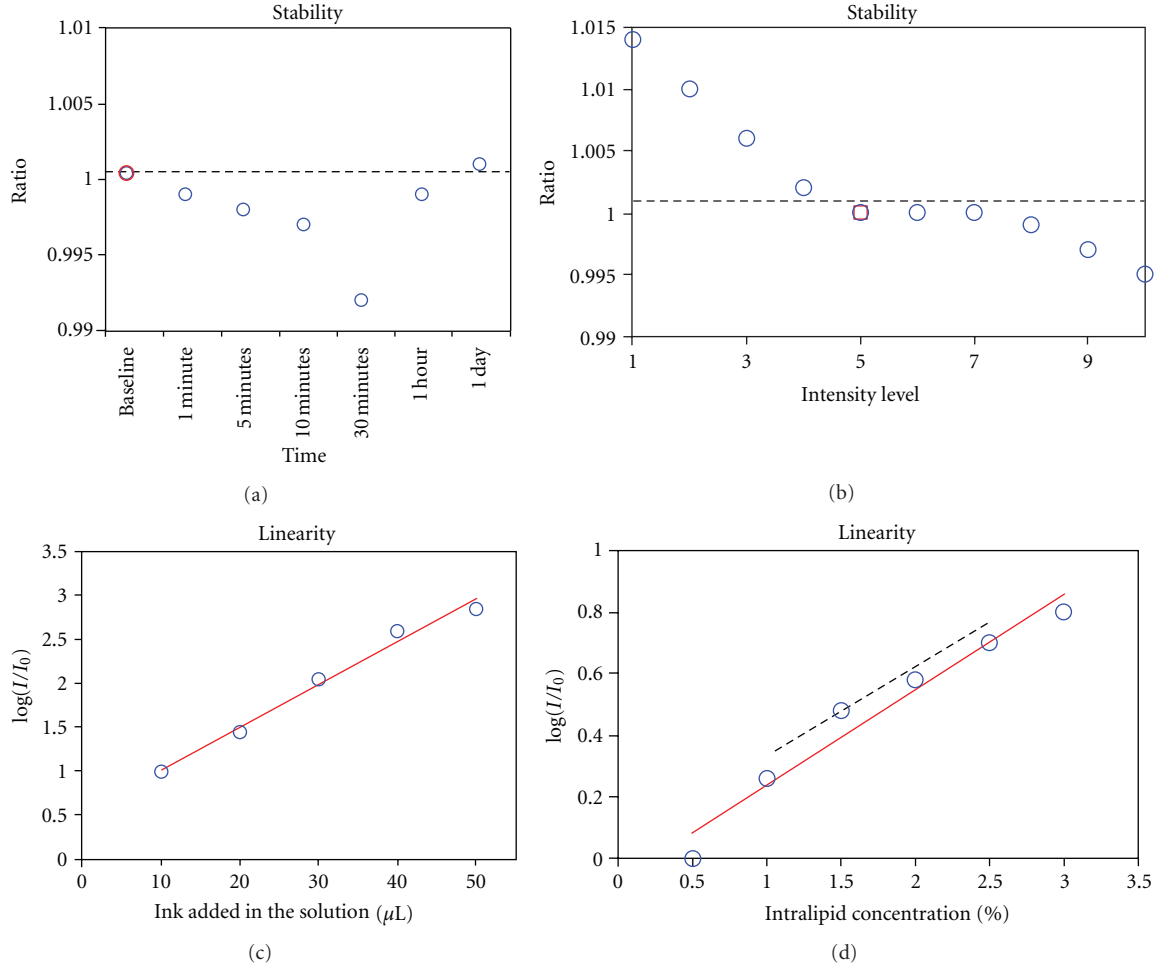


FIGURE 3: Ratio of the intensities ( $I_M/I_B$ ) for a 1% Intralipid solution (a) at different times of measurement and (b) with different light intensities. The relationships between  $\log(I_0/I)$  and (c) the volume of ink added into the testing solution for a 1% Intralipid solution, and (d) the concentration of Intralipid. Dashed line in (d) shows the linear relationship within Intralipid concentrations between 1% and 2.5%.

30  $\mu\text{L}$ , 40  $\mu\text{L}$ , and 50  $\mu\text{L}$  of diluted ink. The CCD camera readings were taken throughout these Intralipid solutions, using the same integration time. We further plotted values of  $\log(I_0/I)$  versus the volume of the ink added in the solution, where  $I_0$  and  $I$  represented the averaged image intensities taken from the Intralipid solutions without ink and with different concentrations of ink. As seen in Figure 3(c), the data can be fitted well by a linear line. A similar behavior was seen for the 1.5% Intralipid case, confirming that a CCD camera has high-quality performance in its linearity with respect to light absorption.

For light scattering changes, the experiments were taken from multiple Intralipid solutions with concentrations of 0.5%, 1%, 1.5%, 2%, 2.5%, and 3% (using the same integration time). A plot of  $\log(I_0/I)$  versus concentration of Intralipid is given in Figure 3(d), where  $I_0$  and  $I$  represent the averaged image intensities taken from the Intralipid solutions at 0.5% and other concentrations. A good linear relationship is seen when Intralipid concentrations are between 1% and 2.5% (shown by the dashed line in Figure 3(d)). While changes of image intensity due to light scattering may non-linearly depend on the Intralipid concentration [21], such

non-linearity is relatively small and can be nonsignificant within the scattering property range for biological tissues [22, 23]. Thus, the optical density measured from the CCD camera is linearly proportional to the light scattering changes, at the first-order approximation.

**2.4. Optode Geometry for CCD-Camera-Based DOT.** Instrument noise may appear during the measurements with a CCD camera that serves as multiple detectors; dark noise and nonuniformity of CCD chip sensitivity are two noise sources. Another problem often encountered is associated with the limited dynamic range of a CCD camera: when an individual pixel of the CCD array reaches its maximal intensity, the individual pixel well is occupied by electrons which can also overflow into the neighboring pixel wells. Such an overflow of electrons thereby distorts the actual signals not only at the saturated pixel but also at several adjacent pixels. In order to minimize the problem of signal saturations, the source fibers in this study were arranged around the FOV of the CCD camera, as shown in Figure 4. Such geometry can also be utilized while keeping the source fibers within the FOV.

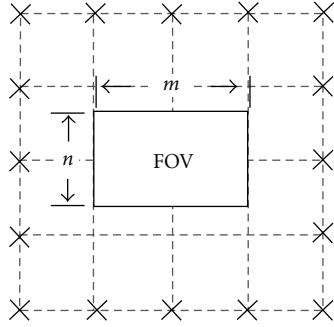


FIGURE 4: Optode geometry for CCD-camera-based DOT system. The dimension of FOV was  $m \times n$  in  $\text{mm}^2$ . X represents possible locations of source fibers.

As shown in Figure 4, the dimension of FOV of the CCD camera was  $m \times n$   $\text{mm}^2$ . Instead of using physical detectors, virtual detectors were used in this noncontact CCD camera imaging system. Virtual detectors refer to groups of CCD pixels combined within FOV of the CCD camera. The signal-to-noise ratio (SNR) at selected locations can be enhanced by averaging the signals of all pixels selected. For example, if we selected  $10 \times 10$  pixels to be binned as a virtual detector, the entire FOV would have a total number of  $\sim 50 \times 66$  virtual detectors for the DOT measurements. This implies that a CCD-camera-based DOT system may serve as a high-density imaging device with an easy-to-change detector array by grouping the pixels in different ways as detectors.

## 2.5. Theory of Image Reconstruction

**2.5.1. Conventional Image Reconstruction in DOT.** The photon propagation in a highly scattering medium follows the diffusion equation, and the analytic solution of the diffusion equation can be utilized to study optical signal changes due to absorption perturbation, as given by

$$\begin{aligned} \Delta\text{OD} &= -\log\left(\frac{\Phi_{\text{pert}}}{\Phi_0}\right) = -\frac{1}{2.3} \ln\left(\frac{\Phi_{\text{pert}}}{\Phi_0}\right) \\ &= \frac{1}{2.3} \int \Delta\mu_a(r)L(r)dr, \end{aligned} \quad (3)$$

where  $\Delta\text{OD}$  is the change in optical density.  $\Phi_0$  is the photon fluence in a semi-infinite, homogeneous medium, and  $\Phi_{\text{pert}}$  is the photon fluence with absorbers embedded.  $L$  is the effective pathlength of light through the tissue experiencing the absorption change. While (3) is known as the modified Beer-Lambert law, it can be generalized in a matrix form and written as  $\mathbf{y} = \mathbf{Ax}$ , where matrix  $\mathbf{y}$  represents measured changes in optical density from all the measurements, matrix  $\mathbf{x}$  corresponds to a volumetric vector of the unknown perturbation in absorption coefficient in the volume under study, and matrix  $\mathbf{A}$  describes the sensitivity of measurements to the change in absorption within each voxel in the medium.

However, solving  $\mathbf{y} = \mathbf{Ax}$  is nontrivial, involving an underdetermined, ill-posed inverse problem because the number of measurements is much fewer than the number of

unknowns (i.e., voxels) to be reconstructed. In the current research field, to reconstruct a DOT image, the Tikhonov regularization [24] method has been employed; an image of  $\mathbf{x}$  can be given by

$$\hat{\mathbf{x}} = \mathbf{A}^T (\mathbf{AA}^T + \alpha \mathbf{S}_{\text{max}} \mathbf{I})^{-1} \mathbf{y}, \quad (4)$$

where  $\hat{\mathbf{x}}$  is the reconstructed image of absorption perturbation;  $\mathbf{I}$  is the identity matrix;  $\mathbf{S}_{\text{max}}$  is the maximal singular value of matrix  $\mathbf{AA}^T$ , and  $\alpha$  is the regularization parameter.

**2.5.2. Depth Compensation Algorithm.** Because of the severe attenuation in light intensity as increase of propagation depth, the measurement sensitivity of DOT in deep tissue is significantly lower than that in superficial tissue. In order to overcome this problem, a new approach of DCA has been recently developed by introducing a weighted matrix  $\mathbf{M}$ , which has a pseudo-exponential magnitude with depth to counterbalance the loss of sensitivity of  $\mathbf{A}$  in deep layers. The weighted matrix  $\mathbf{M}$  is formed as

$$\mathbf{M} = \text{diag}(M(A_L), M(A_{L-1}), \dots, M(A_2), M(A_1))^\gamma, \quad (5)$$

where  $M(A_i)$  represents the maximum singular values for measurement sensitivities within the particular layer  $i$  which is decomposed from forward matrix  $\mathbf{A}$ ;  $\gamma$  is an adjustable power and can be varied between 0 and 3. The detailed derivation and validation of DCA can be found in references [18, 19]. The key component in DCA is the formation of a transformation matrix  $\mathbf{A}^\#$ , as defined by  $\mathbf{A}^\# = \mathbf{AM}$ . Then  $\mathbf{A}^\#$  is used to replace the original sensitivity matrix,  $\mathbf{A}$ , in (4). The reconstructed image to be obtained using DCA can be written as follows:

$$\hat{\mathbf{x}}_{\text{DCA}} = (\mathbf{AM})^T (\mathbf{AM}(\mathbf{AM})^T + \alpha \mathbf{S}'_{\text{max}} \mathbf{I})^{-1} \mathbf{y}, \quad (6)$$

where  $\mathbf{S}'_{\text{max}}$  is the maximum eigenvalue of  $\mathbf{AM}(\mathbf{AM})^T$ . Notice that  $\hat{\mathbf{x}}_{\text{DCA}}$  in (6) is not equal to  $\hat{\mathbf{x}}$  in (4) since matrix  $\mathbf{M}$  is empirically introduced. It is known now that (6) yields minimum error in depth localization for reconstructed NIRS images, while the trade-off of DCA is an inaccurate quantification for absorption perturbation.

As demonstrated in our recent publications [18, 19], the power of depth compensation is controlled by the exponent parameter of  $\gamma$  in  $\mathbf{M}$ . The larger the  $\gamma$  value is, the larger the weight is to compensate the measurement sensitivity toward a deeper layer, and vice versa. An inappropriate selection of  $\gamma$  could lead to overcompensation and give rise to inaccurate results. Our previous studies have suggested an optimal range of  $\gamma$  to be 1.0–1.6 for accurate depth localization using a fiber-based DOT system. In this study, we need to select and confirm a suitable range of  $\gamma$  for a CCD-camera-based DOT system.

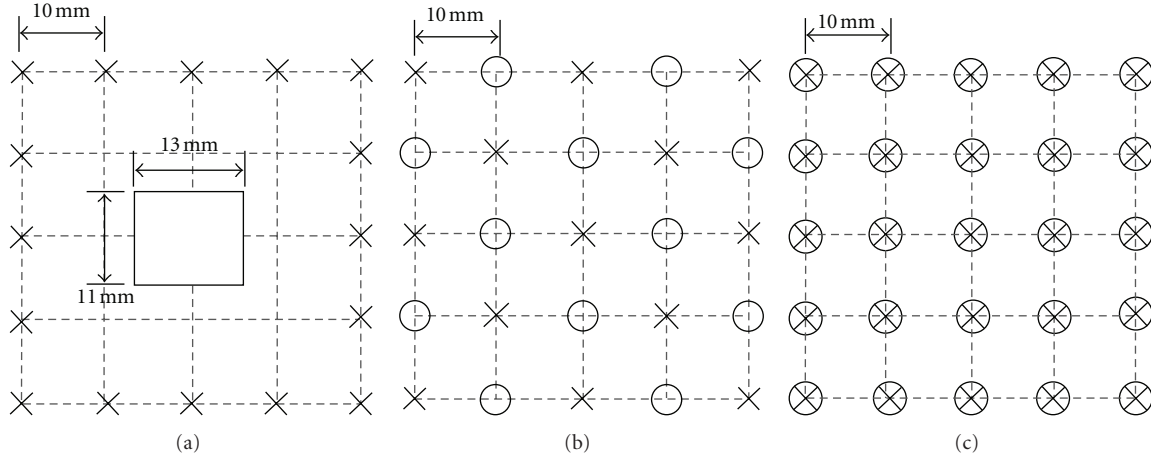


FIGURE 5: Scheme of optode geometries used in the simulation study. (a) to (c) are corresponded to G-I to G-III. Notice that the dimension of all dashed unit squares is  $10 \times 10 \text{ mm}^2$ . (x: source fibers; o: detector fibers;  $\otimes$ : bifurcated fibers).

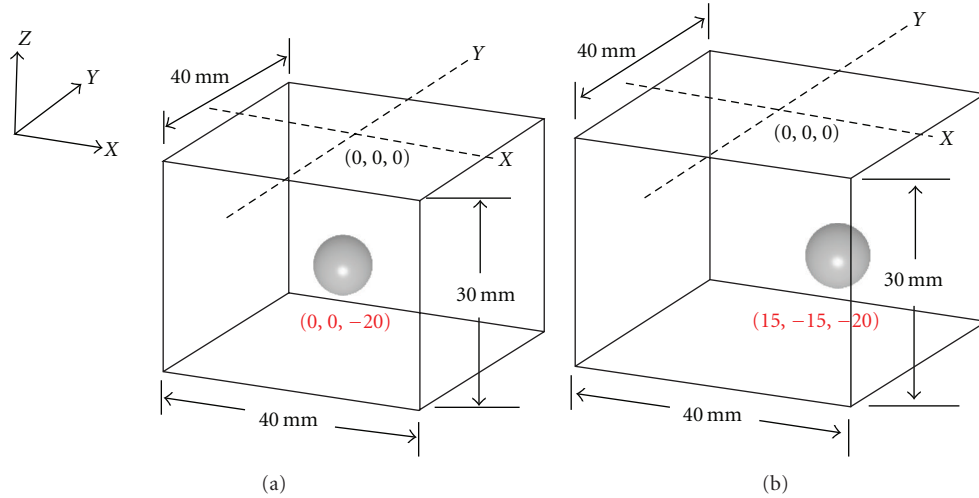


FIGURE 6: Schematic diagram of setups used in simulation study. (a) Setup I: the inclusion was located right below the center of measurement plane. (b) Setup II: the inclusion was located close to the right side corner of the measurement volume.

### 3. Results

**3.1. Computer Simulations.** To evaluate reconstruction performances using the source-camera geometry given in Section 2.4 (also replotted in Figure 5(a) and denoted as G-I), we performed computer simulations and compared the results with those that were derived using the source-detector geometries commonly seen in the fiber-based DOT system (shown in Figures 5(b) and 5(c)). Several sets of simulations were carried out under the conditions of (1) using different numbers of sources and virtual detectors, (2) without and (3) with utilization of DCA.

As shown in Figure 5(a), sixteen sources were used in G-I. In terms of the number of virtual detectors, we defined the dimension of FOV to be  $13 \times 11 \text{ mm}^2$  and the dimension of each virtual detector to be  $1 \text{ mm}^2$ . Therefore, there were

a total of  $13 \times 11 = 143$  virtual detectors used in the simulations. The geometry shown in Figure 5(b) (G-II) is commonly used optode geometry with sources and detectors being alternately placed. The geometry given in Figure 5(c) (G-III) exhibits the optode setup with bifurcated fibers, that is, each fiber can serve as a source and detector.

The reconstruction performances were evaluated by two parameters: (1) the position error (PE) and (2) contrast-to-noise ratio (CNR) [25]. PE is the distance from the center of actual object to the center of the reconstructed object. The reconstructed object was defined by the pixels with values above half of the maximum value. CNR indicates whether the reconstructed object can be clearly distinguished from the background. A reconstructed image was divided into two regions: volume of interest (VOI) and volume of background (VOB). VOI was defined by the location and

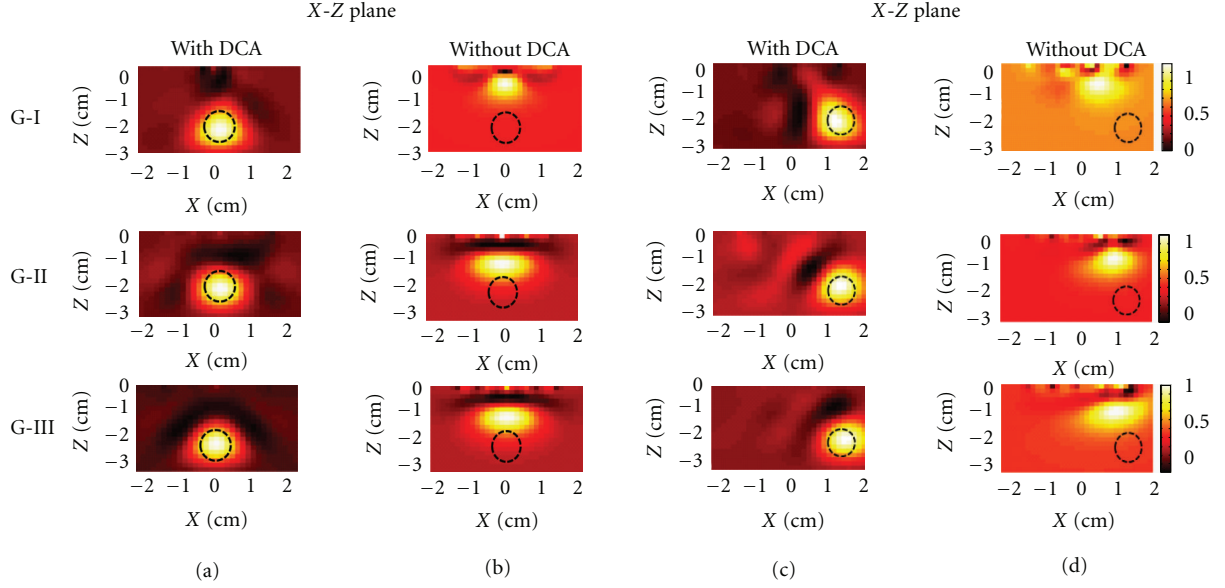


FIGURE 7: Reconstructed DOT images of a single object in X-Z plane: (a) and (c) with DCA ( $\gamma = 1.3$ ), and (b) and (d) without DCA. Top-to-bottom rows were obtained from G-I to G-III (Figure 5).

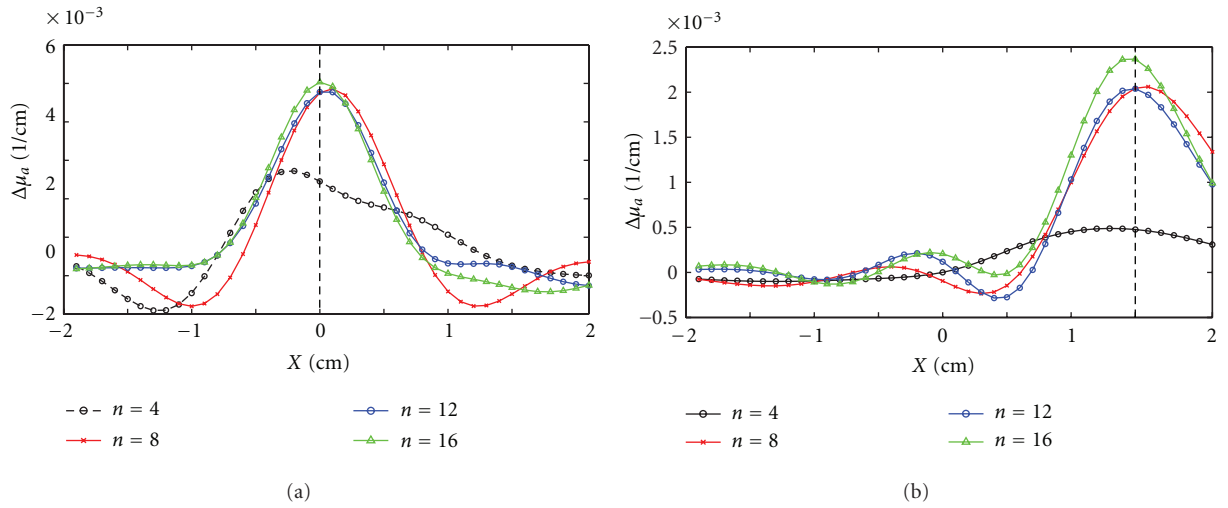


FIGURE 8: Profiles of reconstructed  $\Delta\mu_a$  values along  $x$ -axis for (a) experimental Setup I and (b) experimental Setup II. Dashed vertical lines represent the actual location of the inclusion in  $x$ -axis.

size of the reconstructed object. VOB was defined by the remaining volume of the image. CNR can be calculated by

$$\text{CNR} = \frac{\mu_{\text{VOI}} - \mu_{\text{VOB}}}{[w_{\text{VOI}}\sigma_{\text{VOI}}^2 + w_{\text{VOB}}\sigma_{\text{VOB}}^2]^{1/2}}, \quad (7)$$

where  $w_{\text{VOI}}$  and  $w_{\text{VOB}}$  are the weight factors of the VOI and VOB relative to the entire volume (i.e., VOI or VOB divided by the entire volume),  $\mu_{\text{VOI}}$  and  $\mu_{\text{VOB}}$  are the mean values of object and background volumes in a 3D reconstructed image, and  $\sigma_{\text{VOI}}$  and  $\sigma_{\text{VOB}}$  are the respective standard deviations.

**3.1.1. Image Reconstruction of Embedded Objects.** In the simulation, we considered a homogeneous semi-infinite medium with a volume of  $40 \times 40 \times 30 \text{ mm}^3$  (Figure 6). The origin

of the coordinates was set at the center of top surface, as marked in the figure; this surface was also chosen to be the measurement surface in the simulation. As commonly used, a set of absorption and reduced scattering coefficients of  $\mu_a = 0.1 \text{ cm}^{-1}$  and  $\mu'_s = 10 \text{ cm}^{-1}$  were selected to simulate the background tissue.

Two different setups were utilized to evaluate the performances of optode geometries: Setup 1 is shown in Figure 6(a), where a spherical absorber with an 8 mm diameter was placed at  $(X, Y, Z) = (0, 0, -20)$  (in mm), with a 3:1 contrast ratio in  $\mu_a$  relative to the background  $\mu_a$ . By looking at the optode geometry of the CCD-camera-based DOT imaging system, it is noticed that there are fewer overlapping measurements near four corners of FOV

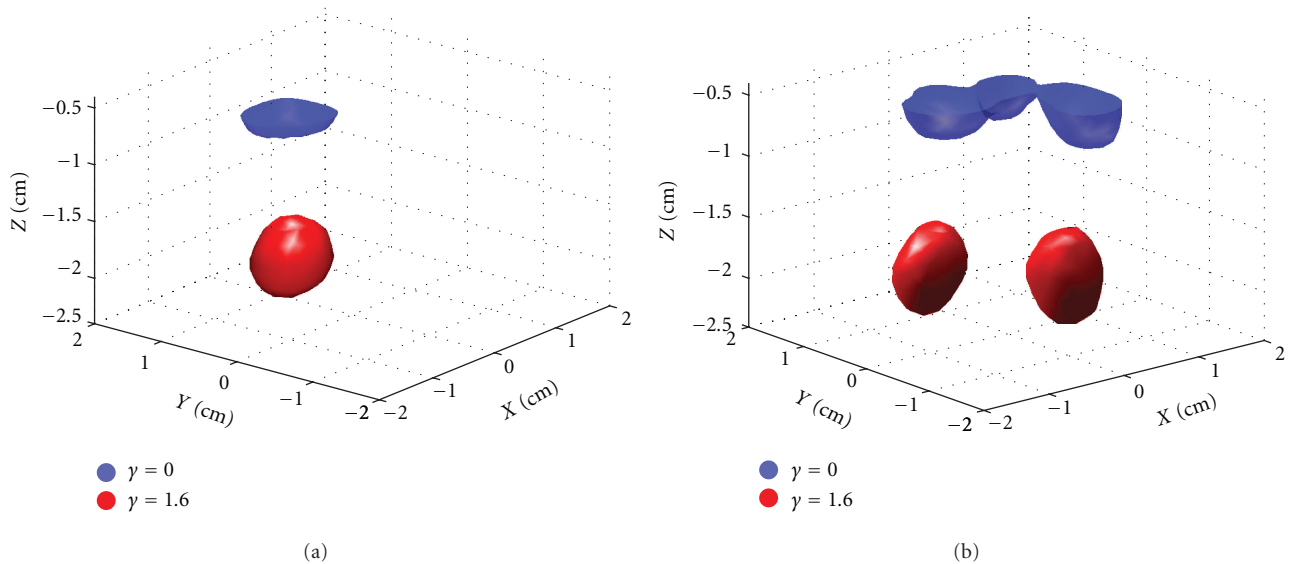


FIGURE 9: Three dimensional plots of reconstructed images for (a) one inclusion with DCA ( $\gamma = 1.6$ ) and without DCA (i.e.,  $\gamma = 0$ ), and (b) two inclusions with DCA ( $\gamma = 1.6$ ) and without DCA ( $\gamma = 0$ ). Voxels with the reconstructed absorption values above 80% of the maximum value are selected as reconstructed objects.

of the camera, as compared to the center of FOV. This is because more overlapping measurements occur near the center of FOV when we pair most of the virtual detectors with given light sources in the current source-camera setup. It has also shown that a higher measurement density does not necessarily improve the spatial resolution significantly [26]. Thus, to evaluate and compare the effect of the number of overlapping measurements at the four corners, in Setup 2, one spherical absorber was placed near the right corner of the medium with respect to Setup 1, as shown in Figure 6(b). A random Gaussian noise of 1% in amplitude was added to the simulated measurement data. DCA was employed with a compensation power of  $\gamma = 1.3$ .

The reconstructed images in the X-Z plane from both setups are shown in Figure 7: Figures 7(a) and 7(b) are obtained from Setup 1 with the absorber placed at the center of measurement plane, while Figures 7(c) and 7(d) result from Setup 2. Also, the three rows from top to bottom in the figure correspond to the fiber-camera or fiber-fiber geometry of G-I to G-III, respectively. Figures 7(b) and 7(d) clearly show that the reconstructed images for all geometries are pulled towards the superficial surface along Z direction when DCA is not used or  $\gamma = 0$ . After DCA was employed with  $\gamma = 1.3$ , the reconstructed object was reconstructed at the expected depth (Figures 7(a) and 7(c)). By comparing the reconstructed images using the three geometries of G-I to G-III, we can see that the overall qualities of DOT images are all similar. However, in Figure 7(c), it is noticed that the DOT images with G-II and G-III exhibit a relatively better shape for the reconstructed objects, while G-I leads to a little distorted profile (tilted to the center) when the absorber was close to the edge of the imaging medium.

To further quantify the comparison among the three geometries, we have calculated respective values of CNR and PE from each geometry (Figure 5) and for two simulation

setups (Figure 6), and the corresponding values are listed in Table 1. It is clearly seen that there are significant improvements of PE values with DCA, as we expected, for both setups, while the overall PE values in Setup 1 are better than those in Setup 2. Next, we focus on only the data with DCA: by close inspection on G-I to G-III for Setup 1, we observe that CNR values from all three optode geometries are not greatly different although G-III has a little higher CNR. A similar trend can be seen for Setup 2. Regarding PE values obtained only with DCA, no noticeable difference appears for all three geometries (less than 1 mm) in either of the setups.

Overall, the computer simulation results confirm that the geometry of G-I, which can be utilized as a CCD-camera-based DOT system, is able to deliver excellent DOT images at the same quality level as the other two fiber-based DOT systems do. Given the simplicity, low cost, and portability of such a system, it may be preferred in preclinical, small animal studies.

**3.1.2. Optimization of the Number of Sources.** It is common that the space available in preclinical studies around animals is restricted or limited to allow for many optodes. Thus, we next further investigate a possible optimal number of optodes that can still permit a reasonably good DOT image. In geometry G-I, only source fibers need to be arranged around FOV of the CCD camera. Therefore, several computer simulations were performed based on both setups (Figure 6) used in Section 3.1.1 in order to optimize the numbers of sources and virtual detectors. Specifically, the light sources were placed symmetrically around the origin to prevent the distortion of reconstructed images.

Figure 8 shows several cross-section profiles of the reconstructed  $\Delta\mu_a$  values along x-axis with different numbers of sources while the absorber was placed at center (Figure 8(a))

TABLE 1: Summary of the CNR and PE values for three geometries.

	Setup 1 (absorber at center)						Setup 2 (absorber on side)					
	G-I		G-II		G-III		G-I		G-II		G-III	
	W	W/O	W	W/O	W	W/O	W	W/O	W	W/O	W	W/O
CNR	5.66	4.39	5.65	4.12	5.73	4.58	5.45	5.46	5.61	5.62	6.47	4.72
PE(cm)	0.20	0.82	0.20	0.75	0.20	0.72	0.36	0.81	0.35	0.79	0.35	0.78

\* W: with DCA; W/O: without DCA.

TABLE 2: Summary of the CNR, PE, and CPU time for different numbers of sources.

Numbers of source	Setup I (absorber at center)				Setup II (absorber on side)			
	4	8	12	16	4	8	12	16
CNR	4.27	5.66	5.67	5.83	1.24	4.42	4.51	4.58
PE (cm)	0.41	0.20	0.20	0.20	0.88	0.35	0.32	0.32
CPU time (sec)	27.1	102.1	209.4	289.2	27.1	102.1	209.4	289.2

and close to the edge of medium (Figure 8(b)). It is clear from this figure that an increase in number of the sources can lead to an enhanced reconstructed contrast, and thus resulting in a clearer DOT image. However, no substantial difference is observed in absorption contrast while the number of sources is increased from 8 to 12 and further to 16 in both cases.

More quantitatively, we have calculated CNR and PE values for all four cases with the number of sources of  $n = 4, 8, 12,$  and  $16$ . The respective values are given in Table 2. It shows unambiguously that no difference in PE and CNR appears when  $n$  has changed from 8 to 16. However, the computational time for  $n = 16$  is  $\sim 2.5$  times longer than that for  $n = 8$ . Hence, for practical use, we would suggest to utilize eight sources instead of twelve or more, which offer the same quality of DOT images but have less complexity of a DOT system.

**3.2. Phantom Experiments and Results.** Besides the computational investigation given above, we have also performed laboratory phantom studies to confirm what we found. A 1% Intralipid solution was used to generate the liquid tissue phantom (Figure 1(b)) with background optical properties of  $\mu_a = 0.1 \text{ cm}^{-1}$  and  $\mu'_s = 10 \text{ cm}^{-1}$ . A spherical gelatin inclusion of 8 mm in diameter was embedded 20 mm below the liquid surface, with a 2.5:1 contrast ratio in absorption between the inclusion and background. A broad-band white light source (Illumination Technologies, Inc. Model 3900, quartz-tungsten halogen lamp) was used, and a 12-bit CCD camera (SamBa Q34 with Navitar Zoom 7000 lens) was employed as the detector. The FOV of the camera was  $13 \times 11 \text{ mm}^2$ , the same dimension as used in the simulations. The total FOV was divided into 143 ( $13 \times 11$ ) virtual detectors, meaning that each virtual detector had  $38 \times 38$  pixels. In this study, 8 light sources were connected to and controlled by a multiplexer (Avantes Inc. Multiplex Channels  $1 \times 16$ ), as shown in Figure 1(a). A total of  $8 \times 143$  source-detector (virtual) pairs were pooled to perform DOT image reconstructions with utilization of DCA. The total volumetric imaging space was  $40 \times 40 \times 30 \text{ mm}^3$ . Moreover,

another similar experiment was repeated with two identical inclusions embedded at 20 mm depth.

3D reconstructed images are shown in Figures 9(a) and 9(b) for the phantom experiments described above. To obtain 3D plots, we have selected the reconstructed absorption values at 80% of its maximum as a volume threshold in order to form the imaged object. From both Figures 9(a) and 9(b), it is clear that the embedded objects can be successfully reconstructed at a relatively accurate depth when DCA is applied. However, because of the diffuse nature of light in tissues, the volume ratio between the reconstructed and real object is around 2:1, which also depends on the threshold value selected and the depth of the embedded inclusion.

## 4. Conclusion

In this study, we present the feasibility of using a CCD-camera-based system combined with our newly developed DCA to form volumetric diffuse optical tomography. We performed both computer simulations and laboratory phantom experiments to confirm our findings. Although only a 12-bit CCD camera was utilized in our experiment setup, the optical signals from 20 mm depth could still be detected by grouping several pixels from the CCD-camera readings as virtual detectors. Overall, we are confident to state that because of its simplicity, low cost, and portability of such a system, a CCD-camera-based DOT may become a highly appropriated imaging tool to be applied in preclinical, small animal studies. For example, this approach may present a great promise for 3D localization of an embedded anomaly tissue, such as a tumor embedded in a small animal.

For future work, *in vivo* animal measurements are planned for both brain imaging and tumor detection to further validate volumetric imaging by combining a CCD-camera-based DOT system with DCA. In addition, optimization of the source-detector geometry will be further investigated since different combinations of source-detector arrangement may result in different qualities of reconstructed images.

## Authors' Contribution

The first two authors contributed equally to the paper.

## Acknowledgments

This work was supported in part by NINDS from the NIH (5R33NS052850-04). The authors also acknowledge the PMI DOT imaging toolbox.

## References

- [1] N. Iftimia and H. Jiang, "Quantitative optical image reconstruction of turbid media by use of direct-current measurements," *Applied Optics*, vol. 39, no. 28, pp. 5256–5261, 2000.
- [2] A. M. Siegel, J. J. A. Marota, and D. A. Boas, "Design and evaluation of a continuous-wave diffuse optical tomography system," *Optics Express*, vol. 4, no. 8, pp. 287–298, 1999.
- [3] D. A. Boas, A. M. Dale, and M. A. Franceschini, "Diffuse optical imaging of brain activation: approaches to optimizing image sensitivity, resolution, and accuracy," *NeuroImage*, vol. 23, no. 1, pp. S275–S288, 2004.
- [4] B. R. White, A. Z. Snyder, A. L. Cohen et al., "Resting-state functional connectivity in the human brain revealed with diffuse optical tomography," *NeuroImage*, vol. 47, no. 1, pp. 148–156, 2009.
- [5] A. Custo, D. A. Boas, D. Tsuzuki et al., "Anatomical atlas-guided diffuse optical tomography of brain activation," *NeuroImage*, vol. 49, no. 1, pp. 561–567, 2010.
- [6] D. R. Leff, O. J. Warren, L. C. Enfield et al., "Diffuse optical imaging of the healthy and diseased breast: a systematic review," *Breast Cancer Research and Treatment*, vol. 108, no. 1, pp. 9–22, 2008.
- [7] B. J. Tromberg, B. W. Pogue, K. D. Paulsen, A. G. Yodh, D. A. Boas, and A. E. Cerussi, "Assessing the future of diffuse optical imaging technologies for breast cancer management," *Medical Physics*, vol. 35, no. 6, pp. 2443–2451, 2008.
- [8] G. Xu, D. Piao, C. H. Musgrove, C. F. Bunting, and H. Dehghani, "Trans-rectal ultrasound-coupled near-infrared optical tomography of the prostate—part I: simulation," *Optics Express*, vol. 16, no. 22, pp. 17484–17504, 2008.
- [9] Z. Jiang, D. Piao, G. Xu et al., "Trans-rectal ultrasound-coupled near-infrared optical tomography of the prostate—part II: experimental demonstration," *Optics Express*, vol. 16, no. 22, pp. 17505–17520, 2008.
- [10] J. P. Sacha, M. D. Cockman, T. E. Dufresne, and D. P. Trokhan, "Quantification of regional fat volume in rat MRI," in *Medical Imaging 2003: Physiology and Function: Methods, Systems, and Applications*, vol. 5031 of *Proceedings of SPIE*, pp. 289–297, February 2003.
- [11] A. Laib, O. Barou, L. Vico, M. H. Lafage-Proust, C. Alexandre, and P. Rügsegger, "3D micro-computed tomography of trabecular and cortical bone architecture with application to a rat model of immobilisation osteoporosis," *Medical and Biological Engineering and Computing*, vol. 38, no. 3, pp. 326–332, 2000.
- [12] D. Sorger, M. Patt, P. Kumar et al., "[<sup>18</sup>F]Fluoroazomycin-arabinofuranoside (18FAZA) and [<sup>18</sup>F]Fluoromisonidazole (18FMISO): a comparative study of their selective uptake in hypoxic cells and PET imaging in experimental rat tumors," *Nuclear Medicine and Biology*, vol. 30, no. 3, pp. 317–326, 2003.
- [13] C. Vanhove, T. Lahoutte, M. Defrise, A. Bossuyt, and P. R. Franken, "Reproducibility of left ventricular volume and ejection fraction measurements in rat using pinhole gated SPECT," *European Journal of Nuclear Medicine and Molecular Imaging*, vol. 32, no. 2, pp. 211–220, 2005.
- [14] J. P. Culver, T. Durduran, D. Furuya, C. Cheung, J. H. Greenberg, and A. G. Yodh, "Diffuse optical tomography of cerebral blood flow, oxygenation, and metabolism in rat during focal ischemia," *Journal of Cerebral Blood Flow and Metabolism*, vol. 23, no. 8, pp. 911–924, 2003.
- [15] G. Gulsen, O. Birgul, M. B. Unlu, R. Shafiha, and O. Nalcioglu, "Combined diffuse optical tomography (DOT) and MRI system for cancer imaging in small animals," *Technology in Cancer Research and Treatment*, vol. 5, no. 4, pp. 351–363, 2006.
- [16] Q. Zhao, L. Ji, and T. Jiang, "Improving depth resolution of diffuse optical tomography with a layer-based sigmoid adjustment method," *Optics Express*, vol. 15, no. 7, pp. 4018–4029, 2007.
- [17] B. W. Pogue, T. O. McBride, J. Prewitt, U. L. Österberg, and K. D. Paulsen, "Spatially variant regularization improves diffuse optical tomography," *Applied Optics*, vol. 38, no. 13, pp. 2950–2961, 1999.
- [18] H. Niu, Z. Lin, F. Tian, S. Dhamne, and H. Liu, "Comprehensive investigation of three-dimensional diffuse optical tomography with depth compensation algorithm," *Journal of Biomedical Optics*, vol. 15, no. 4, article 046005, 2010.
- [19] H. Niu, F. Tian, Z. Lin, and H. Liu, "Development of a compensation algorithm for accurate depth localization in diffuse optical tomography," *Optics Letters*, vol. 35, no. 3, pp. 429–431, 2010.
- [20] S. B. Howell, *Handbook of CCD Astronomy*, 2000.
- [21] S. C. Kanick, U. A. Gamm, M. Schouten, H. J. Sterenberg, D. J. Robinson, and A. Amelink, "Measurement of the reduced scattering coefficient of turbid media using single fiber reflectance spectroscopy: fiber diameter and phase function dependence," *Biomedical Optics Express*, vol. 2, pp. 1687–1702, 2011.
- [22] M. Johns, C. A. Giller, D. C. German, and H. Liu, "Determination of reduced scattering coefficient of biological tissue from a needle-like probe," *Optics Express*, vol. 13, no. 13, pp. 4828–4842, 2005.
- [23] G. Zonios and A. Dimou, "Modeling diffuse reflectance from semi-infinite turbid media: application to the study of skin optical properties," *Optics Express*, vol. 14, no. 19, pp. 8661–8674, 2006.
- [24] S. R. Arridge, "Optical tomography in medical imaging," *Inverse Problems*, vol. 15, no. 2, pp. R41–R49, 1999.
- [25] Q. Zhao, L. Ji, and T. Jiang, "Improving performance of reflectance diffuse optical imaging using a multicentered mode," *Journal of Biomedical Optics*, vol. 11, no. 6, Article ID 064019, 2006.
- [26] F. Tian, G. Alexandrakis, and H. Liu, "Optimization of probe geometry for diffuse optical brain imaging based on measurement density and distribution," *Applied Optics*, vol. 48, no. 13, pp. 2496–2504, 2009.

## Research Article

# Megavoltage X-Ray Imaging Based on Cerenkov Effect: A New Application of Optical Fibres to Radiation Therapy

A. Teymurazyan<sup>1</sup> and G. Pang<sup>1, 2, 3, 4</sup>

<sup>1</sup>Imaging Research, Sunnybrook Health Sciences Centre and Department of Medical Biophysics, University of Toronto, Toronto, ON, Canada M4N 3M5

<sup>2</sup>Odette Cancer Centre, Toronto, ON, Canada M4N 3M5

<sup>3</sup>Department of Radiation Oncology, University of Toronto, Toronto, ON, Canada M5G 2M9

<sup>4</sup>Department of Physics, Ryerson University, Toronto, ON, Canada M5B 2K3

Correspondence should be addressed to A. Teymurazyan, teymuraz@sri.utoronto.ca

Received 14 July 2011; Revised 19 September 2011; Accepted 20 September 2011

Academic Editor: Baohong Yuan

Copyright © 2012 A. Teymurazyan and G. Pang. This is an open access article distributed under the Creative Commons Attribution License, which permits unrestricted use, distribution, and reproduction in any medium, provided the original work is properly cited.

A Monte Carlo simulation was used to study imaging and dosimetric characteristics of a novel design of megavoltage (MV) X-ray detectors for radiotherapy applications. The new design uses Cerenkov effect to convert X-ray energy absorbed in optical fibres into light for MV X-ray imaging. The proposed detector consists of a matrix of optical fibres aligned with the incident X rays and coupled to an active matrix flat-panel imager (AMFPI) for image readout. Properties, such as modulation transfer function, detection quantum efficiency (DQE), and energy response of the detector, were investigated. It has been shown that the proposed detector can have a zero-frequency DQE more than an order of magnitude higher than that of current electronic portal imaging device (EPID) systems and yet a spatial resolution comparable to that of video-based EPIDs. The proposed detector is also less sensitive to scattered X rays from patients than current EPIDs.

## 1. Introduction

Radiation therapy is widely used today to treat patients with tumors [1]. Megavoltage (MV) X-ray beams generated from a linear accelerator are commonly used to deliver the prescribed radiation dose to the tumor while minimizing the dose to the surrounding healthy tissues. The geometric accuracy of such treatment is crucial for its success. Currently, there are a number of ways to verify the positional accuracy of the treated target. One of them is to use MV cone beam CT (MV-CBCT) to locate the position of the target in the treatment room prior to the start of the treatment [2, 3]. MV-CBCT uses an electronic portal imaging device (EPID) [4] attached to the LINAC to acquire CT data by rotating the MV X-ray source (emitting a cone beam) and the EPID around the patient. One of the main challenges with this approach is that the imaging dose currently required to achieve sufficient soft tissue contrast to visualize and delineate a soft tissue target; for example, the prostate is prohibitively large for daily

verification. This is due to the poor X-ray absorption, that is, low quantum efficiency (QE) of the EPID used. For most EPIDs developed so far, the QE is typically on the order of 2–4% at 6 MV as compared to the theoretical limit of 100% [5]. This is because the total combined thickness of the energy conversion layer and the metal buildup in most EPIDs is only ~2 mm. In contrast, the first half value layer (HVL) for 6 MV X-ray beams is ~13 mm of lead. Thus, a significant increase of QE is required in order to reduce the dose currently required to visualize and delineate the prostate using MV-CBCT.

Efforts were made previously to build high QE area detectors for MV X-ray imaging in radiotherapy, including (1) the use of a thick CsI(Tl) scintillator to replace the thin phosphor screen in a mirror video-based system [6], (2) the use of solid converters and a gas electron multiplier to detect MV X rays [7], (3) the use of brass tubes filled with gas to detect MV X rays [8], (4) the use of scintillating crystal matrix to replace the phosphor screen in an indirect flat panel [9–11],

and (5) the use of a large number of microstructured plates (with W converters, microsize cavities filled with Xe, and microstrip electrodes) packed together to achieve a QE of up to  $\sim 60\%$  [12]. However, all of these detectors are made of high atomic number (high-Z) materials, which results in a severe overresponse of the EPIDs to low-energy scattered X rays [13, 14].

Recently, this research group introduced a new design of a high QE area detector made of low-Z materials for MV X-ray imaging in radiation therapy [15]. It is based on Cerenkov radiation [16]. Cerenkov radiation (or Cerenkov light) is an electromagnetic “shock-wave” of light produced by a charged particle passing through a dielectric medium with a velocity greater than the speed of light *in the medium*. Figure 1 shows a cross-section of our proposed system (subsequently referred to as Cerenkov portal imaging detector or CPID). It consists of a large area and thick (thickness  $d \sim 10\text{--}30\text{ cm}$ ) fibre-optical taper (FOT) directly coupled to an optically sensitive 2D active matrix flat panel imager (AMFPI). The active matrix is made optically sensitive either with an *a*-Si PIN photodiode at every pixel or a continuous layer of amorphous selenium (*a*-Se) [17]. We note that AMFPI using *a*-Si PIN photodiodes has been used in current low-QE EPIDs for many years, and no significant image artifact due to the nonuniform structure of AMFPI has been found in clinical images [4]. It has also been shown that AMFPI is highly resistant to radiation [18]. The FOT is a matrix of optical fibres, each of which has a diameter of several hundred micrometers and is aligned with the incident X rays (i.e., focused towards the X-ray source) to avoid blur due to oblique incidence of off-axis X rays (Figure 1(a)). This focusing towards the X-ray source can be achieved by an extra coating at the bottom of the otherwise uniform fibres. When MV X rays interact with the FOT, energetic electrons will be produced. Those electrons with energy greater than the threshold energy  $\varepsilon_C$  required for Cerenkov radiation in the fibre material will produce Cerenkov light along their tracks. The light photons produced in a fibre core and emitted within the acceptance angle of the fibre will be guided towards the optical detector, that is, the *optically sensitive AMFPI*, by total internal reflection. The *a*-Se layer (or *a*-Si PIN photodiodes) in the optical detector can in principle be operated in the avalanche mode [19] if necessary to amplify the signal in order to overcome the electronic noise in the active matrix readout.

In this paper, we investigate the feasibility of the new design (i.e., CPID) using Monte Carlo simulation. We have simulated properties of the CPID, such as detection efficiency, modulation transfer function, and energy dependence. The results of our study, presented in this paper, merit the use of optical fibres for MV X-ray imaging applications in radiation therapy.

## 2. Methods and Materials

**2.1. Processes and Cuts Considered in the Monte Carlo Simulation Program.** The simulation program, developed to study the imaging and dosimetric characteristics of the proposed

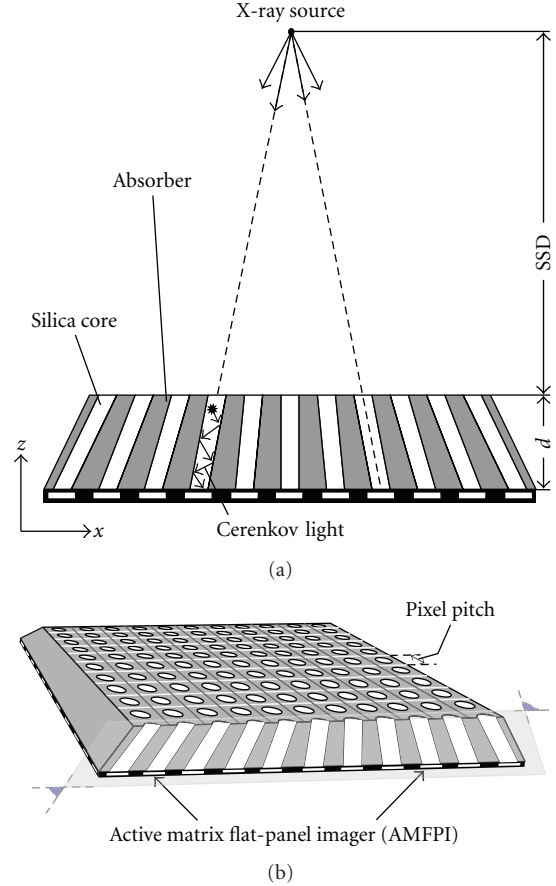


FIGURE 1: Schematic illustration of the proposed CPID. (a) a small cross section of the detector and (b) a 3D view of a small portion of the detector. The detector contains  $931 \times 931$  pixels in the actual simulation.

CPID under irradiation of MV X rays, is based on the Geant4 toolkit (version 9.3 patch-01). The Geant4 toolkit contains physics models covering the interactions of most particle types over a wide energy range (down to 1 keV and below) [20]. Unlike most general-purpose Monte Carlo codes, describing propagation of radiation in matter, it also includes models describing the transport and boundary processes for optical photons. In Geant4 framework, optical photons can be produced by scintillation, Cerenkov effect, or wavelength shifting [20]. For the detector considered in this work, the optical photons are generated by Cerenkov effect only.

The list of particles considered in simulation consists of photons, electrons, positrons, and optical photons. The list of physics processes controlling the particle interactions in the simulation, that is, photoelectric effect, Compton scattering,  $e^+e^-$ -pair production, Rayleigh scattering, multiple scattering, ionization, bremsstrahlung, annihilation, is largely based on the *standard EM* (electromagnetic) *physics list* supplied with Geant4 distribution (class name *G4EmStandardPhysics\_option3*). The EM list was extended to include generation of optical photons via Cerenkov effect. The simulation accounts for optical photon interactions such

as bulk absorption, optical Rayleigh scattering, and optical boundary processes, that is, reflection and refraction [20].

Other modifications to the default parameters of the predefined physics list include the increased number of bins in stopping power ( $S(E) = -dE/dx$ ) and inverse interaction length ( $\lambda(E)$ ) tables from its default value of 220 to 480 bins. The Geant4 applications have a built in, user controllable, production thresholds for secondary particles. These were set to 4.5 mm and 0.16 mm for photons, positrons and electrons, respectively.

**2.2. Detector Configuration as Modeled in Simulation.** A schematic illustration of the proposed detector is given in Figure 1. The active components are fused silica fibres focused towards the X-ray source to avoid blurring due to oblique incidence of off-axis X rays.

The gap between fibres is filled with an opaque material (e.g., water-equivalent black resin) to absorb light that is not guided by the fibres but instead escapes from the side of the fibres. This optically opaque medium, which will subsequently be referred to as the *absorber*, also acts as an energy converter for X rays that would otherwise pass between the fibres without interaction. Furthermore, the absorber reduces the effective range of the electrons (and positrons) generated in the detector, and thus, improves the spatial resolution as well.

The fused silica fibres used in the simulation are cylindrical, each with a fibre core diameter of 0.4 mm and a cladding layer thickness of 0.015 mm, resulting in an outer diameter of 0.43 mm for the whole fibre. The gap between adjacent fibres at the top surface of the detector is 0.005 mm, leading to a pixel pitch of  $0.435 \times 0.435 \text{ mm}^2$  (see Figure 1(b)). The matrix of fused silica fibres contains a total of  $931 \times 931$  elements. The whole detector has a shape of truncated pyramid with optical fibres embedded in the absorber. The total area for the top surface of the detector facing the X-ray source is  $40.455 \times 40.455 \text{ cm}^2$  and the source-to-detector surface distance (SSD) is 157 cm (see Figure 1). The length of the fused silica fibres or the thickness  $d$  of the detector is a variable parameter that primarily influences the QE of the detector. Detector thicknesses of up to 30 cm have been simulated.

**2.3. Detector Materials Considered in the Simulation.** The clear optical fibres for X-ray detection via Cerenkov effect are modeled having a fused silica core (density of  $2.201 \text{ g cm}^{-3}$  and refractive index of  $n_{\text{core}} \approx 1.46$ ). The amount of the light captured and transmitted in fibres depends on the numerical aperture (NA) of the fibre:  $\text{NA} = \sqrt{n_{\text{core}}^2 - n_{\text{cladding}}^2}$ . The numerical aperture of the fibre depends on the cladding material and can range from  $\sim 0.22$  to  $0.66$  (e.g., see technical specifications for fused silica core fibres by Polymicro Technologies LLC). In our simulations, we used  $\text{NA} = 0.48$  (a value characteristic of FSHA fibres by Polymicro Technologies LLC). Fused silica and Teflon have been considered for cladding material in the simulation (as the information on the proprietary polymer cladding for FSHA fibre is unavailable). For fused silica core fibres,

the characteristic absorption length over which a signal is attenuated to  $1/e$  of its original value is  $\sim 20\text{--}100 \text{ m}$  (for  $365\text{--}800 \text{ nm}$  wavelengths). Hence, the absorption of optical photons in fibre cores is a small effect for physical lengths of up to  $\sim 30 \text{ cm}$ . Nevertheless, it was taken into account in the simulation.

The absorber medium between the fibres is assumed to be 100% opaque. The X-ray interaction properties of the water-equivalent black resin are assumed to be the same as that of water in the simulation.

The CPID is simulated as positioned in the center of a  $10 \times 10 \times 10 \text{ m}^3$  volume of air. The primary X rays originate and travel in an air-full environment before reaching the detector.

If not specified, the definitions of all the materials used in the simulation, single element or compound, are taken from the Geant4/NIST materials database.

**2.4. Physics Processes in Detector during Irradiation.** When MV X rays are incident on the CPID, they interact with the optical fibres and the absorber medium in the detector primarily via Compton effect and  $e^+e^-$ -pair production, yielding energetic charged particles (electrons and positrons). From these charged particles, those with sufficient kinetic energy will trigger production of Cerenkov light while traveling in fused silica fibre cores [16]. The light photons, which are produced in a fibre core and emitted within the acceptance angle of the fibre are guided towards the AMFPI by total internal reflection. The light signal that reaches the AMFPI is then converted to an electronic signal and read out by the AMFPI.

**Cerenkov Effect.** The threshold kinetic energy of a charged particle, above which Cerenkov radiation will be generated, can be expressed in terms of refractive index  $n$  of the dielectric medium and the rest mass  $m_0$  of the charged particle:

$$\varepsilon_C = m_0 c^2 \left( \frac{n}{\sqrt{n^2 - 1}} - 1 \right), \quad (1)$$

where  $c$  is the speed of light in vacuum. In silica, electrons or positrons with energy higher than  $\sim 190 \text{ keV}$  will generate Cerenkov light. The simulation takes into account the generation of Cerenkov radiation in the fused silica fibre cores for wavelengths between  $365\text{--}800 \text{ nm}$ . Production of Cerenkov radiation in other components of the detector is negligible due to their opacity or smaller volumes.

**2.5. Simulated Detector Quantities.** The simulation tracks individual histories of all particles: primary, secondary, as well as optical photons, and the energy deposited in the core of each fibre is summed for all tracks and tallied on event-by-event basis. The number of Cerenkov photons created and ones escaping the bottom end of each fibre core is scored on event-by-event basis. Note that an event in the simulation is defined as an instance of an individual X ray and all of its secondaries being tracked through the whole detector.

To study the imaging and dosimetric characteristics of the CPID for clinically relevant X-ray beams, X-ray

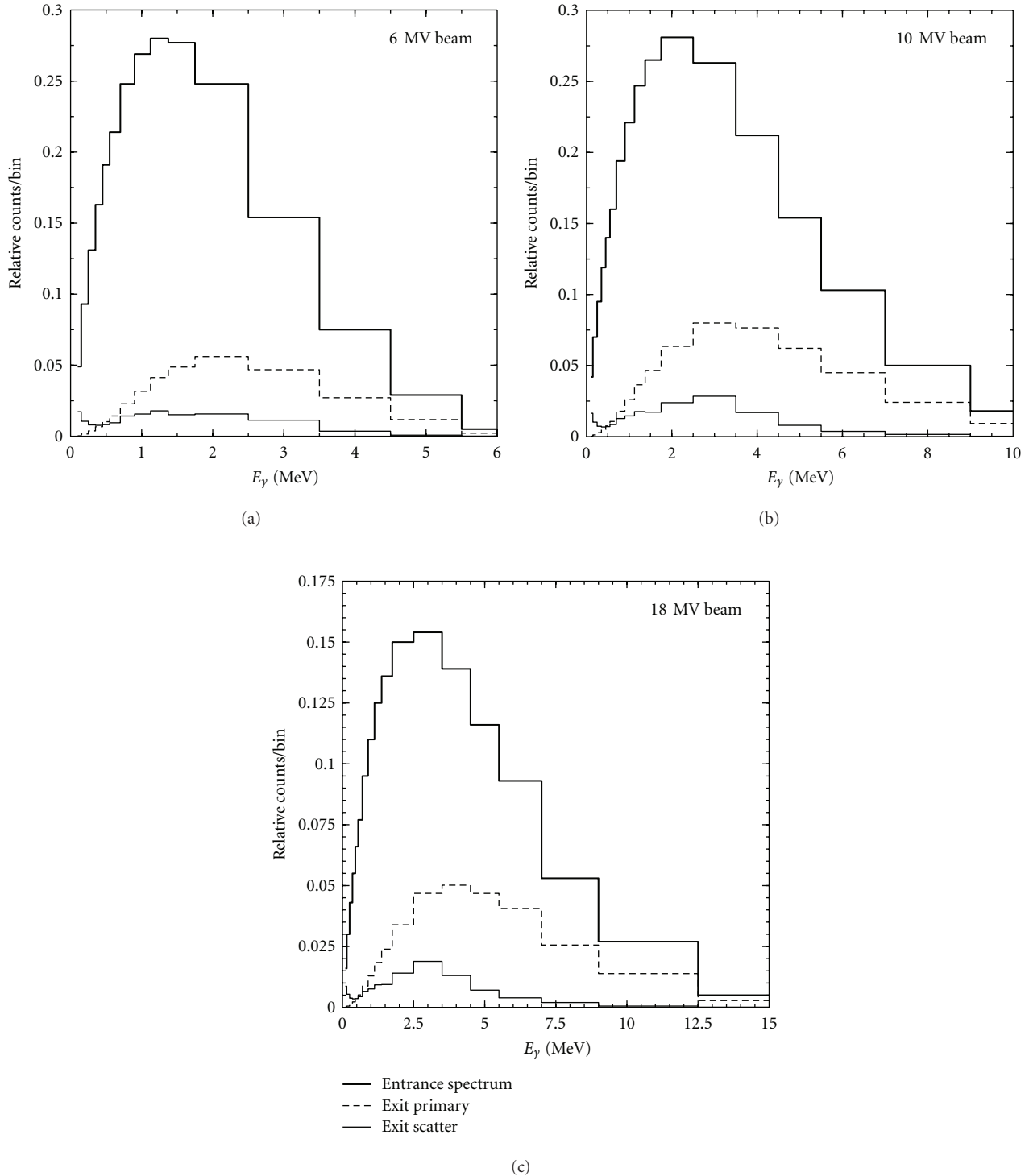


FIGURE 2: X-ray spectra used in the simulation. The entrance spectrum was generated by a treatment planning system (Pinnacle3, Philips), and the exit spectra of X rays were simulated by passing the incident beam (with the entrance spectrum) through a 30 cm thick water phantom.

energy spectra (see Figure 2, entrance spectra) for clinical machines generated by a treatment planning system (Pinnacle3, Philips) were used in the simulation in addition to monoenergetic X-ray beams. For mono-energetic X-ray beams, the energy was varied between 0.2 and 20 MeV.

*2.5.1. Beam Energy Hardening and Scatter due to the Presence of a Patient.* During imaging a patient is positioned between the X-ray source and the EPID. The presence of patient both (1) alters the spectrum of primary X rays exiting the patient and (2) results in generation of secondary particles (X rays,

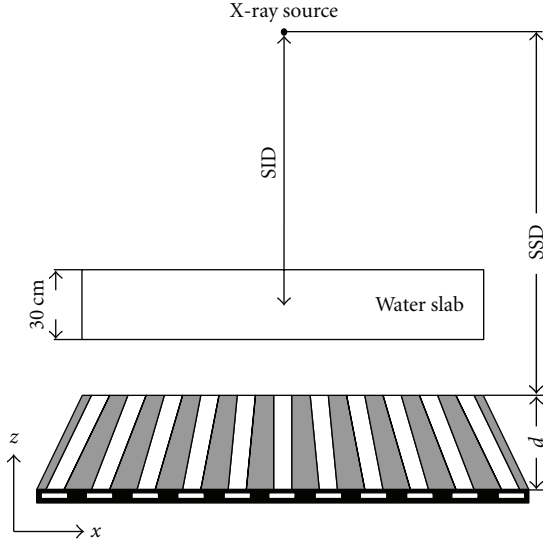


FIGURE 3: Schematic illustration of the geometry used when simulating the primary and scatter components of exit beam due to the presence of a “patient.”

electrons, and positrons) from the patient. To obtain the energy spectra for primary and scattered components of exit beam, the simulation configuration shown in Figure 3 was used. The patient was modeled as a 30 cm thick water slab (phantom) at the isocenter ( $SID = 100$  cm), and the energies and the angles of exit particles were recorded at the detector plane ( $SSD = 157$  cm). A pencil beam sampling the entrance energy spectrum was used to simulate the primary (i.e., nonscattered) and scatter components of exit beam. In our simulations, we investigated the CPID response in absence of a patient (using the entrance spectra from Figure 2) as well as the response in presence of a “patient” (using the energy spectra for scattered and primary components of exit beam).

**2.5.2. Spatial Resolution.** The spatial resolution of the detector can be expressed by the modulation transfer function (MTF) [21]. The one-dimensional MTF is the Fourier transform of the line-spread function [5, 22], that is,

$$MTF(f) = \int_{-\infty}^{\infty} e^{-2i\pi x f} LSF(x) dx, \quad (2)$$

where the line spread function  $LSF(x)$  is defined as

$$LSF(x) = \int_{-\infty}^{\infty} n(x, y) dy. \quad (3)$$

Here  $n(x, y)$  is the point-spread function or the distribution of optical photons that escape the fibres and reach the AMFPI under the irradiation of an infinitely small-size pencil beam. Note that spatial frequencies in this work are referenced to the top surface of the CPID.

To overcome the sampling limitation as in any digital system [12, 21, 23], we varied the location of the incident beam with respect to the detector in the X direction (Figure 1) with a step size of  $53.75 \mu\text{m}$  and sampled over all uniformly

distributed locations within a detector pixel [23]. Prior to applying the Fourier transformation to obtain the MTF, the values of LSF between sampling locations were calculated by linear interpolation. We have also calculated the MTF using a finite-size ( $0.435 \times 0.435 \text{ mm}^2$ ) pencil beam, and the result was essentially identical to that using the infinitely small-size pencil beam.

**2.5.3. CPID Response.** The total mean signal of the detector per pixel under irradiation with X rays of a given energy  $E_\gamma$  can be expressed as a product of the probability of an incident X ray to be detected in CPID  $\eta(E_\gamma)$  (detection efficiency), the mean number of the optical photons reaching the AMFPI per detected X ray  $r(E_\gamma)$  and the incident fluence of X rays  $\Phi(E_\gamma)$ ; namely,

$$R(E_\gamma) = A_d \eta(E_\gamma) r(E_\gamma) \Phi(E_\gamma). \quad (4)$$

Here we assume X-ray fluence from an isotropic point source is incident on the detector, and  $\Phi(E_\gamma)$  represents the total (primary and scattered) fluence reaching a pixel with area  $A_d$ .

Pixel-sized (i.e.,  $0.435 \times 0.435 \text{ mm}^2$ ) pencil beams normally incident at the center of the top surface of the detector were used to simulate the CPID response. Taking advantage of the geometry of the detector, the number of Cerenkov photons reaching the AMFPI was integrated over all fibres on an event-by-event basis to obtain the detector signal per pixel.

**Detection Efficiency.** When MV X rays are incident on the CPID, not all of them interact with the detector and generate a signal in the detector. The detection efficiency  $\eta(E_\gamma)$  is defined as the probability of an incident X ray to produce at least one Cerenkov photon that is guided by the fibre matrix and reaches the AMFPI, irrespective of the position of interaction of the primary X ray in the detector. Throughout this work we assume that the matrix of optical fibres and AMFPI have 100% optical coupling efficiency, and any optical photon incident on the AMFPI will generate an electronic signal in the AMFPI. As such, the detection efficiency quantifies the ability of the CPID to utilize the incident X-ray fluence. We note here that the detection efficiency is equal to or lower than the QE, which is defined as the percentage of incident X rays interacting with the detector. Thus, a high detection efficiency means a high QE.

**Detector Sensitivity.** The quantity  $r(E_\gamma)$ , introduced in (4), represents the efficiency with which the detected X rays are converted into optical photons. The product of  $r(E_\gamma)$  and  $\eta(E_\gamma)$  gives the mean number of optical photons reaching the AMFPI per incident X-ray on the detector, that is, the detector sensitivity. The dependence of detector sensitivity on the energy of incident X rays describes the energy response function of the detector.

**Signal Scatter Fraction.** The presence of a patient, in the beam, results in generation of secondary scattered particles that generally degrade image quality. The contribution to

the total signal per detector pixel from secondary particles is typically presented in form of signal scatter fraction [24]:

$$\text{SF}_{\text{signal}} = \frac{\bar{R}_s}{\bar{R}_s + \bar{R}_p}, \quad (5)$$

where  $\bar{R}_s$  and  $\bar{R}_p$  are the mean signals per pixel due to scattered and primary components of exit beam from the patient, respectively. To further assess the effect of patient scatter on detector performance, we have also calculated the point spread function  $n(x,y)$  in presence of a ‘‘patient’’ (with the pencil beam incident on the ‘‘patient’’) in comparison with that without a patient.

**2.5.4. Detective Quantum Efficiency.** The *detective quantum efficiency* (DQE) is a measure of the image quality of an X-ray detector. The zero spatial frequency DQE of an imaging system can be expressed as [14, 25, 26]

$$\text{DQE}(0) = \frac{M_1^2}{M_2}, \quad (6)$$

where  $M_n$ , the  $n$ th moment of the distribution  $p(m)$  of the number  $m$  of optical photons reaching the AMFPI normalized to the number of incident X rays,  $N_X$ :

$$M_n = \frac{1}{N_X} \sum_m m^n p(m). \quad (7)$$

We note that by definition  $\eta = M_0$ ,  $r = M_1/M_0$  and  $N_X = A_d\Phi$ .

The stochastic nature of interaction of radiation with mater gives rise to the distribution of number of optical photons. For a Cerenkov effect-based detector, the shape of  $p(m)$  is dictated by the distribution of energies of electrons and positrons and their angles with respect to the fibre cores [15]. The general form of (6) and (7) is valid both for discrete X-ray energies and for X-ray energy spectra. In our simulations, we directly sampled the X-ray energy spectra (see Figure 2) to obtain the distribution of the number of optical photons  $p(m)$  for clinical X-ray beams. However, the same result could be produced by averaging the respective moments  $M_n$  (obtained for discrete X-ray energies) over the X-ray energy spectrum. The results for DQE presented in this paper include not only the X-ray quantum absorption noise, but also noise due to variations in Cerenkov light production and transport in fibre cores.

Finally, in case when the noise is white (i.e., frequency independent), the spatial-frequency-dependent DQE( $f$ ) is given by [27]

$$\text{DQE}(f) = \text{DQE}(0) \cdot |\text{MTF}(f)|^2, \quad (8)$$

where  $\text{MTF}(f)$  is the modulation transfer function (see Section 2.5.2).

**2.5.5. Energy Dependence of CPID Dose Response.** To assess the water equivalence of the detector at a given X-ray energy  $E_\gamma$ , we define a ratio  $\alpha(E_\gamma)$  of the value of detector sensitivity

$r(E_\gamma)\eta(E_\gamma)$  to the absorbed dose  $\Gamma(E_\gamma)$  per incident fluence  $\Phi(E_\gamma)$ . Namely,

$$\alpha(E_\gamma) = \frac{\eta(E_\gamma)r(E_\gamma)\Phi(E_\gamma)}{\Gamma(E_\gamma)}, \quad (9)$$

where the definition and calculation of  $\Gamma(E_\gamma)$  is given below (see Section 2.6). For ease of representation, the detector response per unit dose (deposited in water) was normalized to its value at a fixed energy of incident X rays. The value of 2 MeV was chosen as the reference X-ray energy in the analysis, and  $\alpha(E_\gamma)/\alpha(2 \text{ MeV})$  is defined as the *relative response* of the detector to X-ray at a discrete energy for a fixed dose to water. For polyenergetic X-ray beams (see Figure 2), the detector sensitivity  $r(E_\gamma)\eta(E_\gamma)$  and the absorbed dose per incident fluence  $\Gamma(E_\gamma)/\Phi(E_\gamma)$  are separately averaged over the X-ray energy spectrum prior to calculating the relative response.

**2.6. Dose to Water and Fluence-to-Dose Conversion Factors.** The absorbed dose  $\Gamma(E_\gamma)$ , in (9), is defined as the mean dose absorbed in a water slab of an equivalent thickness  $d'$  as if the whole detector were made of pure water; that is,

$$\Gamma(E_\gamma) = \frac{1}{d'} \int_0^{d'} D(E_\gamma, z) dz, \quad (10)$$

where  $D(E_\gamma, z)$  is the dose in water at depth  $z$  [1].

Figure 4 shows the fluence-to-dose conversion factors  $\Gamma(E_\gamma)/\Phi(E_\gamma)$ , assuming a broad parallel beam of normal incidence, for water slab in air environment. The data used in Figure 4 is listed in Table 1. A Geant4-based simulation was developed to calculate the depth-dose curves in a water phantom in presence of surrounding air. It considers a slab of water with surface area of  $300 \times 300 \text{ cm}^2$  and thickness  $d'$  situated in a  $10 \times 10 \times 10 \text{ m}^3$  volume of air. The water slab is logically divided, that is, without physical gaps, into 1 mm thick slices along its depth axis  $Z$ . The depth-dose curves for a broad parallel beam of primary X rays were obtained by considering a pencil beam of  $1 \times 1 \text{ mm}^2$  normally incident on the surface of the water slab. The total energy deposited per unit areal density is scored in a millimeter-thick water slabs at each depth, which gives the depth-dose curve  $D(E_\gamma, z)$ . The primary X rays travel a source-to-surface distance of 157 cm in air.

The CPID thicknesses ( $d = 10, 20, \text{ and } 30 \text{ cm}$ ) investigated in this paper were scaled by the mean physical densities of the detector to obtain the equivalent thicknesses ( $d' = 18.67, 36.30, \text{ and } 53.01 \text{ cm}$ ) of water slabs needed to calculate  $\Gamma(E_\gamma)$ .

### 3. Results

**3.1. Spatial Resolution.** The modulation transfer functions (MTFs) of the CPID for various detector thicknesses  $d$  at 6 MV and 10 MV are shown in Figure 5. The entrance spectra from Figure 2 were used in the simulation. It can be seen that the MTF of the detector decreases at all frequencies with the

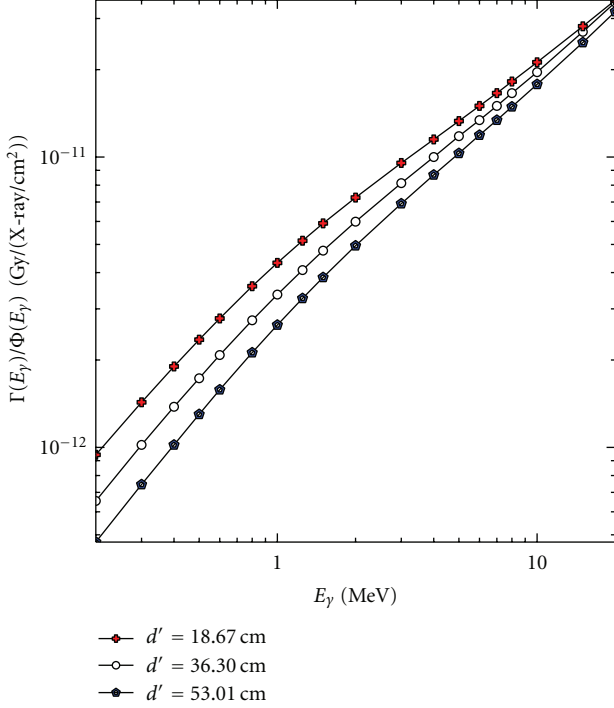


FIGURE 4: Fluence-to-mean-dose-in-water conversion factors  $\Gamma(E_y)/\Phi(E_y)$  used in calculating the energy response of CPID. The mean dose in water is defined as the integral of depth-dose curve along the depth axis normalized to the thickness of the water slab. The calculations assume broad parallel beam of X rays incident normally on 18.67, 36.30, and 53.01 cm thick slabs of water in air.

increase of the detector thickness, which is due to an increase of X-ray scatter in a thicker detector [5].

Figure 6 shows the values of  $f_{50}$  (i.e., the frequency at 50% of the MTF) as a function of the detector thickness for different beam qualities. The value of  $f_{50}$  at  $d = 10$  cm for a 6 MV clinical beam is  $\sim 0.24$  lp/mm, which is comparable to that of video-based EPIDs ( $f_{50} \sim 0.2$  lp/mm) [4]. A reduction of  $\sim 20\%$  of  $f_{50}$  was observed in our simulations when increasing the detector thickness to  $d = 30$  cm.

### 3.2. CPID Response

**3.2.1. Detection Efficiency.** Figure 7 shows the detection efficiencies of the CPID for various detector thicknesses as a function of incident X-ray energy. The efficiency for detecting X rays by means of the Cerenkov effect decreases rapidly with the decrease of X-ray energy below  $\sim 1$  MeV due to the threshold kinetic energy required to generate the Cerenkov light.

For clinically relevant X-ray spectra at 6, 10, and 18 MV (see entrance spectra in Figure 2), the detection efficiencies of CPID for various detector thicknesses are given in Table 2, which are more than an order of magnitude higher than that of current EPIDs.

**3.2.2. Detector Sensitivity.** The number of optical photons that are generated in the detector and reach the AMFPI per

TABLE 1: X-ray fluence-to-mean-dose conversion factors for monoenergetic broad parallel beams incident on 18.67, 36.30, and 53.01 cm thick water slabs in air in units of  $\text{Gy}/(\text{X-ray}/\text{cm}^2)$ . Statistical uncertainties for each X-ray energy are 1.2%, 1.3%, and 1.3% for the 18.67, 36.30, and 53.01 cm thick water slabs, respectively.

$E_y/\text{MeV}$	$d' = 18.67$ cm	$d' = 36.30$ cm	$d' = 53.01$ cm
0.2	$9.43 \times 10^{-13}$	$6.54 \times 10^{-13}$	$4.72 \times 10^{-13}$
0.3	$1.43 \times 10^{-12}$	$1.02 \times 10^{-12}$	$7.45 \times 10^{-13}$
0.4	$1.90 \times 10^{-12}$	$1.38 \times 10^{-12}$	$1.02 \times 10^{-12}$
0.5	$2.35 \times 10^{-12}$	$1.73 \times 10^{-12}$	$1.30 \times 10^{-12}$
0.6	$2.78 \times 10^{-12}$	$2.08 \times 10^{-12}$	$1.58 \times 10^{-12}$
0.8	$3.59 \times 10^{-12}$	$2.74 \times 10^{-12}$	$2.12 \times 10^{-12}$
1	$4.32 \times 10^{-12}$	$3.36 \times 10^{-12}$	$2.64 \times 10^{-12}$
1.25	$5.15 \times 10^{-12}$	$4.08 \times 10^{-12}$	$3.26 \times 10^{-12}$
1.5	$5.91 \times 10^{-12}$	$4.76 \times 10^{-12}$	$3.85 \times 10^{-12}$
2	$7.25 \times 10^{-12}$	$5.99 \times 10^{-12}$	$4.95 \times 10^{-12}$
3	$9.54 \times 10^{-12}$	$8.13 \times 10^{-12}$	$6.91 \times 10^{-12}$
4	$1.15 \times 10^{-11}$	$1.00 \times 10^{-11}$	$8.68 \times 10^{-12}$
5	$1.33 \times 10^{-11}$	$1.18 \times 10^{-11}$	$1.03 \times 10^{-11}$
6	$1.50 \times 10^{-11}$	$1.34 \times 10^{-11}$	$1.19 \times 10^{-11}$
7	$1.66 \times 10^{-11}$	$1.50 \times 10^{-11}$	$1.34 \times 10^{-11}$
8	$1.82 \times 10^{-11}$	$1.66 \times 10^{-11}$	$1.49 \times 10^{-11}$
10	$2.12 \times 10^{-11}$	$1.96 \times 10^{-11}$	$1.78 \times 10^{-11}$
15	$2.82 \times 10^{-11}$	$2.70 \times 10^{-11}$	$2.48 \times 10^{-11}$
20	$3.47 \times 10^{-11}$	$3.41 \times 10^{-11}$	$3.17 \times 10^{-11}$

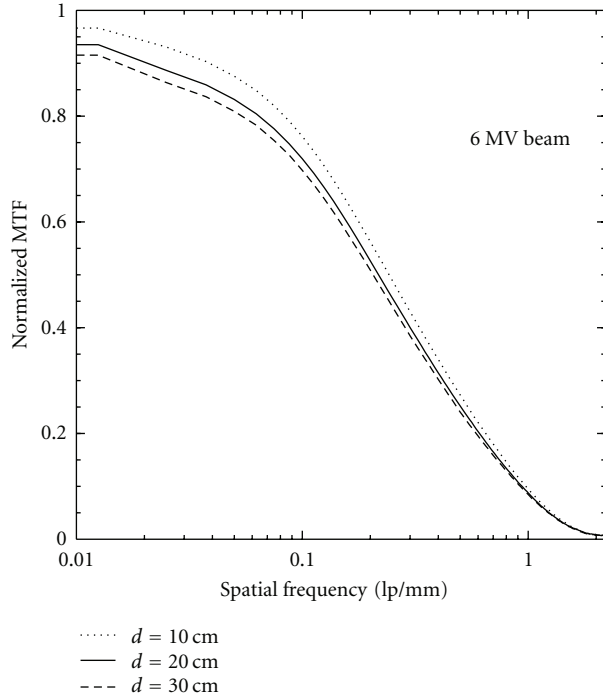
TABLE 2: Detection efficiencies of CPID for three clinical beams. Statistical uncertainty for each value is  $\sim 0.8\%$ .

$d/\text{cm}$	6 MV beam	10 MV beam	18 MV beam
10	39.4%	40.7%	40.2%
20	58.3%	62.0%	61.9%
30	67.1%	73.2%	73.8%

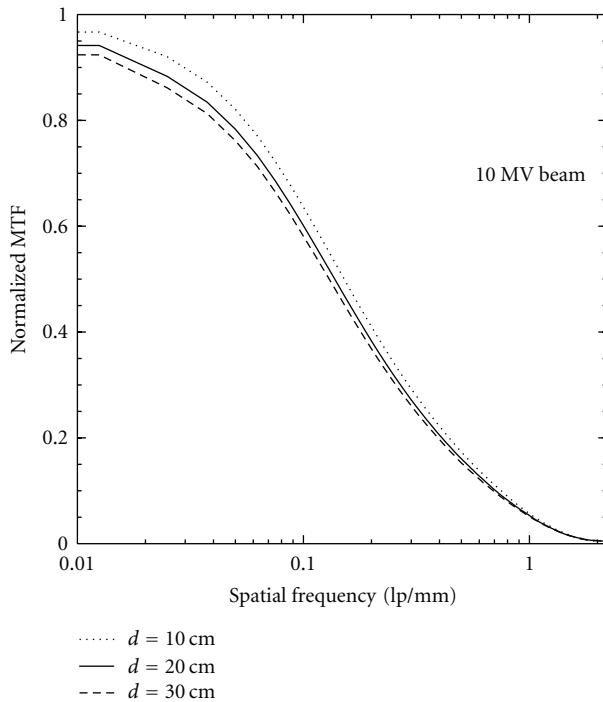
incident X-ray per pixel is shown in Figure 8 as a function of X-ray energy. It can be seen that the number of Cerenkov photons per incident X-ray increases monotonously with X-ray energy for all detector thicknesses.

The total number of the Cerenkov photons per pixel that are generated in the detector and reach the AMFPI per LINAC pulse ( $\sim 0.026$  cGy dose to water at the isocentre) [15] is given in Table 3 for various detector thicknesses. These were obtained using a fluence-to-dose conversion factor ( $8.4 \times 10^{-12}$   $\text{cm}^2\text{Gy}/\text{x-ray}$ ) at 6 MV. We note that the total electronic noise per pixel in AMFPIs is typically  $\sim 2 \times 10^3$  electrons [17].

**3.3. Beam Energy Hardening and Scatter due to the Presence of a Patient.** Lower energy photons are attenuated more when passing through a patient, and, as a result the mean energy of the X-ray spectrum exiting the patient increases. This can



(a)



(b)

FIGURE 5: The MTF as a function of spatial frequency for various thicknesses of the proposed CPID. The entrance spectra of X rays from Figure 2 were used in the simulation.

be seen in Figure 2 showing the entrance spectrum and the primary and scatter components of exit beam after traversing a 30 cm thick water phantom. The presence of a patient, in the beam also results in generation of secondary particles

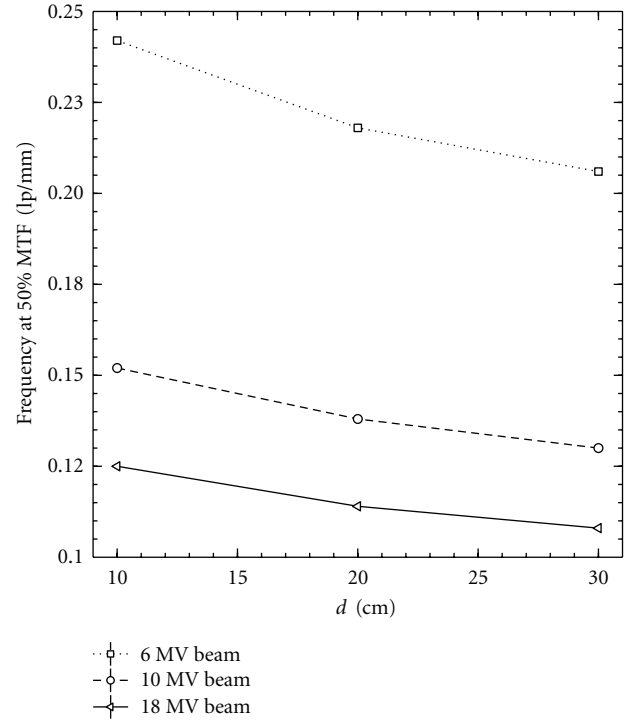


FIGURE 6: The frequency ( $f_{50}$ ) at 50% of the MTF as a function of detector thickness for different beam energies. The entrance spectra of X rays (see Figure 2) were used in the simulation.

TABLE 3: The total number of Cerenkov photons (that are generated in the detector and reach the AMFPI) per LINAC pulse ( $\sim 0.026$  cGy dose-to-water at the isocentre) for a 6 MV beam and various detector thicknesses. Statistical uncertainty for each value is  $\sim 0.8\%$ .

Energy (MV)	$d = 10$ cm	$d = 20$ cm	$d = 30$ cm
6	$1.56 \times 10^5$	$2.41 \times 10^5$	$2.82 \times 10^5$

TABLE 4: The signal scatter fractions of CPID for three clinical beams. Statistical uncertainty for each value is  $\sim 1.8\%$ .

Energy (MV)	$d = 10$ cm	$d = 20$ cm	$d = 30$ cm
6	0.19	0.17	0.17
10	0.18	0.16	0.15
18	0.17	0.15	0.14

that generally degrade image quality. Figures 9(a) and 9(b) represent the CPID response to the primary and scatter components of the exit beam, respectively, per X-ray incident on water phantom.

Figure 10 gives the signal scatter fraction ( $SF_{\text{signal}}$ , as defined in (5)) as a function of X ray energy. Except for very low energies ( $E_\gamma \leq 0.4$  MeV), where the error is  $>100\%$  due to low statistics, the value of  $SF_{\text{signal}}$  is  $\sim 15\text{--}20\%$  and decreases with increase of detector thicknesses.

The signal scatter fractions calculated for three clinical beams (see entrance spectra in Figure 2) incident on a 30 cm thick water phantom are given in Table 4.

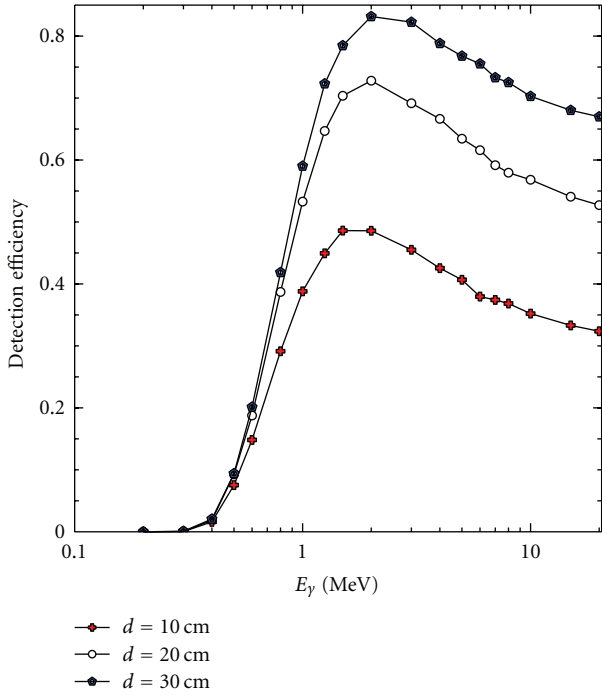


FIGURE 7: The detection efficiency of CPID as a function of incident X-ray energy for various thicknesses.

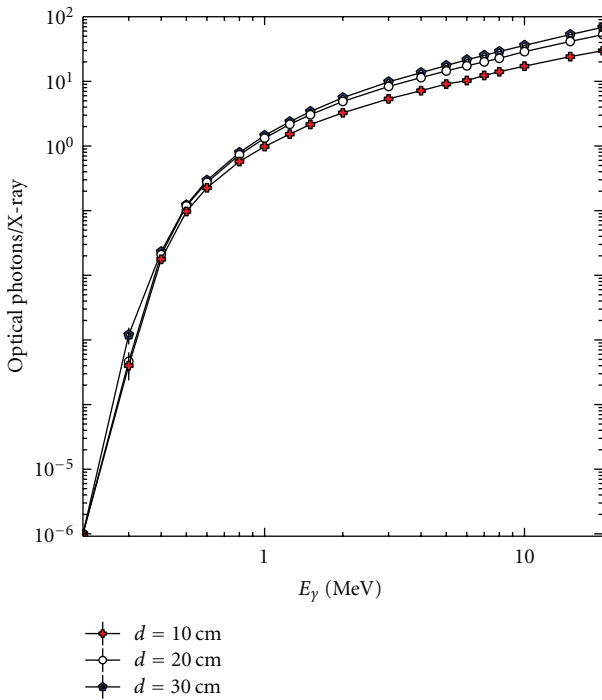
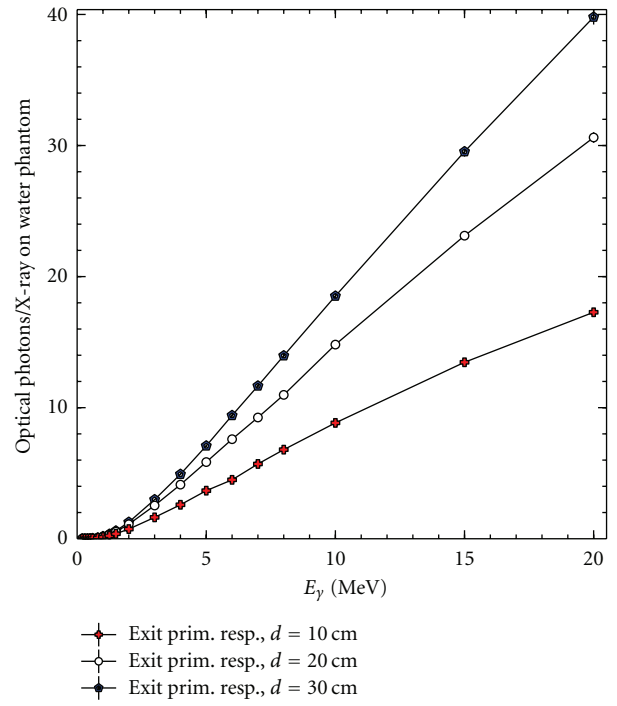
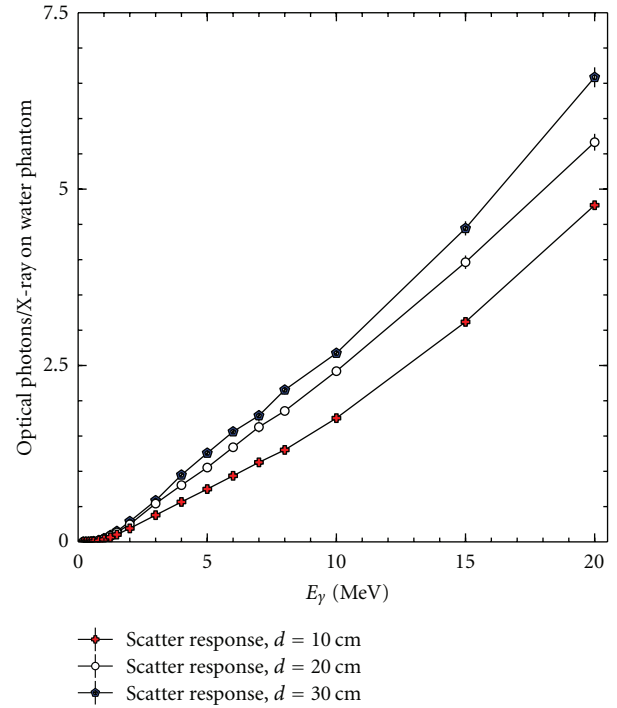


FIGURE 8: The number of Cerenkov photons (that are generated in the detector and reach the AMFPI) per incident X-ray as a function of incident X-ray energy.

Figure 11 shows the normalized spatial ( $x$ -direction only) distributions of the detector signal (i.e., distribution of optical photons reaching the AMFPI) for a 30 cm thick CPID



(a)



(b)

FIGURE 9: The number of Cerenkov photons (that are generated in the detector and reach the AMFPI) per X ray incident on the water phantom as a function of X-ray energy.

under irradiation of a 6 MV pencil beam with (open squares) and without (solid circles) the presence of the water slab (see Figure 3). The difference between these two curves is small.

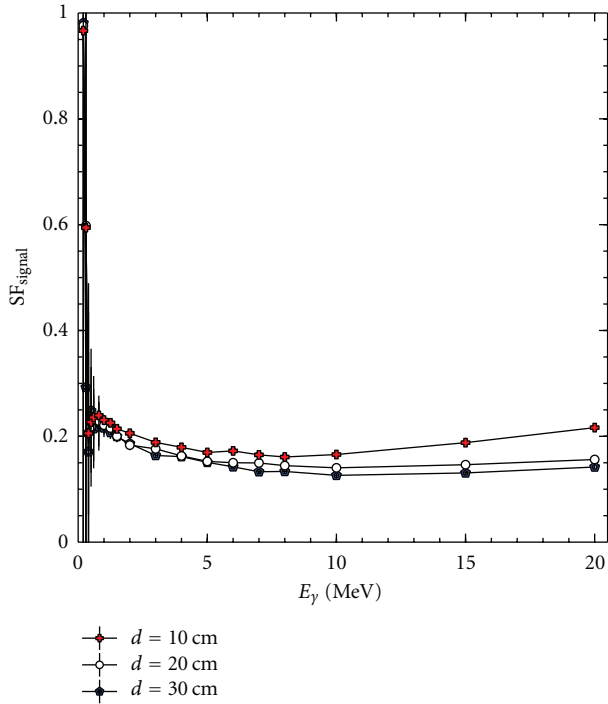


FIGURE 10: The signal scatter fraction for CPID response per pixel as a function of X-ray energy.

TABLE 5: The DQE at zero frequency of CPID for three clinical beams. Statistical uncertainties for each value is  $\sim 0.8\%$ .

$d/\text{cm}$	6 MV beam	10 MV beam	18 MV beam
10	20.8%	22.9%	23.2%
20	31.5%	36.0%	37.0%
30	37.1%	43.5%	45.3%

**3.4. Detective Quantum Efficiency.** The zero spatial frequency DQE was calculated from the results of the simulation output using (6) and (7). Figure 12 shows the  $\text{DQE}(0)$  as a function of incident beam energy for detector thicknesses of 10, 20, and 30 cm. The  $\text{DQE}(0)$  follows the general trend of detection efficiency  $\eta$  (see Figure 7). However,  $\text{DQE}(0)$  varies slowly above  $\sim 2$  MeV (compared to detection efficiency). Sufficient number of events has been simulated to provide for a statistical uncertainty at a percent level ( $\sim 0.8\%$ ).

Table 5 lists DQE at the zero spatial frequency simulated for three clinical beams (see entrance spectra in Figure 2). As expected the  $\text{DQE}(0)$  of the proposed CPID is more than an order higher than that of current EPIDs [4].

Finally, the spatial frequency dependent detective quantum efficiencies  $\text{DQE}(f)$  are shown in Figure 13 for 6 and 10 MV beams at different detector thicknesses.

**3.5. Energy Dependence of CPID Dose Response.** Figure 14 shows the relative response of the detector per unit dose to water as a function of X-ray energy. It can be seen that the

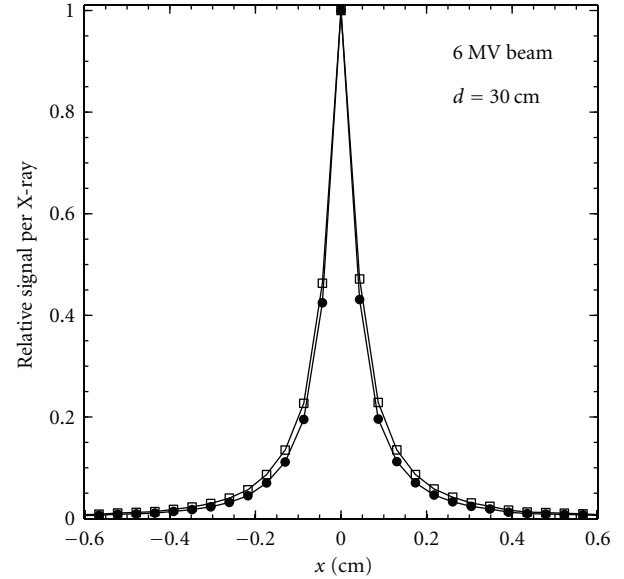


FIGURE 11: Renormalized spatial distributions of the detector signal for a 30 cm thick CPID under irradiation of a 6 MV pencil beam with (open squares) and without (solid circles) the presence of the water slab.

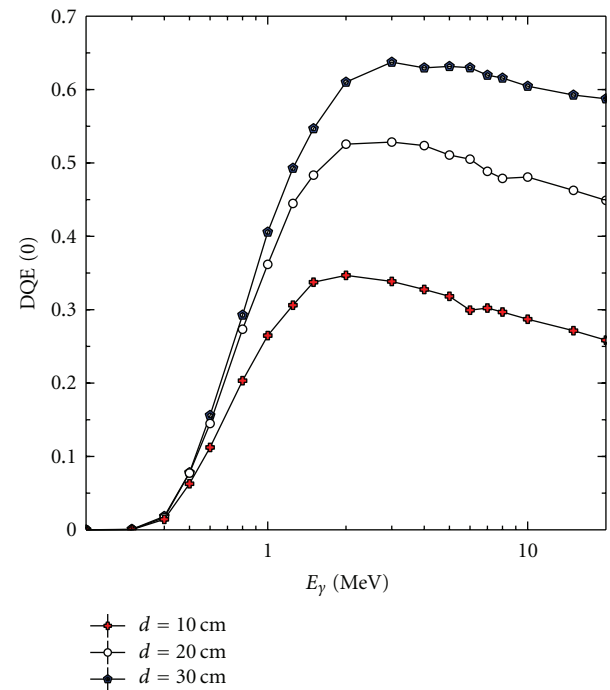


FIGURE 12: The DQE at zero spatial frequency as a function of beam energy for different detector thicknesses.

proposed CPID has lower response to low-energy X rays due to the threshold energy required for generating Cerenkov light. The shape of the energy dependence curve has little dependence on the detector thickness.

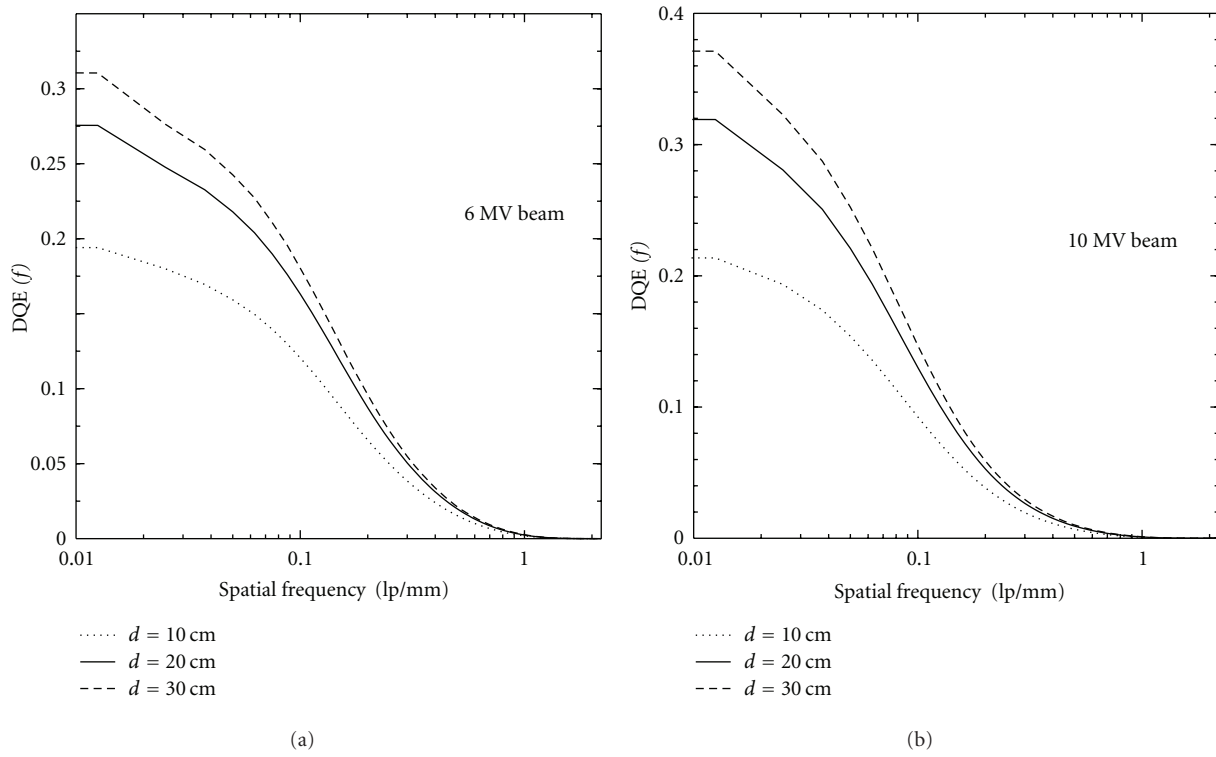


FIGURE 13: The DQE as a function of spatial frequency, obtained from (8), for different detector thicknesses and X-ray spectra.

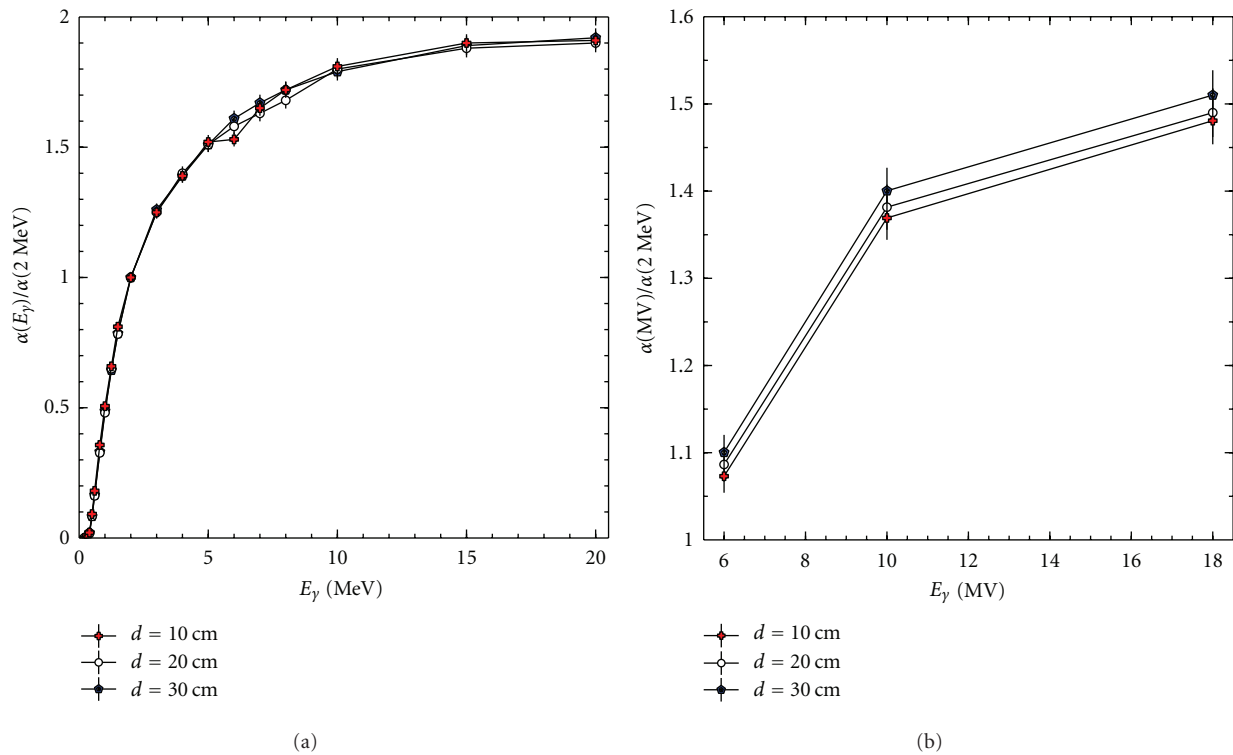


FIGURE 14: Energy dependence curves for the CPID without water phantom. The  $\alpha(E_\gamma)/\alpha(2 \text{ MeV})$  curve for monoenergetic beams is shown on the left and  $\alpha(\text{MV})/\alpha(2 \text{ MeV})$  curve for polyenergetic beams is shown on the right.

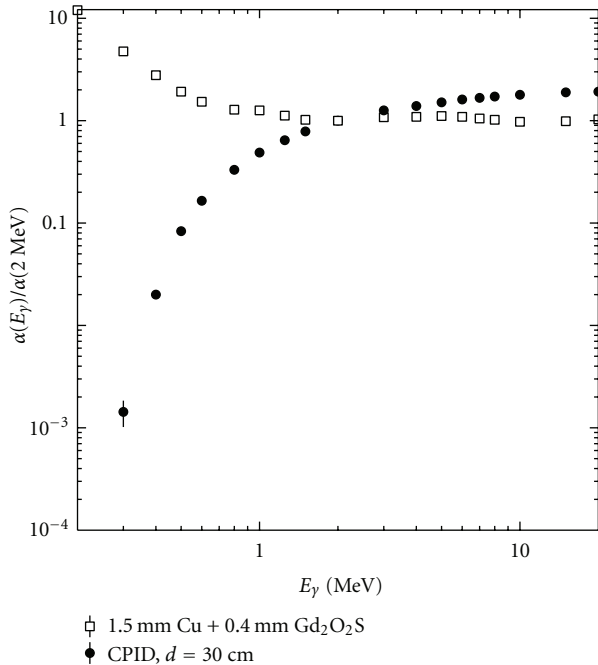


FIGURE 15: Energy dependence of the dose response (for a given dose to water) of a 30 cm thick CPID (solid circles) and that of a conventional Cu plate/phosphor screen system (open squares).

#### 4. Discussion

The main advantage of the proposed CPID is that it can have much higher detection efficiency than current EPIDs. At 6 MV the DQE(0) of CPID can be as high as 37.1%, as compared to  $\sim 1\%$  for most current EPIDs. In addition, the energy response of the CPID is also unique. Figure 15 shows the comparison between the CPID (with  $d = 30$  cm) and a conventional Cu plate/phosphor screen detector consisting of a  $\sim 134 \text{ mg/cm}^2$   $\text{Gd}_2\text{O}_2\text{S}$  phosphor loading (Kodak Lanex fast back) on a 1.5 mm thick copper plate. The energy dependence curve for the Cu plate/phosphor screen was obtained for a given reference dose (to water) from the results of Cremers et al. [22]. In the case of Cu plate/phosphor screen, the reference dose to water is defined as the average dose to a 3 mm thick layer of water at a depth of 3.3 cm in a water phantom with 157 cm SSD [28]. In contrast to the conventional Cu plate/phosphor screen that overresponds to low-energy X rays, the CPID underresponds to X rays below 1 MeV. Since scattered X rays from patients have lower energies than the primary ones and the presence of scattered X rays usually degrade image quality, the underresponse to low energy X rays by the CPID could be advantageous for MV X-ray imaging where no practical antiscatter grid is available. As shown in Table 4, the signal scatter fraction of CPID at 6 MV is 17–19%, which is lower than that ( $\sim 35\%$ ) of a Cu plate/phosphor screen obtained from [24] for the same air gap, X-ray beam energy, and thickness of the scattering material. Thus, the CPID is an antiscatter detector for MV X-ray imaging.

However, there are some disadvantages associated with the proposed detector. The proposed detector could be bulky

and much heavier than current flat-panel-based EPIDs, depending on the thickness chosen. While counterbalancing the large weight of the CPID may require reengineering of the LINAC gantry, the weight issue is common to all high detection efficiency detectors since a large mass of the energy conversion layer is necessary to achieve high detection efficiency. The investigated detector configurations are not expected to be bulkier than a video-based EPID and, thus, would be useable in clinic. In addition, the spatial resolution of the proposed detector would be worse than that of current flat-panel-based EPIDs. This is mainly because (1) more X rays are scattered in our thick detector as compared to that in current flat-panel-based EPIDs [5], and (2) the range of energetic electrons generated by incident X rays in our detector is larger due to the lower density materials used in the CPID. In silica the electron range is approximately 6.8 mm for 6 MV beam and 17 mm for 18 MV beam (based on the value of  $d_{\text{max}}$  in water [1] scaled by the density of the silica). However, for megavoltage X rays, most energetic electrons generated in the detector are initially moving in the forward direction, that is, in the direction of the incident X rays. In addition, as an energetic electron travels in the detector, it continuously loses its kinetic energy. Once its kinetic energy is below the threshold energy required for Cerenkov radiation, the electron can no longer generate Cerenkov light, and; thus, any further spatial spread of low energy electrons has no effect on the resolution of the CPID. As a result, the resolution of the proposed detector is comparable to that of video-based EPIDs.

#### 5. Conclusions

A Monte Carlo simulation has been conducted to investigate imaging and dosimetric characteristics of a novel design of a megavoltage (MV) X-ray detector for radiotherapy applications. It has been shown that the new design can have a zero-frequency detective quantum efficiency more than an order of magnitude higher than that of current clinical systems and yet a spatial resolution comparable to that of previously developed video-based electronic portal imaging devices. In addition, the proposed detector uses Cerenkov effect to detect MV X rays, and, as a result, it is less sensitive to low-energy X rays (including scattered X rays from patients) than current electronic portal imaging devices.

#### Acknowledgments

This work was supported by the Natural Sciences and Engineering Research Council of Canada (NSERC) and the Canadian Institutes of Health Research (CIHR). The authors also thank Dr. G. Gavalian for providing CPU time on 8 computing cores at Department of Physics, Old Dominion University, VA, USA.

#### References

- [1] F. M. Khan, *The Physics of Radiation Therapy*, Williams & Wilkins, Baltimore, Md, USA, 2nd edition, 1994.

- [2] E. J. Seppi, P. Munro, S. W. Johnsen et al., "Megavoltage cone-beam computed tomography using a high-efficiency image receptor," *International Journal of Radiation Oncology Biology Physics*, vol. 55, no. 3, pp. 793–803, 2003.
- [3] J. Pouliot, A. Bani-Hashemi, J. Chen et al., "Low-dose megavoltage cone-beam CT for radiation therapy," *International Journal of Radiation Oncology Biology Physics*, vol. 61, no. 2, pp. 552–560, 2005.
- [4] L. E. Antonuk, "Electronic portal imaging devices: a review and historical perspective of contemporary technologies and research," *Physics in Medicine and Biology*, vol. 47, no. 6, pp. R31–R65, 2002.
- [5] G. Pang and J. A. Rowlands, "Development of high quantum efficiency flat panel detectors for portal imaging: Intrinsic spatial resolution," *Medical Physics*, vol. 29, no. 10, pp. 2274–2285, 2002.
- [6] M. A. Mosleh-Shirazi, P. M. Evans, W. Swindell, J. R. N. Symonds-Taylor, S. Webb, and M. Partridge, "Rapid portal imaging with a high-efficiency, large field-of-view detector," *Medical Physics*, vol. 25, no. 12, pp. 2333–2346, 1998.
- [7] J. Ostling, M. Wallmark, A. Brahme et al., "Novel detector for portal imaging in radiation therapy," in *Medical Imaging 2000: Physics of Medical Imaging*, vol. 3977 of *Proceedings of SPIE*, pp. 84–95, February 2000.
- [8] R. Hinderer, J. M. Kapatoes, H. Keller et al., "Development of a new multielement detector system for megavoltage photons," in *Medical Imaging 2002: Physics of Medical Imaging*, vol. 4682 of *Proceedings of SPIE*, pp. 809–818, February 2002.
- [9] A. Sawant, L. E. Antonuk, Y. El-Mohri et al., "Segmented crystalline scintillators: an initial investigation of high quantum efficiency detectors for megavoltage x-ray imaging," *Medical Physics*, vol. 32, no. 10, pp. 3067–3083, 2005.
- [10] T. T. Monajemi, B. G. Fallone, and S. Rathee, "Thick, segmented CdWO<sub>4</sub>-photodiode detector for cone beam megavoltage CT: a Monte Carlo study of system design parameters," *Medical Physics*, vol. 33, no. 12, pp. 4567–4577, 2006.
- [11] Y. El-Mohri, L. E. Antonuk, Q. Zhao et al., "Low-dose megavoltage cone-beam CT imaging using thick, segmented scintillators," *Physics in Medicine and Biology*, vol. 56, pp. 1509–1527, 2011.
- [12] G. Pang and J. A. Rowlands, "Development of high quantum efficiency, flat panel, thick detectors for megavoltage x-ray imaging: a novel direct-conversion design and its feasibility," *Medical Physics*, vol. 31, no. 11, pp. 3004–3016, 2004.
- [13] S. Wang, J. K. Gardner, J. J. Gordon et al., "Monte Carlo-based adaptive EPID dose kernel accounting for different field size responses of imagers," *Medical Physics*, vol. 36, no. 8, pp. 3582–3595, 2009.
- [14] D. A. Jaffray, J. J. Battista, A. Fenster, and P. Munro, "Monte Carlo studies of x-ray energy absorption and quantum noise in megavoltage transmission radiography," *Medical Physics*, vol. 22, no. 7, pp. 1077–1088, 1995.
- [15] X. Mei, J. A. Rowlands, and G. Pang, "Electronic portal imaging based on Cerenkov radiation: a new approach and its feasibility," *Medical Physics*, vol. 33, no. 11, pp. 4258–4270, 2006.
- [16] J. V. Jelley, *Cerenkov Radiation and Its Applications*, Pergamon Press, London, UK, 1958.
- [17] J. A. Rowlands and J. Yorkston, "Flat Panel Detectors for Digital Radiography," in *Handbook of Medical Imaging*, L. V. M. Richard, B. Jacob, and L. K. Harold, Eds., pp. 223–328, SPIE Press, 2000.
- [18] J. M. Boudry and L. E. Antonuk, "Radiation damage of amorphous silicon, thin-film, field-effect transistors," *Medical Physics*, vol. 23, no. 5, pp. 743–754, 1996.
- [19] K. Tanioka, J. Yamazaki, K. Shidara et al., "Avalanche-mode amorphous selenium photoconductive target for camera tube," in *Advances in Electronics and Electron Physics*, B. L. Morgan, Ed., vol. 74, pp. 379–387, Academic Press, 1988.
- [20] S. Agostinelli, J. Allison, K. Amako et al., "GEANT4—a simulation toolkit," *Nuclear Instruments and Methods in Physics Research A*, vol. 506, no. 3, pp. 250–303, 2003.
- [21] J. T. Dobbins, "Effects of undersampling on the proper interpretation of modulation transfer function, noise power spectra, and noise equivalent quanta of digital imaging systems," *Medical Physics*, vol. 22, no. 2, pp. 171–182, 1995.
- [22] F. Cremers, T. Frenzel, C. Kausch, D. Albers, T. Schönborn, and R. Schmidt, "Performance of electronic portal imaging devices (EPIDs) used in radiotherapy: image quality and dose measurements," *Medical Physics*, vol. 31, no. 5, pp. 985–996, 2004.
- [23] H. Fujita, D. Y. Tsai, T. Itoh et al., "A simple method for determining the modulation transfer function in digital radiography," *IEEE Transactions on Medical Imaging*, vol. 11, no. 1, pp. 34–39, 1992.
- [24] D. A. Jaffray, J. J. Battista, A. Fenster, and P. Munro, "X-ray scatter in megavoltage transmission radiography: Physical characteristics and influence on image quality," *Medical Physics*, vol. 21, no. 1, pp. 45–60, 1994.
- [25] R. K. Swank, "Absorption and noise in x-ray phosphors," *Journal of Applied Physics*, vol. 44, no. 9, pp. 4199–4203, 1973.
- [26] C. E. Dick and J. W. Motz, "Image information transfer properties of x-ray fluorescent screens," *Medical Physics*, vol. 8, no. 3, pp. 337–346, 1981.
- [27] M. Lachaine and B. G. Fallone, "Monte Carlo detective quantum efficiency and scatter studies of a metal/a-Se portal detector," *Medical Physics*, vol. 25, no. 7, pp. 1186–1194, 1998.
- [28] B. M. C. McCurdy, K. Luchka, and S. Pistorius, "Dosimetric investigation and portal dose image prediction using an amorphous silicon electronic portal imaging device," *Medical Physics*, vol. 28, no. 6, pp. 911–924, 2001.

## Research Article

# Development of Automatic 3D Blood Vessel Search and Automatic Blood Sampling System by Using Hybrid Stereo-Autofocus Method

Eiji Nakamachi, Yusuke Morita, and Yoshifumi Mizuno

*Department of Biomedical Engineering, Doshisha University, 1-3 Miyakodani, Tatara, Kyotanabe, Kyoto 610-0394, Japan*

Correspondence should be addressed to Eiji Nakamachi, enakamac@mail.doshisha.ac.jp

Received 11 July 2011; Accepted 21 September 2011

Academic Editor: Nanguang Chen

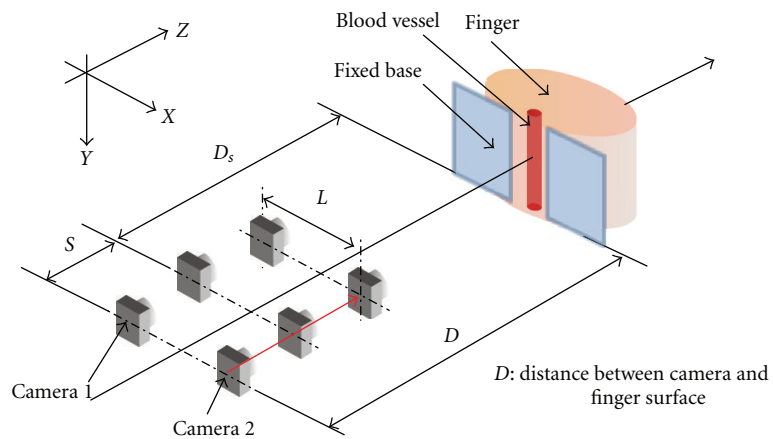
Copyright © 2012 Eiji Nakamachi et al. This is an open access article distributed under the Creative Commons Attribution License, which permits unrestricted use, distribution, and reproduction in any medium, provided the original work is properly cited.

We developed an accurate three-dimensional blood vessel search (3D BVS) system and an automatic blood sampling system. They were implemented into a point-of-care system designed for medical care, installed in a portable self-monitoring blood glucose (SMBG) device. The system solves problems of human error caused by complicated manual operations of conventional SMBG devices. We evaluated its accuracy of blood-vessel position detection. The 3D BVS system uses near-infrared (NIR) light imaging and the stereo and autofocus hybrid method to determine blood vessel locations accurately in three dimensions. We evaluated the accuracy of our 3D BVS system using a phantom of human skin, blood vessels, and blood. Additionally, we established an automatic blood sampling system for SMBG and assessed its performance in relation to punctures, blood suction, transport, and discharge on an enzyme sensor. The 3D BVS and automatic blood sampling system are adequate for use in a portable SMBG device.

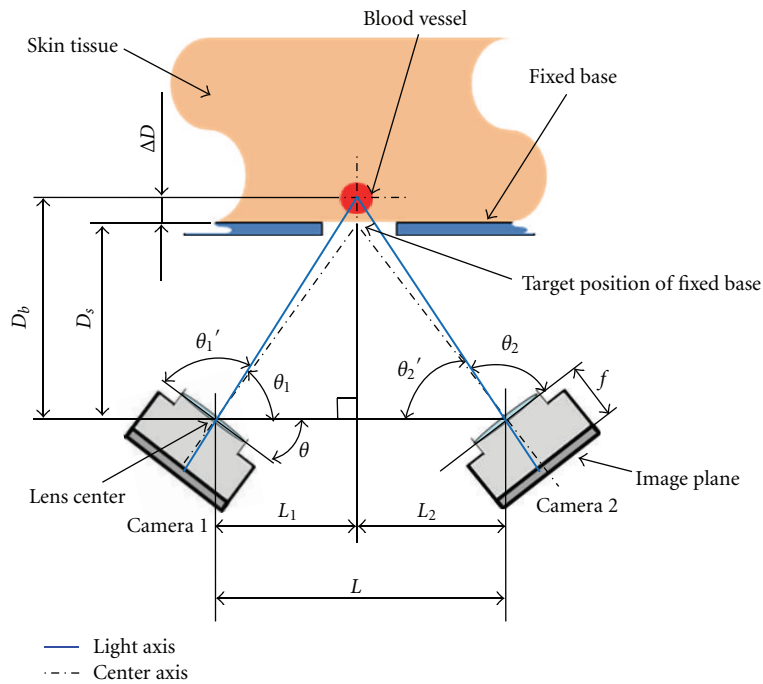
## 1. Introduction

Recently, the rapidly increasing number of diabetic patients has [1] become a major social problem throughout the world. Diabetic patients must independently measure blood glucose concentrations using a self-monitoring blood glucose (SMBG) device and self-inject insulin several times each day [2, 3]. Diabetes patients and candidates might constitute up to one-fifth of the world population [1]. Therefore, SMBG devices are expected to play an increasingly important role in daily medical care. The commercial SMBG devices of various kinds that are on the market today can be categorized as either noninvasive or minimally invasive. Noninvasive devices adopt infrared spectroscopy [4], FT-IR-ATR method [5], photoacoustic spectroscopy [6], and so on. However, these methods present severe problems of low accuracy and unreliability. In contrast, minimally invasive devices [7, 8] can measure blood glucose concentrations with high accuracy [9], but puncture with a needle or knife edge is painful. In addition, such devices frequently induce human error because of their complicated

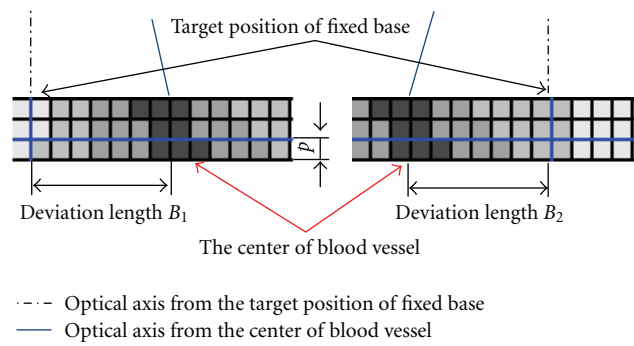
manual operations during puncture, treatment of small blood samples, self-measurement, and so on. Therefore, many improvements are necessary for SMBG devices. Several groups have developed minimally invasive SMBG devices equipped with a blood vessel search system to reduce human error. For example, Yamakoshi et al. developed a device to detect the positions of blood vessels in the arm using reflected near-infrared (NIR) light [10], but the blood vessel depth could not be determined accurately. Another example is a bio-medical-chip developed by Horiike et al., which can detect the position of a blood vessel in three dimensions using electric signals [11]. However, their chip showed low accuracy of blood vessel location detection, and the device entailed operations that were time-consuming and painful for patients. Although Kandani et al. developed a three-dimensional blood vessel search (3D BVS) system using the stereo method [12], the value of the standard deviation of measured positions was higher for deeper blood vessel locations. In this study, we set our goal as integration of a 3D BVS system and an automatic blood sampling system. To accomplish that goal, we combined the autofocus method



(a) Schematic diagram of movement of the cameras in our system



(b) Schematic view of the stereo optical system embedded in a 3D BVS system



(c) 8 bit Pixel images of CMOS camera 1 and 2 (three rows) and deviation lengths  $B_1$  and  $B_2$

FIGURE 1: Schematic diagram of the autofocus and stereo hybrid methods embedded in a 3D BVS system.

with the original stereo method to establish a hybrid method. We set the allowed value of  $100\ \mu\text{m}$  for the targeted blood vessel, which had diameter of  $500\text{--}1000\ \mu\text{m}$ . An automatic blood sampling system for collection and transport of the blood for blood glucose measurements was connected with 3D BVS to produce the portable medical care system. For patients with diabetes, this system is expected to improve quality of life to a considerable degree.

As described in this paper, we first discuss the hybrid stereo-autofocus method for 3D BVS systems by introducing images processed with NIR light. Then we examine the accuracy of the 3D BVS system. Secondly, to evaluate our newly developed automatic blood sampling system for blood glucose measurement, we verify its capabilities of (1) accurate puncture, (2) stable blood transport, and (3) blood discharge on a glucose enzyme sensor. In light of those results, we assess the performance of this integrated portable medical care system.

## 2. Hybrid Stereo-Autofocus Method and Blood Vessel Visualization

**2.1. Autofocus Method and Stereo Method.** We used a hybrid stereo-autofocus method to detect the position of a blood vessel located between the first and second joints of the finger using transmitting NIR light. Our previous studies, which were done using a stereo method, did not determine the blood vessel depths accurately [12]. The measurement error was high for blood vessels located deep in the finger. Therefore, we adopted an autofocus method to obtain a very clear image of blood vessels using the template search method in the region of blood vessel [13]. This method improved the accuracy considerably. As presented in Figure 1(a), we took blood vessel images using different camera positions in relation to the finger based on the autofocus method.  $D$  means the length between the initial set position and the fixed base, and  $S$  the slide length as indicated in Figure 1(a). Fixed base means the upper surface of the glass plate, which is located at the position  $D_s$  and on which the finger was set. We evaluated the blood vessel image sharpness based on the template-matching algorithm and selected the clearest image at the camera position  $D_s$  as shown in Figure 1(a) [13]. In the auto focus procedure, we fix the incline angle  $\theta$  as indicated in Figure 1(b).

Next, as shown in Figure 1(b), we measured blood vessel positions using the stereo method [12]. In Figure 1(b),  $L$  stands for the distance between the two CMOS cameras,  $f$  represents the focal length,  $D_b$  signifies the vertical distance between the center of the blood vessel and the line drawn between two center points of the lenses, and  $D_s$  denotes the vertical distance between the reference surface of the fixed base and the line drawn between respective center points of the lenses. In Figure 1(b),  $\Delta D$  is the depth of the blood vessel center from the reference surface of fixed base. Figure 1(b) shows  $\theta_1$  and  $\theta_2$  as the angles of the light axes from the center of the blood vessel against the horizontal line between the respective centers of the two lenses. As shown in Figure 1(c), the center of the blood vessel can be detected

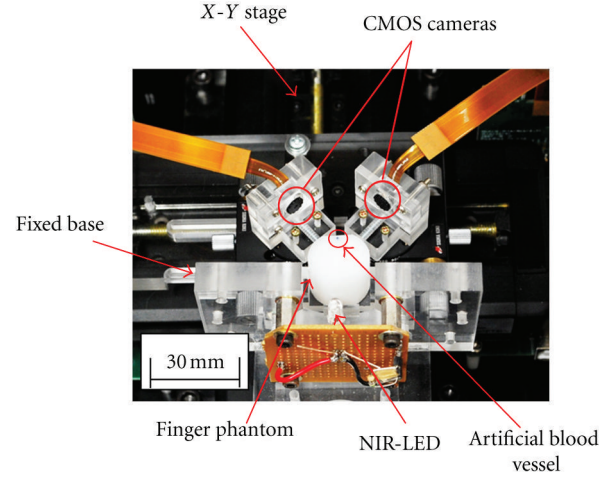


FIGURE 2: Photograph of the 3D BVS system.

from the luminance distribution of the blood vessel images obtained using the two CMOS cameras. Furthermore,  $\theta_1$  and  $\theta_2$  are calculable using trigonometric functions. The size of image plane pixel,  $5.55\ \mu\text{m}$ , was used to evaluate the blood vessel center position with the same length ratio as the pixel. Therefore, we obtain the deviation lengths  $B_1$  and  $B_2$  as indicated in Figure 1(c), which can be calculated as a number of deviated pixels times by pixel size  $5.55\ \mu\text{m}$ . Finally,  $D_b$  is expressed as

$$D_b = \frac{\tan \theta_1 \cdot \tan \theta_2}{\tan \theta_1 + \tan \theta_2} L, \quad (1)$$

here,  $\theta_1 = \pi - \theta - \theta'_1$ ,  $\theta_2 = \pi - \theta - \theta'_2$ ,  $\theta'_1 = \tan^{-1}(f/B_1)$ ,  $\theta'_2 = \tan^{-1}(f/B_2)$ ,  $L = L_1 + L_2 = (D_b/\tan \theta_1) + (D_b/\tan \theta_2)$ .

Length  $D_s$  is already determined by using the autofocus method as shown in Figure 1(a). Therefore, the blood vessel depth ( $\Delta D$ ) can be calculated as

$$\Delta D = D_b - D_s. \quad (2)$$

**2.2. 3D BVS System and Blood Vessel Visualization.** We incorporated the hybrid stereo-autofocus components into a 3D BVS system, which included four NIR LED lights (peak wavelength of 870 nm, KED871M51A; Kyosemi Corp.) as the light sources, two CMOS cameras (PPV404C; Asahi Denshi Inc.), and two image-processing units (PP-DEB-007; Asahi Electronics Laboratory Co., Ltd.). The NIR LEDs were set behind the finger to irradiate the finger with NIR light. We used two CMOS cameras to take images using the NIR transmitted light. Details of the CMOS cameras were the following: 5.32 mm focal length,  $8 \times 8 \times 5.55\ \text{mm}$  size, and  $5.55 \times 5.55\ \mu\text{m}$  pixel size. Images were of 8-bit digital gray-scale values ranging from black (0) to white (255) for one pixel. The  $640 \times 480$  pixel images were stored as JPEG image files. The images were processed by an image processing unit (AT401; Asahi Denshi Inc.) to calculate the blood vessel depth using the autofocus and stereo algorithms. Figure 2 presents a photograph of our 3D BVS system. The respective centers of CMOS cameras and LEDs are set on the same

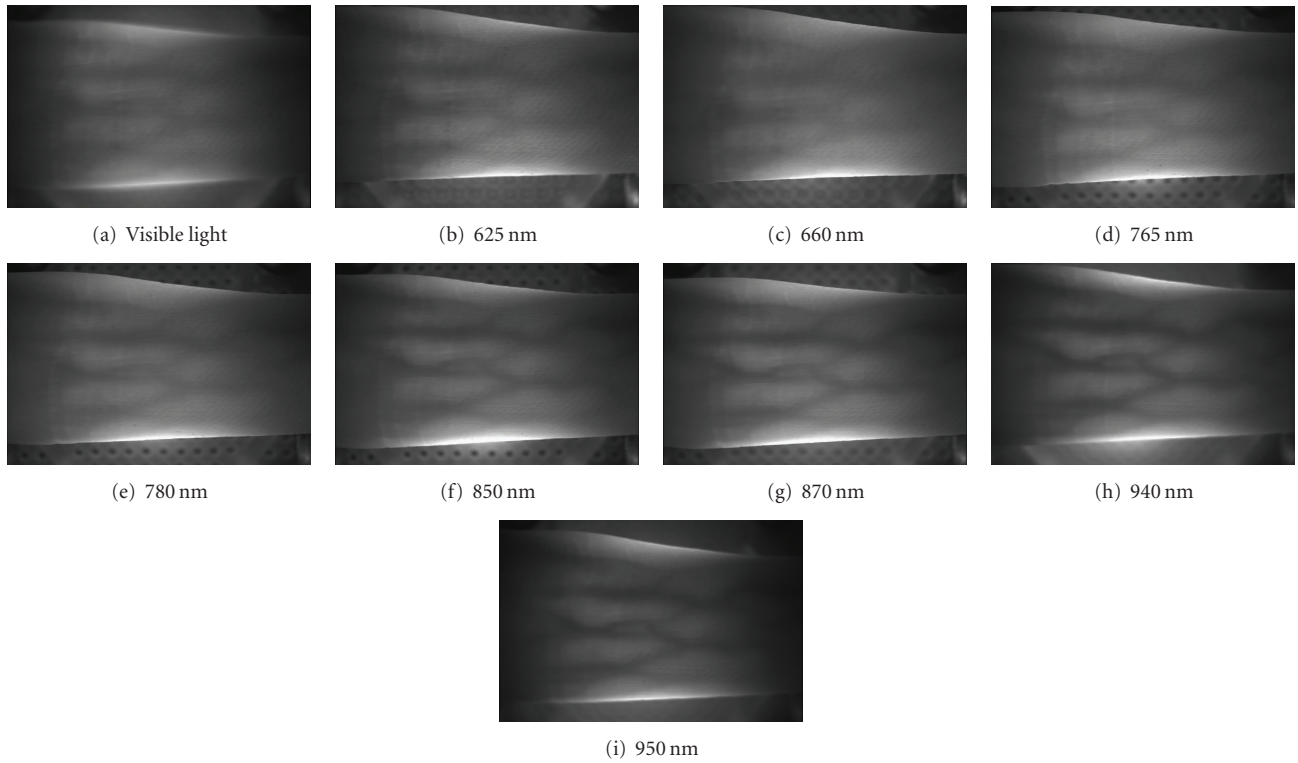


FIGURE 3: Blood vessel photos in cases of NIR lights, wavelengths 625–950 nm, and visible light.

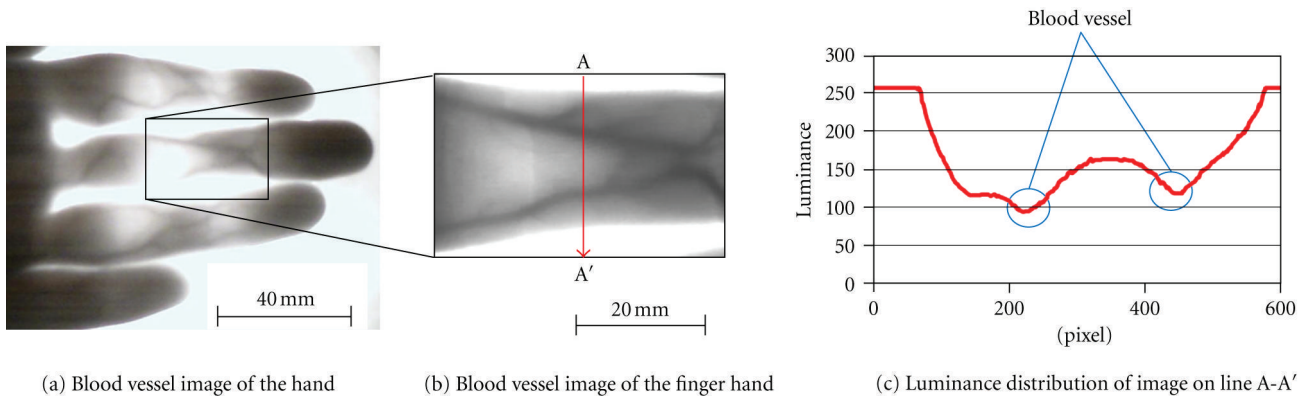


FIGURE 4: Image of the blood vessel in the human finger. The NIR light wavelength is 870 nm.

horizontal plane. The length between the cameras ( $L$  value: Figure 1(b)) was set to 30 mm. The length between the object and the camera lens ( $D_s$  value: Figure 1) was set to 18.8 mm. The CMOS cameras were inclined at 33.5 deg using a rotating stage (KSP-256; Sigma Koki Co., Ltd.). The size of our 3D BVS device became  $40 \times 30 \times 10$  mm. Therefore, our system had size and features that allowed its installation into our new portable SMBG device. We used the transmitted NIR light to visualize blood vessels located in the human finger [14–16]. We selected small veins as our measurement targets and employed NIR light with wavelengths of 650–950 nm. The NIR light was transmitted through the finger and was recorded in images by the cameras in the positions presented in Figures 1(b) and 2. Figure 3 shows images obtained using

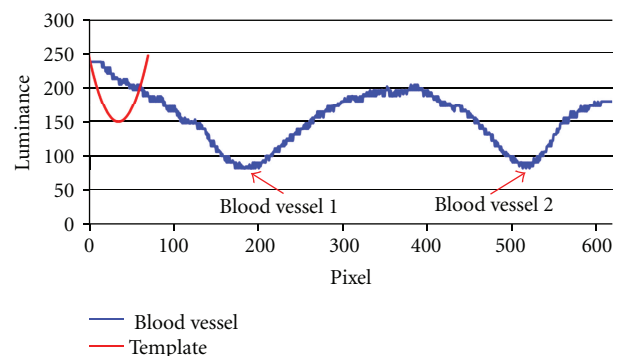


FIGURE 5: Luminance distribution of the image including the blood vessel and the template to search the blood vessels.

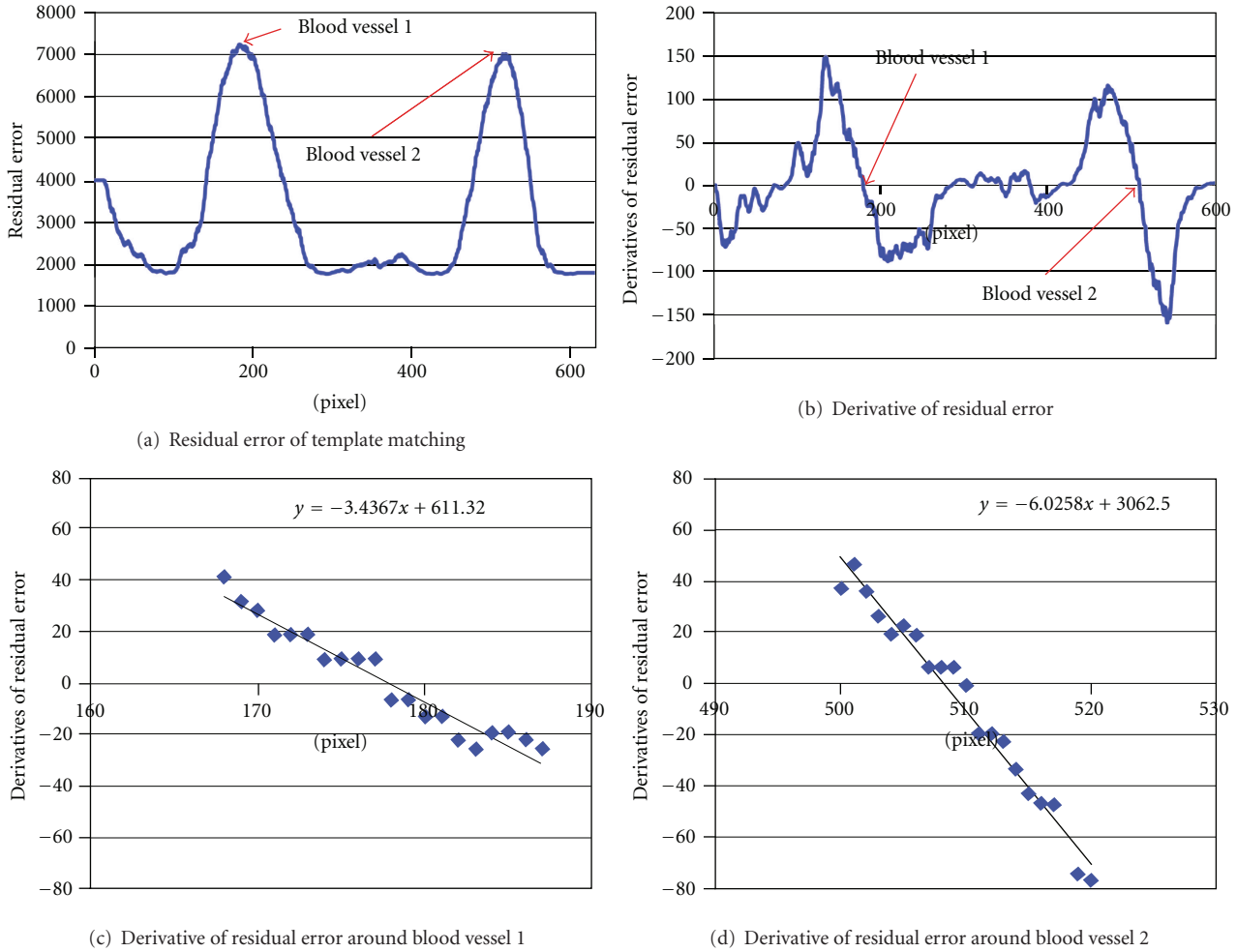


FIGURE 6: Residual errors calculated by template matching algorithm and its derivatives distributions to determine the sharpness.

the visible light and NIR light of the wavelengths shown in the figures. According to the steepest gradient search of the luminance distribution, especially in the close area to the blood vessel, finally we chose the wavelength of 870 nm [11, 13]. Figure 4 presents blood vessel images and the luminance distribution along line A–A' as indicated in Figure 4(b). We concluded that our imaging system can provide a clearer image of the blood vessel to determine its location in three dimensions.

Next we discuss the image processing associated with blood vessel detection. We adopted template matching to determine the image sharpness. The templates were produced on the assumption that the luminance distributions of blood vessels are convex-downward quadratic curves, as shown by the red curve in Figure 5, where the luminance distribution is portrayed as a blue line. Figures 6(a)–6(d) show results of template matching. Figure 6(a) presents the distribution of residual error obtained by template matching calculation. It shows two local maximum points, which correspond to the blood vessel position. Figure 6(b) portrays the distribution of the derivative of residual error. Figures 6(c) and 6(d) show the point at which the derivative value becomes zero, which

is the center of the blood vessel. Moreover, we assumed the inclination of the diagram of derivative values to be the rate of luminance change. Therefore, we confirmed that the blood vessel can be detected clearly as the rate of luminance change. The sharpness can be evaluated using the angle of inclination of derivatives, as shown in Figures 6(c) and 6(d). Results show that we can select a clear image of a blood vessel taken by the camera located at distance  $D_s$  shown in Figure 1(a).

### 3. Evaluation of Blood Vessel Position Detection

We evaluated the accuracy of our 3D BVS system by carrying out experiments using finger phantoms containing artificial blood vessels. The photograph and the finger phantom size are depicted in Figure 7. Small veins of a human finger, with diameters of 0.5–1.0 mm, exist at depths of 0.5–2.0 mm from the surface. Therefore, we used the diameter of 0.75 mm for artificial blood vessels. We generated finger phantoms of seven types with artificial blood vessels embedded at different depths of 0.5–2.0 mm with 0.25 mm intervals. The finger phantoms were made of the polyacetal resin (TPS-POM; Toyo Plastic Seiko Co., Ltd.), which had optical

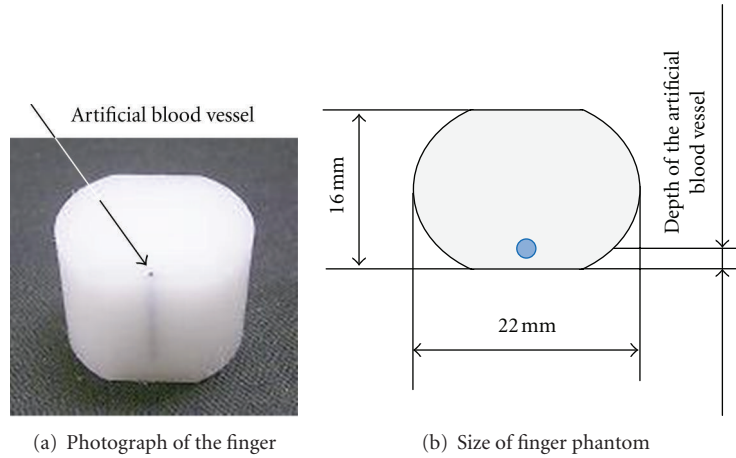
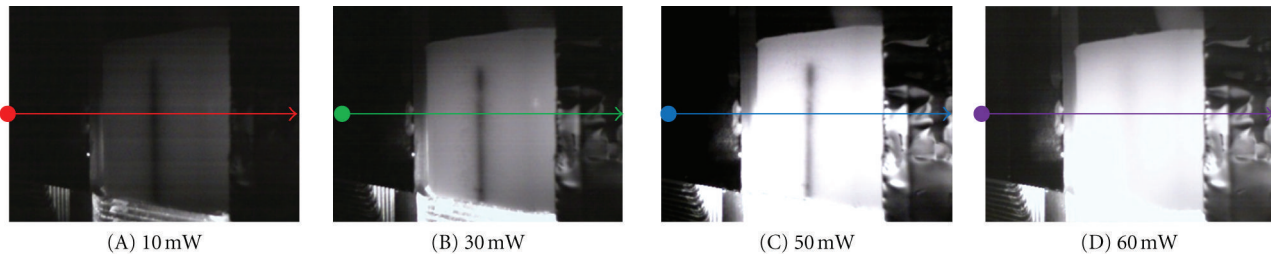


FIGURE 7: Finger phantom image and its dimensions.



(a) Photographs of artificial blood vessel with the described light powers

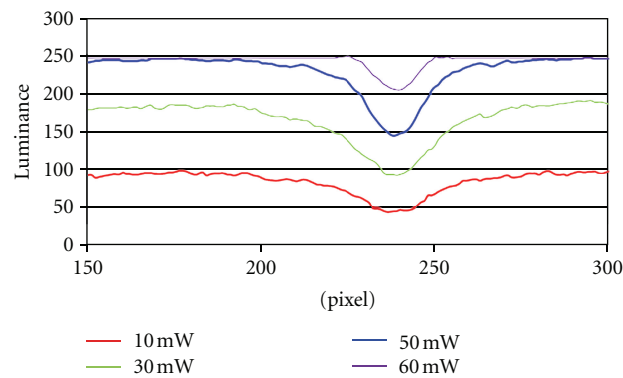


FIGURE 8: Influence of light power on the luminance distributions.

characteristics similar to those of human skin [17]. We included colored water in the artificial blood vessels.

We first increased the input power of NIR light to reduce the influence of scattering and thereby obtain a clear image. The scattering of NIR light reduces both the intensity of the transmitted light and the contrast between the artificial blood vessel and the tissue. We adopted four levels of input power of the NIR light: 10, 30, 50, and 60 mW. Figures 8(a) and 8(b) show photographs of blood vessels and luminance distributions of finger phantom images with the four input powers. Through comparison with the slope and concentration of the luminance distribution, we finally

selected 50 mW to overcome the scattering and provide the clearest image of artificial blood vessels.

We measured the depths of the artificial blood vessels using our 3D BVS system, which is based on the hybrid stereo-autofocus method. To avoid the influence of light from the environment, we covered the whole system with a light-proof cloth. First, we analyzed the images and determined the vertical distance between the reference surface of the fixed base and the line drawn between respective center points of the lenses as  $D_s$ , presented in Figure 1(a), using autofocus methods. Secondly, we measured the position of the artificial blood vessel based on the stereo method.

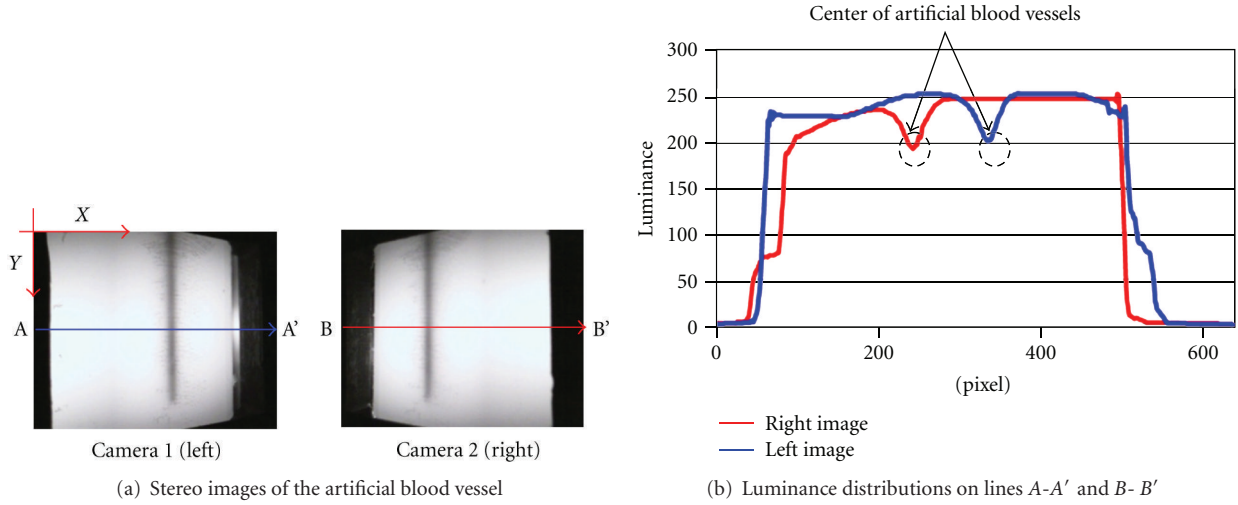


FIGURE 9: Stereo images and luminance distributions obtained using two cameras, wavelength of 870 nm.

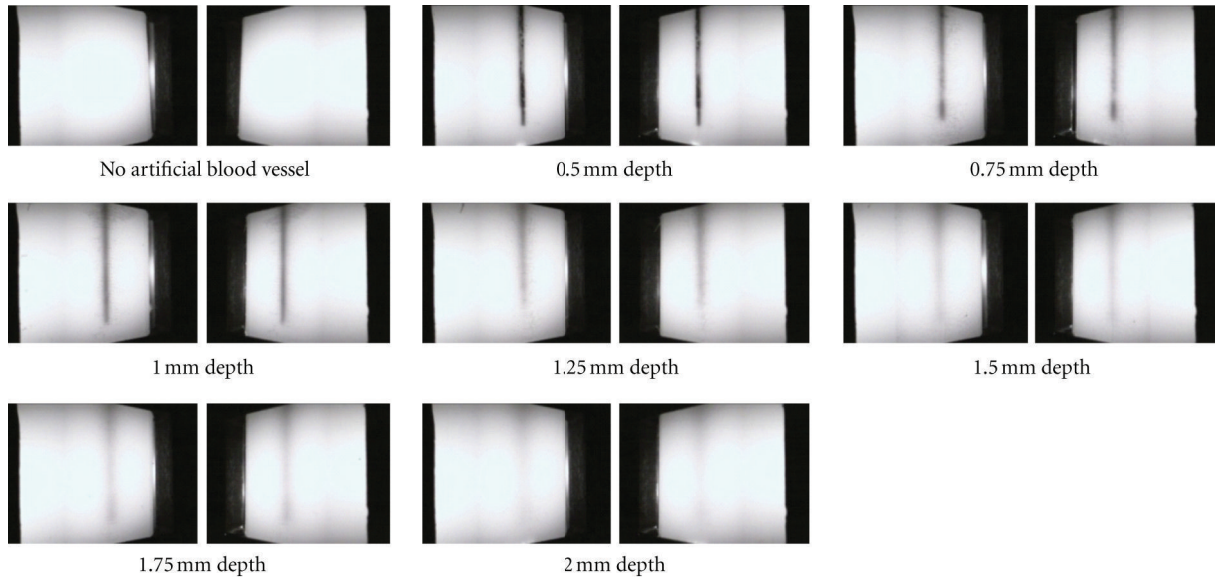


FIGURE 10: Stereo images of artificial blood vessels embedded in the finger phantom at the indicated depth.

Figure 9(a) shows stereo images of the artificial blood vessels. The rows of pixels on the center lines represented as  $A-A'$  and  $B-B'$ , as portrayed in Figure 9(a), were used to determine the center and the blood vessel depth. Pixels located on the line  $(X, Y)$  from value  $(0, 240)-(640, 240)$  provide luminance according to the eight-byte digital number, where  $X$ - $Y$  coordinates were defined as portrayed in Figure 9(a). Figure 9(b) shows that a rapid decrease in brightness is observed at the area of the blood vessel. Therefore, we are able to determine the artificial blood vessel position. The center of the artificial blood vessel position of camera 1 was set to the 327th pixel and that of camera 2 to the 316th pixel. According to Figures 1(b) and 1(c), the deviations between the center position of blood vessel and the fixed base plate in the image planes of CMOS camera 1 and 2 were 7 pixels and 4 pixels, respectively. Because the pixel size was  $5.55 \mu\text{m}$ ,

the actual deviation lengths were, respectively,  $64.8 \mu\text{m}$  in camera 1 and  $93.6 \mu\text{m}$  in camera 2. Next, the angles of light axes,  $\theta_1$  and  $\theta_2$ , as indicated in Figure 1(b), were obtained using these deviation length  $B_1$  and  $B_2$  and focal length  $f$  as shown in Figure 1(c). We then calculated the blood vessel depth  $\Delta D$  using (1) and (2). Figure 10 shows stereo images of the artificial blood vessels embedded at the indicated depths, where the left image was taken by camera 1 and the right image by camera 2,

$$\begin{aligned} \theta &= \sin^{-1}\left(\frac{\sin \theta}{n}\right), \\ \phi &= \tan^{-1}\left(\frac{f}{s}\right), \\ d &= d' \frac{\tan \theta}{\tan \phi}. \end{aligned} \quad (3)$$

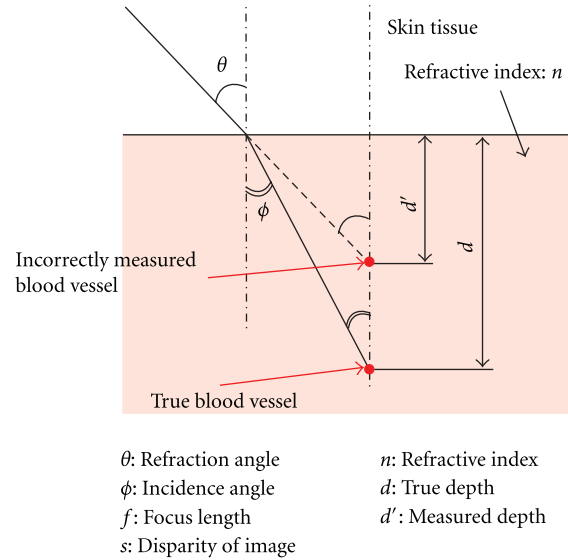


FIGURE 11: Refraction of light in the skin tissue and depth correction.

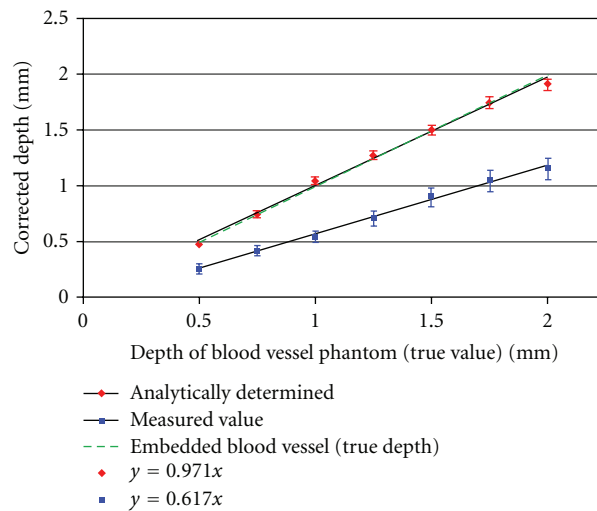


FIGURE 12: Relation between the estimated depths and true depth of artificial blood vessel.

Next, to assess the position detection accuracy of this 3D BVS detection device, we strove to eliminate the influence of the refraction of NIR light in the visualization procedure. Because the refractive index of polyacetal differs from that of air, NIR light is refracted at the interface and the difference occurs between the blood vessel position of the image and that of the actual value. Therefore, we corrected the result of the measurements based on Snell's law using the refractive index of the polyacetal as 1.48. Figure 11 shows the trajectory of NIR light from the finger phantom to the camera. Figure 11 shows that the measured depth of the blood vessel becomes smaller than the actual depth because of the refraction of NIR light. Formulas for the incidence angle, refraction angle, and the blood vessel depth are shown in (3). Using these values, we corrected the measured depth obtained using (1) and (2).

Figure 12 shows the relation between the corrected depth and the actual one, which we named "true" depth. We calculated the standard deviations in seven cases of "true" depths. In each "true" depth, we measured more than ten times and calculated the standard deviation by using the differences between the "true" depth and measured depths. It shows that the deeper the depth, the larger the standard deviation. The maximum standard deviation was  $110\ \mu\text{m}$ , and the average value of standard deviations was  $63\ \mu\text{m}$ . The average of all deviations was  $29.8\ \mu\text{m}$ , which means that average value of differences between measured and true depths in seven cases. Good correlation ( $R^2 = 0.946$ ) was found between the corrected depths and the actual depths. These errors were less than the allowance value of  $150\ \mu\text{m}$  for the targeted blood vessel with diameter greater than  $500\ \mu\text{m}$ .

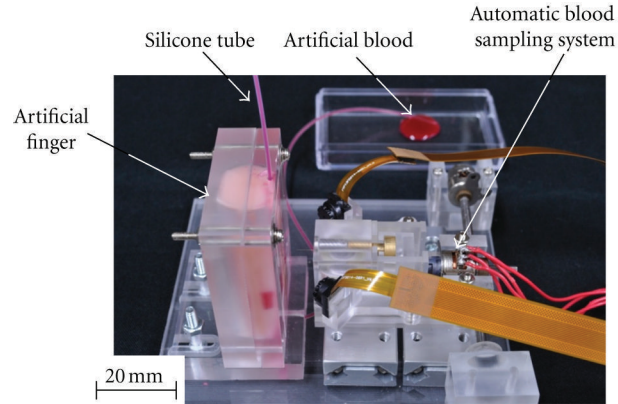


FIGURE 13: Automatic blood sampling system equipped with artificial finger and blood vessel.

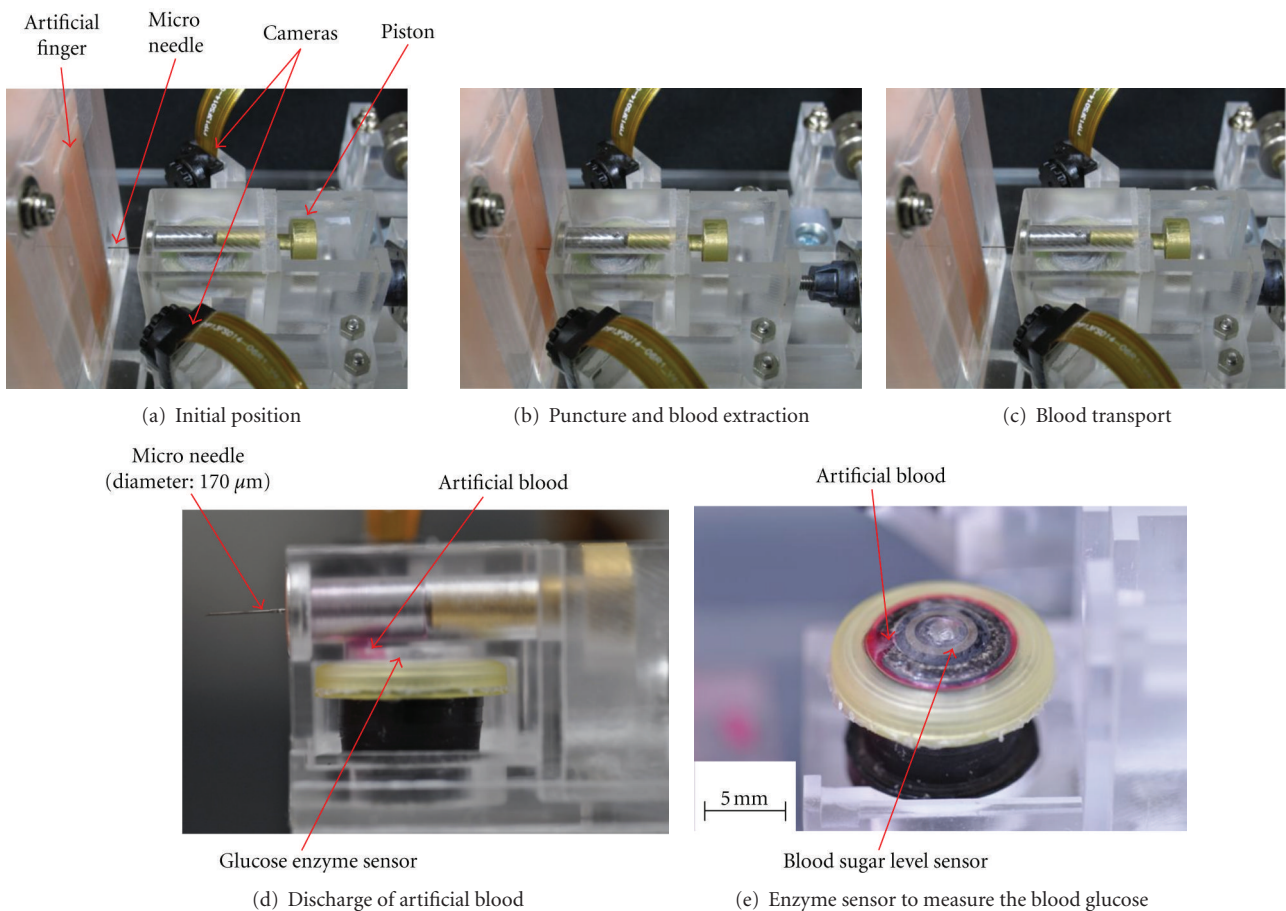


FIGURE 14: Photos of automatic blood sampling procedure and the enzyme sensor used to measure the blood glucose.

#### 4. Automatic Blood Sampling System

We fabricated an automatic blood sampling system that had been designed to be built in a portable SMBG device for use in conjunction with the 3D BVS system. In addition to two small stepping motors, we used a glucose enzyme sensor made by Horiba, Ltd. for accurate and reliable blood glucose measurement purposes [18], which was expected to perform accurate and quick blood collection. Figure 13

shows a prototype of the newly developed automatic blood sampling system, with size of  $47 \times 30 \times 20$  mm. Regarding performance evaluation, we used an artificial finger made of silicone rubber (RTV2 VP7550; Asahi Chemical Ind. Co. Ltd.), which had similar elastic properties to those of human skin. The artificial blood vessel diameter was set as 1.0 mm; the blood vessel was embedded to 1.0 mm depth in the artificial finger. We used a 50% glycerin solution, which had similar viscosity to that of human blood, as artificial blood.

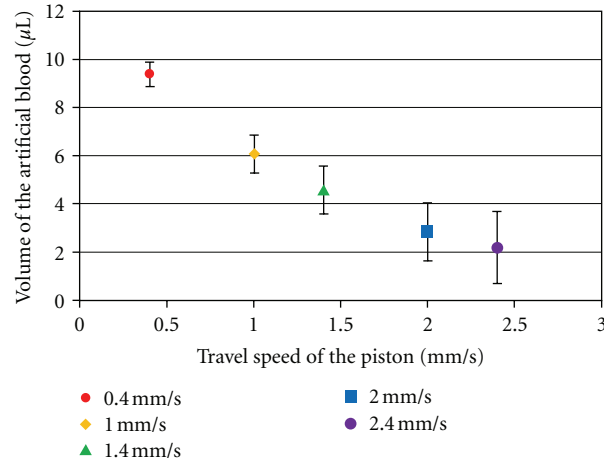


FIGURE 15: Relation between the volume of artificial blood on the sensor and the piston travel speed ( $\pm$ SD).

This artificial blood was kept in the artificial blood vessel. We examined the capabilities for puncture, blood extraction, transport, and discharge on the enzyme sensor. The glucose enzyme sensor required at least  $5.0 \mu\text{L}$  of blood for blood glucose measurements. Figures 14(a)–14(e) show four stages of blood sampling procedures, such as puncture, extraction, transport, discharge, and measurement. We analyzed blood sampling and measurement capabilities to provide  $5.0 \mu\text{L}$  of blood on the enzyme sensor. Figure 15 presents the relation between the artificial blood volume on the enzyme sensor and the piston speed for blood transport and discharge. As the piston speed decreases, the amount of artificial blood increases. We concluded that an adequate piston speed to provide over  $5.0 \mu\text{L}$  of blood for measurement was  $1.0 \text{ mm/s}$ .

## 5. Conclusions

We developed a 3D BVS system and an automatic blood sampling system to fabricate a portable SMBG device. We adopted the hybrid stereo-autofocus method to detect the position of blood vessels in three dimensions. We also examined the performance of our automatic blood sampling system, which features puncture, blood extraction, transport, and discharge for an enzyme sensor to measure the blood glucose. Results of the evaluation of our 3D BVS and automatic blood sampling devices are summarized as follows. (1) Accuracy evaluation of 3D BVS system was confirmed. The maximum standard deviation was  $111 \mu\text{m}$  and the average of the standard deviation was  $63 \mu\text{m}$  when detecting  $0.5 \text{ mm}$ -diameter blood vessels embedded at depths of  $0.5\text{--}2.5 \text{ mm}$  with  $0.25 \text{ mm}$  intervals. Results show very good correlation with actual measurements:  $R^2 = 0.946$ . (2) Blood sampling performance evaluation was done with the piston speed for blood suction and discharge selected as  $1.0 \text{ mm/s}$  to provide  $5.0 \mu\text{L}$  artificial blood on the glucose enzyme sensor. That amount was sufficient for measuring the blood glucose concentration. Our integrated system, combined with 3D BVS and automatic blood sampling systems, can be used effectively as a portable medical care system.

## References

- [1] Matsushita Co. Ltd., “Blood sugar level measurement system,” *Matsushita Technical Journal*, vol. 51, no. 3, pp. 248–253, 2005 (Japanese).
- [2] M. Miyazaki, “Reliability related to small size and simple blood sugar weighing device and the usages,” *Journal of Clinical Laboratory Instruments and Reagents*, vol. 28, no. 4, pp. 291–304, 2005 (Japanese).
- [3] N. Ozeki, Y. Kamata, Y. Okuzumi et al., “Examination related to measurement accuracy of small electrode type blood sugar measuring instrument Antisense  $\beta$ ,” *Journal of Medicine and Pharmaceutical Science*, vol. 53, no. 3, pp. 361–370, 2005 (Japanese).
- [4] K. Jungheim and T. Koschinsky, “Risky delay of hypoglycemia detection by glucose monitoring at the arm,” *Diabetes Care*, vol. 24, no. 7, pp. 1303–1306, 2001.
- [5] K. Fujita, K. Tamura, K. Wataru, H. Ishizawa, and E. Toba, “Development of noninvasive blood glucose sensor using the infrared spectroscopy,” *Transactions of the Institute of Electrical Engineers of Japan C*, vol. 129, no. 9, pp. 1759–1765, 2004 (Japanese).
- [6] T. Karatsu, D. Iwata, T. Nakajima et al., “Determination of the glucose in serum by the FT-IR-ATR method,” *Japan Analyst*, vol. 54, no. 2, pp. 149–154, 2005.
- [7] E. Nakamachi, S. Jinninn, Y. Uetsuji, K. Tsuchiya, and H. Yamamoto, “Sputter generating and characterization of a titanium alloy microneedle for applying to Bio-MEM,” *Transactions of the Japan Society of Mechanical Engineers A*, vol. 72, no. 716, pp. 471–477, 2006.
- [8] T. Asakura and H. Seino, “Basic study of a micro-tapered needle (TN-3305) used for insulin pre-filled products,” *Japanese Journal of Pharmaceutical Health Care and Sciences*, vol. 30, no. 6, pp. 368–376, 2004 (Japanese).
- [9] H. A. MacKenzie, H. S. Ashton, S. Spiers et al., “Advances in photoacoustic noninvasive glucose testing,” *Clinical Chemistry*, vol. 45, no. 9, pp. 1587–1595, 1999.
- [10] K. Yamakoshi, S. Ishimaru, A. Nakabayashi et al., “Development of a compact device for self-monitoring of venous blood glucose using miniature needle and infra-red CCD monitor,” *Transactions of the Japanese Society for Medical and Biological Engineering*, vol. 42, p. 198, 2003 (Japanese).

- [11] Y. Horiike, Y. Ogawa, M. Niihashi, A. Oki, M. Takai, and M. Nagai, "Development of a health-care-chip," *Chemical Devices*, pp. 81–85, 2004.
- [12] H. Kandani, Y. Uetsuji, K. Tsuchiya, and E. Nakamachi, "Development of blood vessel searching system for HMS," in *Proceedings of the SPIE Optics and Photonics*, vol. 7055, SanDiego, Calif, USA, 2008.
- [13] E. Nakamachi, T. Kuroda, K. Tsuchiya, Y. Uetsuji, and T. Uenoya, "Development of a three-dimensional blood vessel searching system by using the near infra-red light," *Transactions of the Japan Society of Mechanical Engineers C*, vol. 73, no. 731, pp. 2088–2094, 2007.
- [14] M. Tamura, M. Kaneko, K. Shimizu, K. Yamamoto, and T. Mikami, "Basic study for visualization of blood vessels using near-infrared light," Tech. Rep. MBE89, IEICE, 1989.
- [15] M. Kono, H. Ueki, and S. Umemura, "A new method for the identification of individuals by using of vein pattern matching of a finger," in *Proceedings of the 5th Symposium on Pattern Measurement*, pp. 9–12, Yamaguchi, Japan, 2000.
- [16] E. Nakamachi, S. Jinninn, Y. Uetsuji, K. Tsuchiya, and H. Yamamoto, "Sputter generating and characterization of a titanium alloy microneedle for applying to Bio-MEM," *Transactions of the Japan Society of Mechanical Engineers A*, vol. 72, no. 716, pp. 471–477, 2006.
- [17] N. Furuya, "3D measuring system for assembly robot using stereo camera. Camera model and parameter calibration by geometrical method," *Journal of the Japan Society for Precision Engineering*, vol. 65, no. 8, pp. 1116–1120, 1999.
- [18] E. Nakamachi, "Development of automatic operated blood sampling system for portable type self-monitoring blood glucose device," in *Proceedings of the 32nd Annual International Conference of the IEEE Engineering in Medicine and Biology Society (EMBC '10)*, pp. 335–338, September 2010.

## Research Article

# Effect of Fluorescent Particle Size on the Modulation Efficiency of Ultrasound-Modulated Fluorescence

Yuan Liu,<sup>1,2</sup> Baohong Yuan,<sup>1,2</sup> and Joseph Vignola<sup>3</sup>

<sup>1</sup> Department of Bioengineering, The University of Texas at Arlington, Arlington, TX 76019, USA

<sup>2</sup> Joint Biomedical Engineering Program, The University of Texas at Arlington, and The University of Texas Southwestern Medical Center at Dallas, TX 75390, USA

<sup>3</sup> Department of Mechanical Engineering, The Catholic University of America, Washington, DC 20064, USA

Correspondence should be addressed to Baohong Yuan, baohong@uta.edu

Received 15 July 2011; Revised 15 September 2011; Accepted 15 September 2011

Academic Editor: Nanguang Chen

Copyright © 2012 Yuan Liu et al. This is an open access article distributed under the Creative Commons Attribution License, which permits unrestricted use, distribution, and reproduction in any medium, provided the original work is properly cited.

To investigate whether the size of fluorescent particles affects the modulation efficiency of ultrasound-modulated fluorescence (UMF), we measured UMF and DC (direct current) signals of the fluorescence emission from four different-sized fluorescent particles: (1) three carboxylate-modified fluorescent microspheres (FM) with diameters of 20 nm, 200 nm, and 1.0  $\mu\text{m}$  and (2) streptavidin-conjugated Alexa Fluor 647 with a diameter of approximately 5 nm. The UMF and DC signals were simultaneously measured using a broadband lock-in amplifier and a narrowband amplifier, respectively. The ratio of the UMF strength to the DC signal strength is defined as the modulation efficiency. This modulation efficiency was then used to evaluate the effects of fluorophore size and concentration. Results show that the modulation efficiency was improved by approximately a factor of two when the size of the fluorescent particles is increased from 5 nm to 1  $\mu\text{m}$ . In addition, the linear relationship between the UMF strength and ultrasound pressure (observed in our previous study) was maintained regardless of the fluorescent particle sizes.

## 1. Introduction

Tissue fluorescence imaging has been well developed and widely used because of its high sensitivity and specificity [1, 2]. Fluorescence techniques can provide unique tissue physiological information when compared with other noninvasive imaging modalities (ultrasound, magnetic resonance imaging, computed tomography, etc.) and are sensitive to tissue microenvironments, such as tissue pH, temperature, and gas/ion concentrations. Also, they are relatively cost efficient, flexible in imaging probes selection (from organic dyes, to quantum dots, and to nanoparticles or microparticles), highly sensitive to imaging probes (fM-nM,  $10^{-15}$ – $10^{-9}$  mole/liter), and nonionizing radiative [1–3]. Commonly used high-resolution fluorescence microscopy faces a fundamental challenge due to tissue's strong optical scattering, which typically limits penetration depth to a few hundred micrometers [3]. Techniques used to image deep tissue at ranges of millimeters or centimeters, such as fluorescence diffuse optical tomography (FDOT) [4], take advantage of diffused photons that have been scattered many times before

being detected. These diffused photons can penetrate biological tissue up to tens of millimeters at the red or near infrared (NIR) region [3] at the expense of spatial resolution (limited to  $\sim 1$ – $5$  mm) [4].

Ultrasound-modulated fluorescence (UMF) has been proposed to increase spatial resolution while maintaining imaging depth [5]. This is possible because ultrasonic scattering is two to three orders of magnitude less than optical scattering in biological tissues [3]. The concept of UMF is similar to ultrasound-modulated optical tomography (UOT) [6–8], although their mechanisms may be different [9, 10]. In UMF, a focused ultrasound beam is used to tag the diffused fluorescence photons in the focal zone. By detecting and analyzing the tagged (or modulated) fluorescence photons, one can quantify the fluorescence properties in the ultrasound focal zone with ultrasonic spatial resolution that is usually much higher than the resolution of FDOT [11–15]. Recently, several research groups have investigated UMF both theoretically [5, 10] and experimentally [11–15]. The modulation efficiency of UMF is limited and has to be significantly improved for applications in biomedical imaging [11–15].

Kobayashi et al. reported a modulation efficiency in UMF adequate for tomographic imaging in a scattering medium using relatively large fluorescent microspheres ( $\sim$  microns in diameters) [11]. However, their results seem to disagree with our recently reported experimental data collected using relatively small organic fluorescent dyes (nanometers in diameters) [12, 13] and that of Hall et al. [14, 15] (see the detailed discussion about the disagreements in [12]). Therefore, the question of whether relatively large fluorescent particles ( $\sim$ microns) can reliably and significantly improve the modulation efficiency of UMF is of interest.

The study of the effect of particle size on the modulation efficiency can also lead to a better understanding of the underlying UMF mechanisms. The modulation mechanisms of UMF are quite different from those of UOT [10] due to the intrinsic incoherent properties of fluorescence emission in tissue. While UOT has been well studied using coherent light [9], the modulation mechanisms of UMF are still poorly understood due to inconsistent data in literature [11–15]. Previously, we have proposed several possible mechanisms for UMF [10]. The most plausible one is that the UMF signal is caused by periodic oscillations of the fluorophore concentration that are generated by ultrasonic pressure wave [10]. We have reported a supporting evidence of this mechanism based on a recent experimental data [12, 13]. Although this mechanism can only provide a relatively small modulation efficiency (typically  $10^{-4}$ – $10^{-6}$ ) in a scattering medium, it exists in all types of fluorophores from small nanoscale fluorescent molecules to relatively large nano-/microscale fluorescent particles [10, 12, 13]. Intuitively, one might think that it is easier to modulate large fluorescent microparticles with an ultrasound wave because larger particles may be ultrasonically oscillated more efficiently; besides, each microparticle can encapsulate more fluorescent molecules. Potentially, this could provide a means to improve the modulation efficiency of UMF. If this hypothesis is proved true, the next question would be how much improvement can be achieved and is it sufficient for biomedical imaging applications? To address these basic questions, UMF modulation efficiencies for four communally available fluorescing particles were measured and discussed in this study.

## 2. Methods

Our previous studies have shown that the UMF signal is difficult to quantify in a scattering medium due to its poor signal-to-noise ratio [13]. As a result, water was used as the medium in this study. Three fluorescent microspheres with diameters of 20 nm, 200 nm, and  $1.0\ \mu\text{m}$  were tested in this study. To further reduce the particle size, Alex Fluor 647 conjugated with streptavidin ( $\sim 1$  nm in diameter for the dye molecule and  $\sim 5$  nm in diameter for the streptavidin [16, 17]) was selected as a sample in comparison. The UMF signal was measured using a broadband lock-in amplifier, and simultaneously the fluorescent DC signal was measured using a narrowband amplifier. With both measurements calibrated, the ratio of these two quantities is recognized as the modulation efficiency. A consistent experimental setup was used for all the samples in the study so that results for different

samples could be compared. The modulation efficiency is evaluated as a function of the fluorescent particle size.

The experimental setup is shown in Figure 1. The excitation light was produced by a fiber-coupled diode laser (57ICS064/SP/HS, Melles Griot) with a wavelength of 638 nm. The monochromatic light is guided via a polarization maintaining fiber (57FTP602/FC/1.0 Melles Griot, core diameter:  $4\ \mu\text{m}$ ) to a collimating lens (F240FC-B, Thorlabs). The power density of the laser was controlled as  $411\ \text{mW}/\text{cm}^2$ . A silicon tube (FT, Instech Laboratories, inner diameter: 0.79 mm, outer diameter: 2.39 mm) was positioned in a water-filled container ( $40\ (x) \times 120\ (y) \times 120\ (z)$  mm) and orientated parallel to the  $y$ -axis. An ultrasound transducer (UST, V314-SU-F-1.00-IN-PTF, Olympus NDT, center frequency: 1 MHz) was focused on the intersection of the laser beam and the FT (see Figure 1). The UST was driven by a continuous sinusoidal signal with a frequency of 1.0 MHz that was generated from a function generator (FG, Agilent 33120A, Agilent Tech, Calif, USA) and amplified by a power amplifier (PA, 7600 M, Krohn-Hite, Mass, USA). The peak pressure at the transducer focus was measured by a hydrophone (HNP-0200, Onda Corporation, Calif, USA) and preamplifier (AH2010, Onda Corporation, Calif, USA). Two lenses (L1 and L2, AC254-030-A1, Thorlabs) were used to collect the emitted fluorescence. Long-pass emission filters (EmF, BLP01-635R, Semrock, cutoff wavelength: 650 nm) were employed to reject the excitation light. The emission photons were focused on two adjacent channels of a 16-channel photomultiplier tube (PMT, R5900U-01-L16, Hamamatsu, Japan) at the central area of this PMT to monitor the UMF and the fluorescence DC signals. The photocurrent from one channel was converted to a voltage signal using a transimpedance amplifier (TIA, 313A-1-1 pF, Analog Modules, Longwood, Florida), and its output was directed to a broadband lock-in amplifier (LIA, SR844, Stanford Research Systems, Calif, USA). The synchronized TTL (transistor-transistor logic) signal of the function generator was used as the reference signal for the LIA. The output of the LIA represents the UMF strength. The photocurrent from the second channel was directly connected to an oscilloscope (OS, TDS 3032B, Tektronix, Oregon). The input impedance of the oscilloscope was selected to be 1 Mega Ohms so that an appropriate gain can be obtained with a limited bandwidth. This signal was used to record the DC level of the fluorescence. Four sets of measurements were conducted for each sample using a new solution and tube. In each set of measurements, the UST was scanned for 3 times along the  $x$ -axis using a linear translation stage (PT1, Thorlabs, NJ, USA), and the DC and UMF signals were recorded at each selected position of the UST. The average and the standard derivation were calculated and displayed based on all the measurements.

Before any measurements were conducted, the tube was ultrasonically located by connecting the UST to a pulse generator/receiver (5077PR, Olympus NDT, Waltham, Mass, USA). The peak-to-peak voltage of the ultrasonic echoes were recorded at selected positions when scanning the UST along the  $x$ -axis. The background voltage, which was mainly caused by the electronic interference from the UST driven

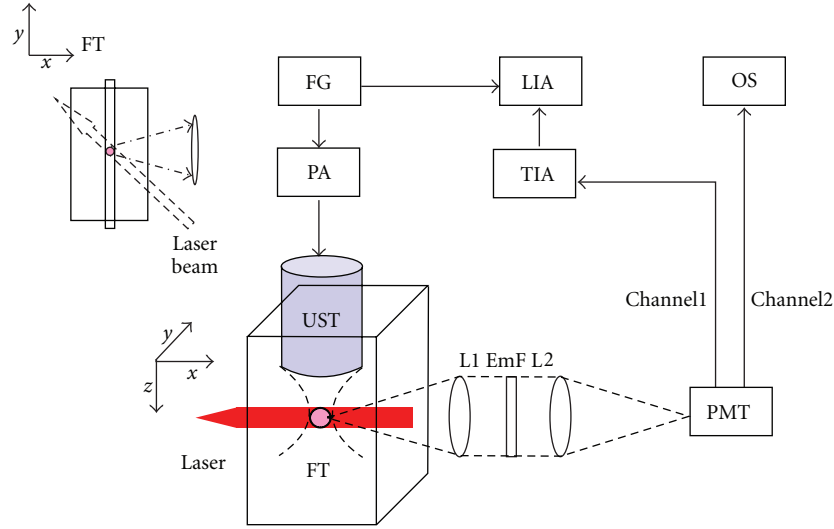


FIGURE 1: Schematic of the measurement system. FG: function generator; PA: power amplifier; UST: ultrasound transducer; FT: fluorescent tube; L1–L2: two lenses; EmF: emission filters; PMT: photomultiplier tube; TIA: transimpedance amplifier; LIA: lock-in amplifier; OS: oscilloscope. The inset represents the top view of the container and FT.

signal, was recorded when the excitation laser beam was blocked. This background voltage is independent of the UST position and can be subtracted from the measured UMF signals.

The UMF signal and the fluorescent DC signal were measured as a function of the fluorophore concentration. The concentrations of the Alexa Fluor 647 solutions (S21374, Invitrogen) were 0.025, 0.05, 0.1, and 0.2 mg/mL, and the concentrations for the fluorescent microsphere solutions (FM, F8782, F8806, F8816, FluoSpheres, Invitrogen) were 0.5, 1.0, 2.0, and 4.0 mg/mL. New clear tubes were used for each fluorescent sample to avoid the contamination from the previous sample. The effect of the tube autofluorescence is undetectable at the 638 nm excitation wavelength and can be ignored. This has been verified by detecting the UMF signal when filling the tube with water. Our results showed that the detected signal is almost a constant and independent of the location of the ultrasound transducer, which implies that no UMF signal can be detected when no fluorescent solution is present. Ideally, the linear fits of the experimental data should pass through the origin, implying that both the UMF and the fluorescence DC signals should be zero when the concentration is zero. In practice, this is not always true because of the existence of background interference and/or instrument bias. Therefore, the intercepts of the linearly fitted data were subtracted during the data processing. The ratio of the intercept-subtracted UMF signal to the intercept-subtracted DC signal is defined as the modulation efficiency. The absolute value of the modulation efficiency (the ratio) may not represent the true physical meaning of the modulation depth because the gains of the two channels may not be the same. However, because the measurement system and all experimental parameters were maintained the same for all the samples, the relative values of the defined modulation efficiency for all the samples can be compared.

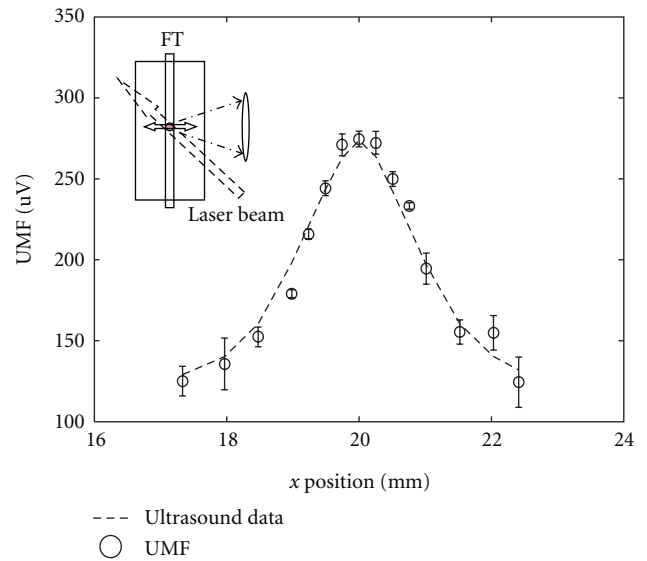


FIGURE 2: The circles with error bars represent the measured UMF signals from one of the fluorescent microsphere solutions (with the diameter of 200 nm and the concentration of 1.0 mg/mL) as a function of the  $x$  position of the UST. The dashed line shows the rescaled ultrasound signal. The inset represents the measurement configuration, and the doubled arrow shows the UST scan line.  $P_{fssp} = 180$  KPa.

### 3. Results and Discussion

Figure 2 displays the measured UMF signals (the circles with error bars) from the tube filled with 200 nm diameter FM solution (1.0 mg/mL) after scanning the UST along the  $x$ -axis. The inset shows the measurement configuration. The ultrasound data was linearly rescaled as to display both the ultrasound data and the UMF data in the same figure. The origin of the  $x$ -axis is defined as the left edge of the

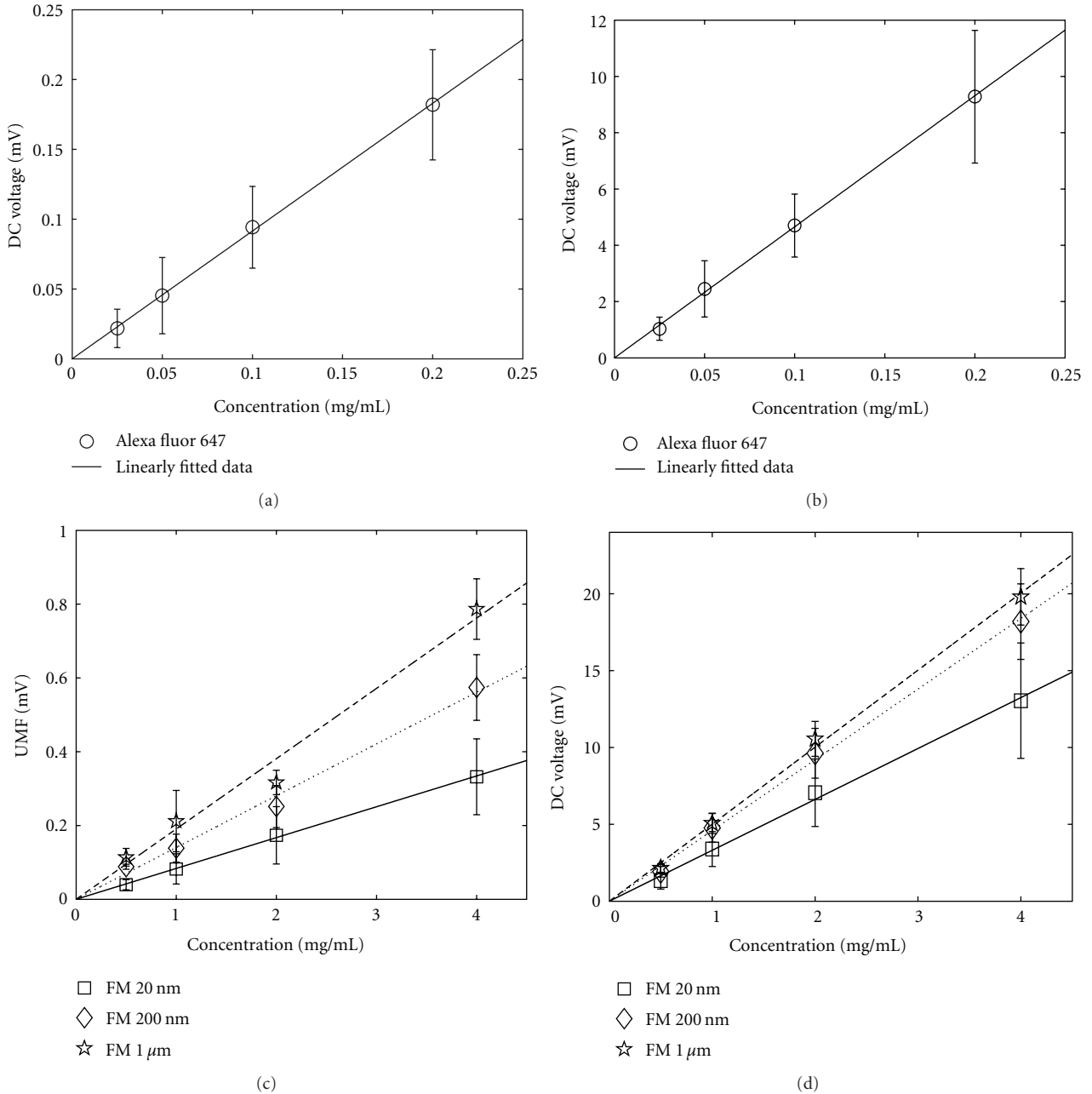


FIGURE 3: UMF and DC signals as a function of fluorophore concentration when  $x = 20$  mm,  $y = 0$  mm, and  $P_{fspp} = 180$  KPa. (a) and (b) show the UMF signal and DC signal of streptavidin-conjugated Alexa Fluor 647, respectively. The circles with error bars represent the experimentally measured data, and the solid line is the linearly fitted data. (c) and (d) show the UMF signal and DC signals from the fluorescent microsphere solutions, respectively. The squares, diamonds, and stars represent the experimentally measured data. The solid, dotted, and dashed lines are the linearly fitted data.

tank, and the tube is located at the center of the tank ( $x = 20$  and  $y = 0$  mm). The peak pressure applied at the transducer focus ( $P_{fspp}$ ) is 180 KPa. Figure 2 indicates a correlation between the UMF signal and the ultrasound. The modulation efficiency of different fluorophores is based on the peak values of the UMF signals.

Figure 3 shows the peak values of the measured UMF and DC signals from the four fluorescent particle solutions as a function of fluorophore concentration when

$P_{fspp} = 180$  KPa. Figures 3(a) and 3(b) show the UMF signal and the DC signal from the streptavidin-conjugated Alexa Fluor 647, respectively. The circles with error bars represent the experimentally measured data, and the solid lines are the linearly fitted data. Similarly, Figures 3(c) and 3(d) show the UMF signal and the DC signals from the three fluorescent microsphere solutions, respectively. The squares, diamonds, and stars represent the experimentally measured data. The solid, dotted, and dashed lines represent linear fits

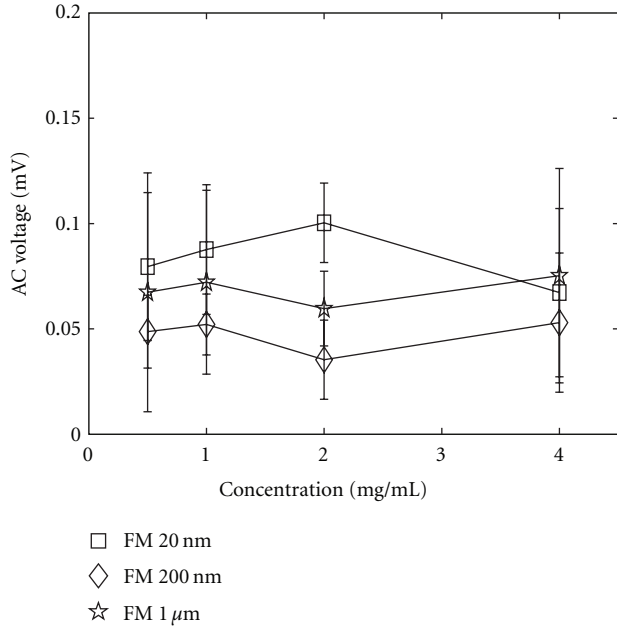


FIGURE 4: Ultrasound-modulated signal (AC voltage) of the scattered excitation light from the microsphere solutions as a function of concentration, when  $x = 20$  mm,  $y = 0$  mm, and  $P_{f_{\text{sp}}} = 180$  KPa. The squares, diamonds, and stars represent the experimentally measured data.

of the data. Figures 3(b) and 3(d) show a linear relationship between the DC signal and fluorophore concentrations from all the four samples. These linear relationships imply that the concentrations chosen in this study are appropriate and the inner filter effect or self-quenching is negligible.

To investigate the possibility of ultrasound-induced modulation of excitation light, we also detected the AC signal of the excitation light by blocking the emission light. Figure 4 shows the ultrasound-modulated signal (AC voltage) of the excitation light as a function of microsphere concentration. The squares, diamonds, and stars represent the experimentally measured data. For all three microsphere solutions, the AC signals do not vary significantly with the concentrations in the adopted range. Also, the differences of signal strengths from different particle solutions are not significant. Interestingly, the signal from 1.0 micron particles is higher than that from 200 nm particles. However, both are lower than that of 20 nm particles solution. These results indicate that modulation of the excitation light is complicated and may originate from various mechanisms [9]. Although the dominant modulation mechanism is difficult to be judged from the data shown in Figure 4, a few conclusions can be drawn based on our current and previous studies [5, 10, 12, 13]. First, the modulated fluorescence signal can be clearly observed in a solution without scatterers, such as rhodamine B aqueous solution where the fluorophores are smaller than 1 nm in diameters and do not contribute to light scattering [13]. It implies that the scatters are not necessary to generate UMF signal. Secondly, the modulation of the excitation light is not well correlated with fluorophore concentration and particle size. In contrast, the observed UMF does. This result

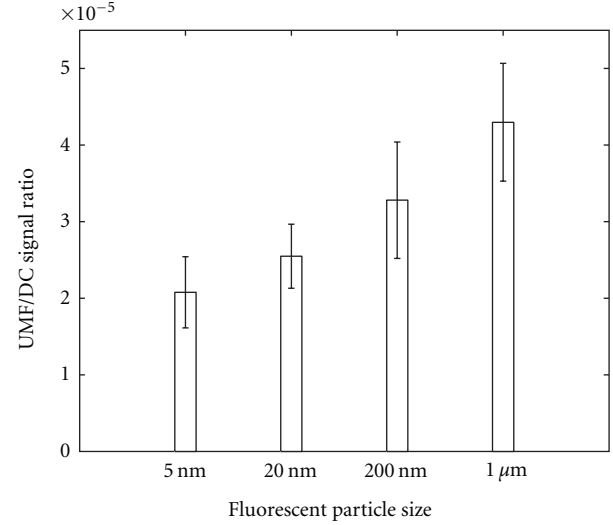


FIGURE 5: Modulation efficiencies of the four types of samples with diameters of 5 nm (as an approximation to streptavidin-conjugated Alexa Fluor 647), 20 nm, 200 nm, and 1.0 μm.

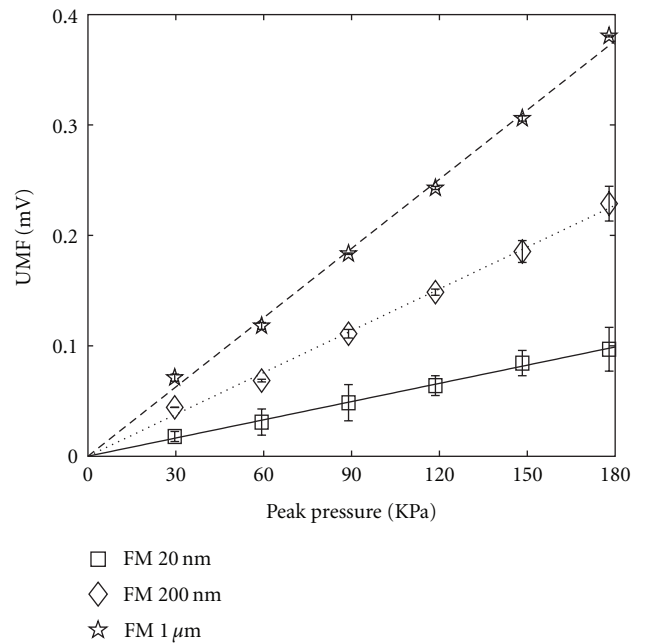


FIGURE 6: UMF signals from the fluorescent microsphere solutions with the concentration of 1.0 mg/mL as a function of  $P_{f_{\text{sp}}}$  (after the subtraction of the electronic interference) when  $x = 20$  mm  $y = 0$  mm. The squares, diamonds, and stars with error bars represent the experimentally measured data from the three different-sized microsphere solutions (20 nm, 200 nm, and 1.0 μm), respectively. The solid, dotted, and dashed lines are the linear fits.

may indicate that the modulation of the fluorophore concentration is dominant in which the unmodulated excitation light excites the modulated fluorophores.

Figure 5 shows the calculated modulation efficiencies (the ratio of the UMF signal to the fluorescence DC signal) of three FM and the streptavidin-conjugated Alexa Fluor 647

fluorescent probes. The modulation efficiency increases with increasing particle size for fluorescent microsphere solutions. The modulation efficiency of the fluorescent microsphere sample with a diameter of  $1.0\ \mu\text{m}$  is  $\sim 1.3$  times higher than that of the  $200\ \text{nm}$  diameter sample,  $\sim 1.7$  times higher than that of  $20\ \text{nm}$  diameter sample, and  $\sim 2$  times higher than that of the sample of streptavidin-conjugated Alexa Fluor 647 ( $\sim 5\ \text{nm}$  diameter). Unfortunately, the factor of 2 improvement in the modulation efficiency is limited compared to the factor of 200 increase in the size of fluorescent particles (from  $5\ \text{nm}$  to  $1\ \mu\text{m}$ ). This result implies that the observed increases in modulation efficiencies from different research groups mentioned in the introduction section cannot be justified based solely on the size differences of the adopted fluorescent particles. The finding of the size-dependent modulation efficiency in this study implies that large fluorescent particles (microns) are easier to modulate compared with small fluorescent particles (nanometers). If one assumes that the major modulation mechanism is the modulation of fluorophore concentration as discussed in our previous studies [10, 13], the current results imply that for the same concentration of the fluorophore the larger microspheres can be modulated relatively more efficiently. Note that the upper limit of the size being effective in the modulation has not been specifically studied. However, the particle size is usually limited to be smaller than capillary diameter for biomedical imaging applications. Therefore, we limited our particle size to below one micron in this study.

The peak UMF signals from the three-sized fluorescent microsphere solutions (with the concentration of  $1.0\ \text{mg/mL}$ ) were measured as a function of the peak pressure applied at the transducer focus ( $P_{\text{fspp}}$ ). The background electronic interference was measured at each  $P_{\text{fspp}}$  value and subtracted from the corresponding UMF signal. Figure 6 shows a the linear relationships between the UMF and the  $P_{\text{fspp}}$  for all the three samples. This result is consistent with our previous studies [10, 13] and indicates that the fluorescent particle size does not affect the linear relationship between the UMF strength and the ultrasound pressure [13].

#### 4. Summary

In summary, modulation efficiencies from four different-sized fluorescent particles solutions (from  $5\ \text{nm}$  to  $1\ \mu\text{m}$  scale) were measured and compared. The modulation efficiency increases by approximately a factor of two when increasing the fluorescent particle size from  $5\ \text{nanometers}$  to  $1\ \mu\text{m}$ . This size-dependent modulation efficiency indicates that large fluorescent particles can be slightly more efficiently modulated. The mechanism may be that larger particles are ultrasonically oscillated more efficiently and larger particle can encapsulate more fluorescent molecules. However, the improvement is very limited and may not be considered as a strategy to significantly improve the modulation efficiency of UMF for biological imaging applications. This study also indicates that new modulation mechanisms should be explored to gain further improvements in modulation efficiency.

#### Acknowledgments

The authors acknowledge the funding support of National Institute of Health (7R15EB012312-02), CPRIT (RP120052) and seed grant support of Research Enhancement Program from University of Texas at Arlington

#### References

- [1] W. Cai and X. Chen, "Multimodality molecular imaging of tumor angiogenesis," *Journal of Nuclear Medicine*, vol. 49, supplement 2, pp. 113S–128S, 2008.
- [2] J. R. Lakowicz, *Principles of Fluorescence Spectroscopy*, Spieinger, Berlin, Germany, 3rd edition, 2006.
- [3] L. V. Wang, "Multiscale photoacoustic microscopy and computed tomography," *Nature Photonics*, vol. 3, no. 9, pp. 503–509, 2009.
- [4] J. Culver, W. Akers, and S. Achilefu, "Multimodality molecular imaging with combined optical and SPECT/PET modalities," *Journal of Nuclear Medicine*, vol. 49, no. 2, pp. 169–172, 2008.
- [5] B. Yuan, "Theoretical study of ultrasound-modulated fluorescence photon waves in turbid media," in *Diffuse Optical Tomography and Fluorescence Diffuse Optical Tomography*, PhD Dissertation, chapter 6, University of Connecticut, Connecticut, RI, USA, 2006.
- [6] Y. Li, H. Zhang, C. Kim, K. H. Wagner, P. Hemmer, and L. V. Wang, "Pulsed ultrasound-modulated optical tomography using spectral-hole burning as a narrowband spectral filter," *Applied Physics Letters*, vol. 93, no. 1, Article ID 011111, 2008.
- [7] T. W. Murray, L. Sui, G. Maguluri et al., "Detection of ultrasound-modulated photons in diffuse media using the photorefractive effect," *Optics Letters*, vol. 29, no. 21, pp. 2509–2511, 2004.
- [8] G. Rousseau, A. Blouin, and J.-P. Monchalain, "Ultrasound-modulated optical imaging using a powerful long pulse laser," *Optics Express*, vol. 16, no. 17, pp. 12577–12590, 2008.
- [9] L. V. Wang, "Mechanisms of ultrasonic modulation of multiply scattered coherent light: an analytic model," *Physical Review Letters*, vol. 87, no. 4, Article ID 043903, 2001.
- [10] B. Yuan, J. Gamelin, and Q. Zhu, "Mechanisms of the ultrasonic modulation of fluorescence in turbid media," *Journal of Applied Physics*, vol. 104, no. 10, Article ID 103102, 2008.
- [11] M. Kobayashi, T. Mizumoto, Y. Shibuya, M. Enomoto, and M. Takeda, "Fluorescence tomography in turbid media based on acousto-optic modulation imaging," *Applied Physics Letters*, vol. 89, no. 18, Article ID 181102, 2006.
- [12] B. Yuan, Y. Liu, P. M. Mehl, and J. Vignola, "Microbubble-enhanced ultrasound-modulated fluorescence in a turbid medium," *Applied Physics Letters*, vol. 95, no. 18, Article ID 181113, 2009.
- [13] B. Yuan and Y. Liu, "Ultrasound-modulated fluorescence from rhodamine B aqueous solution," *Journal of Biomedical Optics*, vol. 15, no. 2, Article ID 021321, 2010.
- [14] D. J. Hall, U. Sunar, and S. Farshchi-Heydari, "Quadrature detection of ultrasound-modulated photons with a gain-modulated, image-intensified, CCD camera," *The Open Optics Journal*, vol. 2, pp. 75–78, 2008.
- [15] D. J. Hall, M. J. Hsu, S. Esener, and R. F. Mattrey, "Detection of ultrasound-modulated photons and enhancement with ultrasound microbubbles," *Proceedings of SPIE*, vol. 7190, article 71900L, 2009.
- [16] J. H. Shin, Y. Jiang, B. Grabowski, J. Hurwitz, and Z. Kelman, "Substrate requirements for duplex DNA translocation by the

eukaryal and archaeal minichromosome maintenance helicases," *The Journal of Biological Chemistry*, vol. 278, no. 49, pp. 49053–49062, 2003.

- [17] H. Li, S. H. Park, J. H. Reif, T. H. LaBean, and H. Yan, "DNA-templated self-assembly of protein and nanoparticle linear arrays," *Journal of the American Chemical Society*, vol. 126, no. 2, pp. 418–419, 2004.

## Research Article

# Multilayer Mie Scattering Model for Investigation of Intracellular Structural Changes in the Nucleolus and Cytoplasm

S. Saltsberger, I. Steinberg, and I. Gannot

*Department of Biomedical Engineering, Faculty of Engineering, Tel-Aviv University, Tel-Aviv 69978, Israel*

Correspondence should be addressed to I. Gannot, gannot@eng.tau.ac.il

Received 15 July 2011; Accepted 11 September 2011

Academic Editor: Baohong Yuan

Copyright © 2012 S. Saltsberger et al. This is an open access article distributed under the Creative Commons Attribution License, which permits unrestricted use, distribution, and reproduction in any medium, provided the original work is properly cited.

Light scattering from biological cells has been used for many years as a diagnostic tool. Several simulation methods of the scattering process were developed in the last decades in order to understand and predict the scattering patterns. We developed an analytical model of a multilayer spherical scattering cell. Here, we describe the model and show that the results obtained within this simple method are similar to those obtained with far more complicated methods such as finite-difference time-domain (FDTD). The multilayer model is then used to study the effects of changes in the distribution of internal cell structures like mitochondria distribution or nucleus internal structures that exist in biological cells. Such changes are related with cancerous processes within the cell as well as other cell pathologies. Results show the ability to discriminate between different cell stages related to the mitochondria distributions and to internal structure of the nucleolus.

## 1. Introduction

Light scattering from biological cells has been used for many years as a tool for the measurement and characterization of cell size and cell internal structure [1]. Automatic cellular and intracellular anatomical and physiological processes characterization might assist, in the diagnosis of pathological conditions and in controlling the effectiveness of a given therapy. In order to use light scattering to measure cellular level parameters and hence detect possible pathologies, one has to record the scattered signals, one cell at a time, and use that information to analyze the cell state.

One application in which a better model of light scattering from a single cell can be used to improve cell characterization in flow cytometry is presented in [2]. Here, flowing cells are individually probed by light and are characterized and sorted based on their scattering and/or fluorescence properties. In light scattering-based flow cytometry applications, two critical factors measured are the fractions of forward-scattered and side-scattered light (typically near 90 degrees), which are used to assess cell size and shape, respectively [2]. By plotting the forward scattered light against the side scattered light for a large number of individual cells, one can then apply statistical methods to identify various cell popu-

lations present inside of a cell suspension. Thus, any method that improves our understanding of how different structural compositions inside of single cells affect the scatter pattern can potentially have an enormous impact in applications where flow cytometry is used.

The general conclusions from the above studies about the light scattering dependence on the cell properties can be summarized as follows: gross cell size dominates the forward scattering (near zero angles) via diffraction processes. The nucleus is responsible for the scattering at slightly larger angles. Small organelles are responsible for the scattering at even larger angles, while light scattering in the backward direction (near 180 degrees) is mostly due to large subcellular structures [3].

It is clear that one needs a thorough understanding and the ability to characterize the processes and the patterns involved in the scattering of electromagnetic radiation (e.g., laser or LED light) from cells. Detailed simulation techniques are invaluable in applying cellular light scattering analysis.

To describe the scattering process in the optical domain (typically 0.4–1.1  $\mu\text{m}$ ), where the size of the investigated cells or subcellular organelles is comparable and sometimes smaller than that of the wavelength, one needs to use a full electromagnetic wave scattering theory like Mie theory.

Conceptually simpler approximations like those of Rayleigh or geometrical optics approximation cannot be applied in all of the cases [4–7].

Over the last decades, large efforts were devoted by many researchers to find theoretical and computational methods that can be used for a simulation of the scattering process of light by cells and intracellular organelles. These methods can be divided generally to analytical and numerical methods.

Analytical methods solve Maxwell's equations for an object with a given refractive index and a simple shape (e.g., a sphere, cylinder [4], or other shape [8]). The complete analytical solution of Maxwell's equations for homogenous spherical object was published by Mie at the beginning of the 20th century. More recent works used a coated sphere model to describe the cell, which consists of two spherical layers. The internal layer describes the cell's nucleus, and the outer layer describes the cytoplasm of the cell [1, 9]. Recently, more complex variations of Mie-like analytical models of the cell, that use multilayer configurations, were proposed and described in general terms [4, 10–12] and were used in a best fitting scheme between the experimental scattering pattern of blood cells and the theoretical scattering calculations in flow cytometry [13].

Numerical methods use a finite, multielement space/time grid to convert Maxwell's equations to a finite elements/differences set of equations in space and time. In the last decade, the FDTD (finite difference time domain) numerical method [14–16] has been used by several research groups in order to simulate the light scattering pattern from biological cells [17, 18]. Recent example is the work of Tanev et al. who used FDTD to simulate the interaction of light with cellular structures [19] and applications for flow cell cytometry [20]. The discrete set of equations can be solved using numerical methods, to give the resulting distribution of electromagnetic fields in the cell and in its close vicinity. One then can get the electromagnetic field distribution in the far-field using “near to far field transformation” [16]. The main advantage of the FDTD and other numerical methods is the ability to simulate cells of arbitrary structures and not just “idealized” geometrical shapes.

However, numerical solutions might consume a large amount of computing resources because of the large number of grid elements that need to be handled even in a moderately

complex problem. Moreover, in most cases one only has a simplified and idealized knowledge on the cell shape and internal structure.

In this paper, we are describing a multilayer Mie-like model that was developed to study the effects of spherically symmetric refractive index distributions on the scattering patterns of light scattered from a single cell. We show that the predictions of such model are similar to results of an FDTD model. Then, we investigate different mitochondria distributions in the cell. It was shown that cancerous processes are responsible for changes in the mitochondria distributions, and therefore, detection of such changes is of great interest. We also study the effect of internucleic structures. We demonstrate how high and low spatial frequency (hence detailed fine structure) fluctuations in the refractive index of the nucleus affect the light scattering.

## 2. Models and Methods

*2.1. The Multilayer Sphere Model.* The basic multilayer sphere model for electromagnetic scattering was described in the literature long ago [4, 21]. Enhancements to the model and to the computational algorithms were described later [10, 11, 22, 23]. The basic model is depicted in Figure 1. We are using the notation of Kerker [4].

In Figure 1,

$$\alpha_i = \frac{2\pi r_i}{\lambda_i}, \quad 1 \leq i \leq L, \quad (1)$$

is the Mie size parameter of the  $i$ th spherical shell which has a radius  $r_i$  measured from the cell center.  $\lambda_0$  is the wavelength of the radiation in the external medium (with index  $m_0$ ).  $m_i$  is the (possibly complex) refractive index of the respective layer.

Obtained from the multilayer Mie model are the Mie scattering coefficients  $a_n$  and  $b_n$  which are equivalent to, but somewhat more complicated from, the coefficients in the case of a homogeneous sphere (one-layer model) [4]. The index  $n$  is used in summations of Mie coefficients as will be outlined below. The coefficients  $a_n$  and  $b_n$  are given as a ratio of two determinants.

$$a_n = \frac{\begin{vmatrix} \psi'_n(m_1\alpha_1) & \psi'_n(m_2\alpha_1) & \chi'_n(m_1\alpha_1) & 0 & 0 & \cdots & 0 & 0 & 0 \\ m_1\psi_n(m_1\alpha_1) & m_2\psi_n(m_2\alpha_1) & m_2\chi_n(m_2\alpha_1) & 0 & 0 & \cdots & 0 & 0 & 0 \\ 0 & \psi'_n(m_2\alpha_2) & \chi'_n(m_2\alpha_2) & \psi_n(m_3\alpha_2) & \chi_n(m_3\alpha_2) & \cdots & 0 & 0 & 0 \\ 0 & m_2\psi_n(m_2\alpha_2) & m_2\chi_n(m_2\alpha_2) & m_3\psi_n(m_3\alpha_2) & m_3\chi_n(m_3\alpha_2) & \cdots & 0 & 0 & 0 \\ 0 & 0 & 0 & \psi'_n(m_3\alpha_3) & \chi'_n(m_3\alpha_3) & \cdots & 0 & 0 & 0 \\ 0 & 0 & 0 & m_3\psi_n(m_3\alpha_3) & m_3\chi_n(m_3\alpha_3) & \cdots & 0 & 0 & 0 \\ 0 & 0 & 0 & 0 & 0 & \cdots & 0 & 0 & 0 \\ 0 & 0 & 0 & 0 & 0 & \cdots & 0 & 0 & 0 \\ 0 & 0 & 0 & 0 & 0 & \cdots & \psi'_n(m_L\alpha_L) & \chi'_n(m_L\alpha_L) & \psi'_n(\alpha_L) \\ 0 & 0 & 0 & 0 & 0 & \cdots & m_L\psi_n(m_L\alpha_L) & m_L\chi_n(m_L\alpha_L) & \psi_n(\alpha_L) \end{vmatrix}}{\begin{vmatrix} \psi'_n(m_1\alpha_1) & \psi'_n(m_2\alpha_1) & \chi'_n(m_1\alpha_1) & 0 & 0 & \cdots & 0 & 0 & 0 \\ m_1\psi_n(m_1\alpha_1) & m_2\psi_n(m_2\alpha_1) & m_2\chi_n(m_2\alpha_1) & 0 & 0 & \cdots & 0 & 0 & 0 \\ 0 & \psi'_n(m_2\alpha_2) & \chi'_n(m_2\alpha_2) & \psi_n(m_3\alpha_2) & \chi_n(m_3\alpha_2) & \cdots & 0 & 0 & 0 \\ 0 & m_2\psi_n(m_2\alpha_2) & m_2\chi_n(m_2\alpha_2) & m_3\psi_n(m_3\alpha_2) & m_3\chi_n(m_3\alpha_2) & \cdots & 0 & 0 & 0 \\ 0 & 0 & 0 & \psi'_n(m_3\alpha_3) & \chi'_n(m_3\alpha_3) & \cdots & 0 & 0 & 0 \\ 0 & 0 & 0 & m_3\psi_n(m_3\alpha_3) & m_3\chi_n(m_3\alpha_3) & \cdots & 0 & 0 & 0 \\ 0 & 0 & 0 & 0 & 0 & \cdots & 0 & 0 & 0 \\ 0 & 0 & 0 & 0 & 0 & \cdots & 0 & 0 & 0 \\ 0 & 0 & 0 & 0 & 0 & \cdots & \psi'_n(m_L\alpha_L) & \chi'_n(m_L\alpha_L) & \psi'_n(\alpha_L) \\ 0 & 0 & 0 & 0 & 0 & \cdots & m_L\psi_n(m_L\alpha_L) & m_L\chi_n(m_L\alpha_L) & \psi_n(\alpha_L) \end{vmatrix}}, \quad (2)$$

| Same as above except that  $\psi'_n(\alpha_i)$  and  $\psi_n(\alpha_i)$  are replaced by  $\zeta'_n(\alpha_i)$  and  $\zeta_n(\alpha_i)$ , respectively |

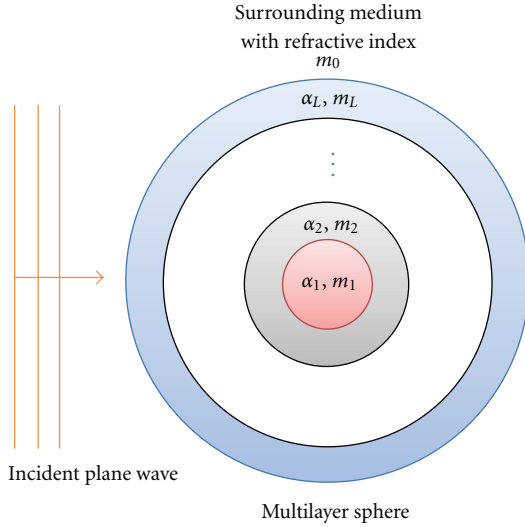


FIGURE 1: Multilayer sphere model with  $L$  layers and zero indexed environment parameters. A plane electromagnetic wave is coming from the left.

where primes denote the derivative of the respective function and the various functions in (2) are outlined below [4, 24, 25]

$$\begin{aligned}\psi_n(x) &= \sqrt{0.5\pi x} J_{n+1/2}(x), \\ \chi_n(x) &= -\sqrt{0.5\pi x} N_{n+1/2}(x).\end{aligned}\quad (3)$$

These are the Ricatti-Bessel functions of the first and second kind, respectively, and  $J_{n+1/2}(x)$  and  $N_{n+1/2}(x)$  are the half integral-order Bessel functions of the first and the second kinds (the second kind function called also Neumann function).

The function  $\zeta_n(x)$  is the Ricatti-Bessel function of the third kind defined by

$$\zeta_n(x) = \psi_n(x) + i\chi_n(x).\quad (4)$$

The solution for  $b_n$  can be obtained from that of  $a_n$  by raising the “ $m$ ’s” from the even numbered rows of the determinants to the odd numbered rows immediately above. The actual dimensions of the determinants depend on the number of layers in the model and are given by

$$\dim = 2L,\quad (5)$$

where  $L$  is the number of layers. We investigated a model which contains up to 4 layers, which gives us determinants with dimensions of  $8 \times 8$ .

Knowing  $a_n$  and  $b_n$ , we can calculate the amplitude of the scattered electromagnetic waves in a given scattering angle  $\theta$

and in any of the two possible polarizations: parallel and perpendicular

$$\begin{aligned}S_1(\alpha, m, \theta) &= \sum_{n=1}^{\infty} \frac{2n+1}{n(n+1)} \{a_n(\alpha, m)\pi_n(\cos \theta) + b_n(\alpha, m)\tau_n(\cos \theta)\}, \\ S_2(\alpha, m, \theta) &= \sum_{n=1}^{\infty} \frac{2n+1}{n(n+1)} \{a_n(\alpha, m)\tau_n(\cos \theta) + b_n(\alpha, m)\pi_n(\cos \theta)\}.\end{aligned}\quad (6)$$

In the case of multilayer model, the Mie size parameter and the complex refractive index are vectors with one component for every layer. The angular functions  $\pi_n$  and  $\tau_n$  are defined by

$$\begin{aligned}\pi_n(\cos \theta) &= \frac{P_n^{(1)}(\cos \theta)}{\sin \theta}, \\ \tau_n(\cos \theta) &= \frac{d}{d\theta} P_n^{(1)}(\cos \theta),\end{aligned}\quad (7)$$

where

$$P_n^{(1)}(x) = \frac{1}{2^n n!} (1-x^2)^{1/2} \frac{d^{n+1}}{dx^{n+1}} (x^2-1)^n \quad (8)$$

is the associated Legendre polynomial of order  $n$  and degree 1 [4].

The corresponding measurable intensity functions can be obtained from the amplitudes (6) by

$$\begin{aligned}i_1(\alpha, m, \theta) &= |S_1(\alpha, m, \theta)|^2, \\ i_2(\alpha, m, \theta) &= |S_2(\alpha, m, \theta)|^2.\end{aligned}\quad (9)$$

In a computer code, an important consideration to be made is the number of terms  $n_c$  to be taken for the amplitude series (6) in order to preserve the required numerical precision. A relatively simple criterion for the number of terms exist in the literature [26–28]

$$n_c = \text{Round}(\alpha + 4.05\alpha^{1/3} + 2), \quad (10)$$

where the Round function means rounding to the nearest integer. It can be seen by a simple calculation that the size parameter  $\alpha$  for a typical case of biological cell with a radius of  $5 \mu\text{m}$  and the wavelength of  $0.5 \mu\text{m}$  is approximately 63. Therefore, the number of terms required is 81.

## 2.2. Mitochondria and Nucleus Refractive Index Fluctuations Distribution in the Multilayer Model.

In order to study the mitochondrial distribution effect on the light scattering pattern of the cell, we divided the cell interior to 4 parts or zones as depicted in Figure 2: the nucleus (1), the perinuclear zone (2), the mid zone (3), and the membrane zone (4). The surrounding media is composed Extra Cellular Fluid (ECF).

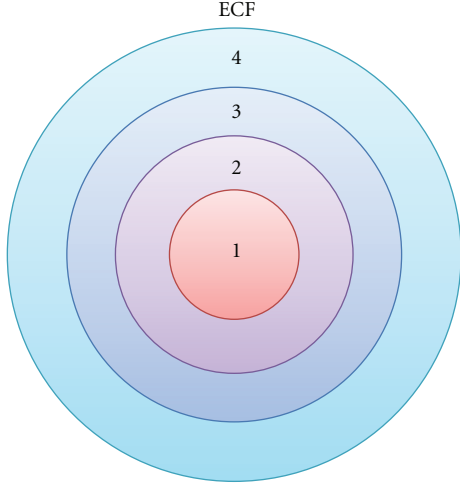


FIGURE 2: 4 layer sphere model: (1) Nucleus, (2) Perinuclear zone, (3) Mid zone (4) membrane zone. The surrounding is Extra Cellular Fluid (ECF).

We assume that the mitochondria distribution is represented by an equivalent distribution of refractive index in the cytoplasm region of the cell. Different cell types or states manifest themselves in the existence of certain amount of mitochondria in one of the cytoplasm zones defined above. The radii of the nucleus and of the membrane zone (i.e., whole cell's radius) are taken from the literature [17] as well as the refractive indices of the various parts of the cell and its environment. Since we divided the distance from the nucleus membrane to the cell membrane into three equal parts, the radii of the perinuclear zone and the mid zone are also determined.

The equivalent refractive index is the volume average of the cytoplasm and the mitochondria refractive indices in a certain zone. In order to calculate the volume averaged refracted index, we used the following formulas:

$$m_{avr,i} = v_{mito,i} m_{mito} + v_{cyto,i} m_{cyto},$$

$$v_{mito,i} = \frac{1}{r_i^3 - r_{i-1}^3} \sum_{j=1}^{N_i} \rho_{mito,j}^3, \quad (11)$$

$$v_{cyto,i} = 1 - v_{mito,i},$$

where,  $i$ : zone index, that can takes one of the values 2,3 or 4 for perinuclear, mid and membrane zone respectively;  $m_{mito}, m_{cyto}$ : refractive index of the mitochondria and the cytoplasm respectively;  $v_{mito,i}, v_{cyto,i}$ : volume fraction of mitochondria and cytoplasm respectively in zone  $i$ ;  $m_{avr,i}$ : average (effective) refractive index of the zone  $i$ ;  $r_i$ : radius of the zone  $i$ , measured from cell's center;  $\rho_{mito,j}$ : radius of the  $j$ th mitochondrion (in the zone  $i$ );  $N_i$ : number of mitochondrion in the zone  $i$ .

In (11) above, the total mitochondria volume can be calculated as the sum of all the single mitochondrion volumes in the respective zone  $i$ . Every mitochondrion is modeled as a sphere with radius  $\rho_{mito,j}$ .

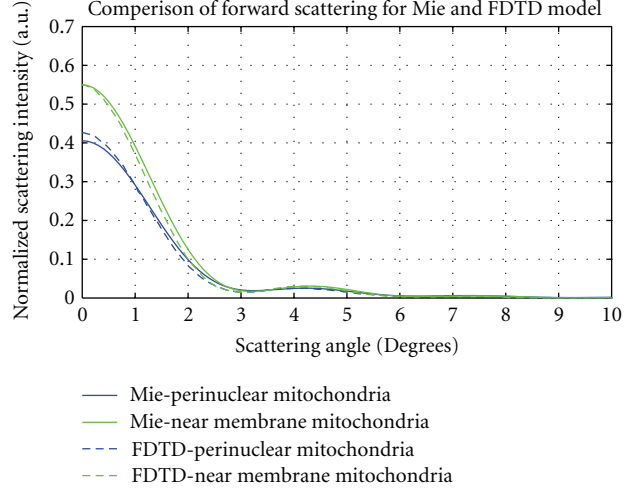


FIGURE 3: Forward scattering intensity as a function of scattering angle. Full lines: analytic multilayer Mie model. Dashed lines: Numerical FDTD model from Figure 2(a) of Su et al. [18] showing similar behavior. Both perinuclear mitochondria (blue) and near membrane mitochondria cases (red) are shown.

Changes in the nucleus might result in coarser or fine structures of the refractive index at the nucleolus compared to a normal cell. This means lower or higher spatial frequency content of the refractive index fluctuation in the nucleolus. In the multilayer model it is natural to approximate the nucleus refractive index fluctuations as a nucleus with  $N$  spherical shells with spatial frequency of  $0.5N r_{nuc}^{-1}$  cycles/ $\mu\text{m}$ , where  $r_{nuc}$  is the radius of the nucleus in microns. The refractive index of odd shells is  $m_{avr} - \Delta m$  and of even shells is  $m_{avr} + \Delta m$  where  $\Delta m$  is relatively small amount.

### 3. Results

**3.1. Comparison with FDTD Model.** The details of the near forward scattering (0–10 degrees) pattern of the average polarization are shown in Figure 3 below. For comparison, the data from Figure 2(a) of Su et al. [18], which is a result of FDTD computation for a similar geometry, is plotted in dashed lines. Refractive indices and radii were taken to match Su et al. [18]. However, randomization of the mitochondria locations was neglected and replaced with spatial averaging as discussed in Section 2.2. The results of both calculations are very similar for both perinuclear mitochondria and near membrane mitochondria.

**3.2. Mitochondria Distribution Effects.** For further investigation of the effects of different mitochondria distributions, the multilayer model was run with the following parameters. These parameters are taken from previous publications [17, 18] and their values are summarized in Table 1. The radii of zones 2, 3, 4 in the cytoplasm (see Figure 2 above) were taken to be equal.

Based on these parameters, the scattering intensities functions  $i_1$  and  $i_2$  (parallel and perpendicular polarizations resp.) were plotted. Figures 4(a) and 4(b) show the intensities

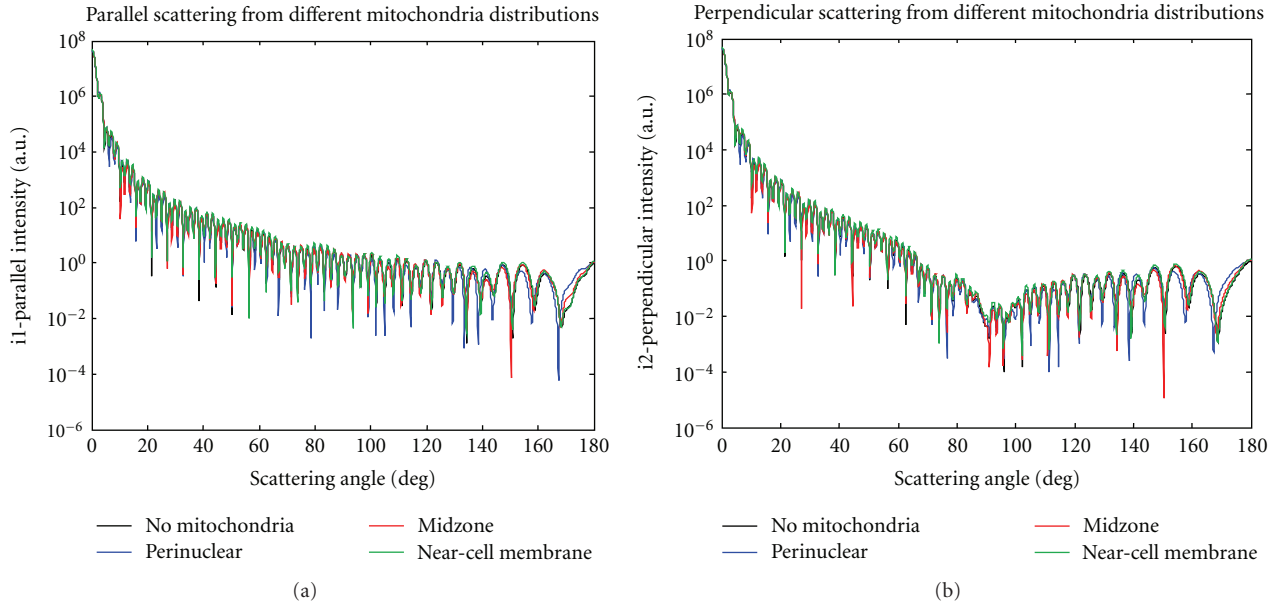


FIGURE 4: Scattered intensities as a function of scattering angles for different mitochondria distributions. (a)  $i_1$  parallel polarization, (b)  $i_2$  perpendicular polarization. The different colors represent different mitochondria distributions.

TABLE 1: Summary of simulation parameters.

Item	Value	Units	Comments
Number of mitochondria	180	No.	In the cytoplasm
Mitochondrion radius	0.35	$\mu\text{m}$	
Laser wavelength	0.488	$\mu\text{m}$	For argon laser
Cell's radius	7.50	$\mu\text{m}$	
Nucleus radius	2.50	$\mu\text{m}$	
Extracellular fluid's index of refraction	1.35	No.	Relative to vacuum
Cytoplasm's index of refraction	1.37	No.	Relative to vacuum
Mitochondria's index of refraction	1.42	No.	Relative to vacuum
Nucleus' index of refraction	1.39	No.	Relative to vacuum

as a function of the scattering angle (forward is a zero scattering angle) for a few mitochondria distribution of interest. Due to the exponentially decaying nature of the intensities, the magnitude is shown in logarithmic scale in order to see the behavior in large scattering angles.

Since the overall differences between cases are small, we focus on side-scattering which is related to cell structure. Figure 5 zooms into this region of interest to show the differences in the  $i_2$  side-scattering between mitochondria distributions. Here mitochondria positions were randomized ten times for each distribution to see the variance of these different situations. One can deduce from the figure that the further the mitochondria displaced from the nucleus the

stronger is the side scattering. Similar results can be obtained for the  $i_1$  intensity.

Finally, as mentioned before, it is a common practice in cell cytometry to plot side scattering intensity versus forward scattering intensity in order to cluster different cell types. This allows the application of a wide array of classifiers and clustering algorithms. Therefore, we plotted the results from Figures 4 and 5 in such manner for the different mitochondria distributions. The result is presented in Figure 6 below.

**3.3. Nuclear Fine Structure Effects.** In order to study the effects of the nuclear fine structures on the light scattering pattern we used the multilayer model with several spatial frequencies in the nucleus.

The results for homogenous nucleus and nucleus with 25, 37, 50 layers of refractive index modulation (spatial frequency of 5, 7.5, 10 cycles/micrometer) are depicted in Figures 7(a), 7(b) and 7(c) below.

We observe major differences between homogenous nucleolus and multilayered nucleus. Similar results are obtained for the  $i_2$  scattering intensity.

## 4. Discussion and Conclusions

We have developed and implemented a MATLAB multilayer Mie-like model for the scattering of light from biological cells that have internal structures with spherical symmetry. The multilayer Mie-like model can be used for exvivo and invivo simulation of light scattering from biological cells.

The model is somewhat simpler than the complex Finite-Difference Time-Domain (FDTD) cell models that were recently published and used by several groups [14–18, 29]. We have showed in Figure 3 that the multilayer model gives

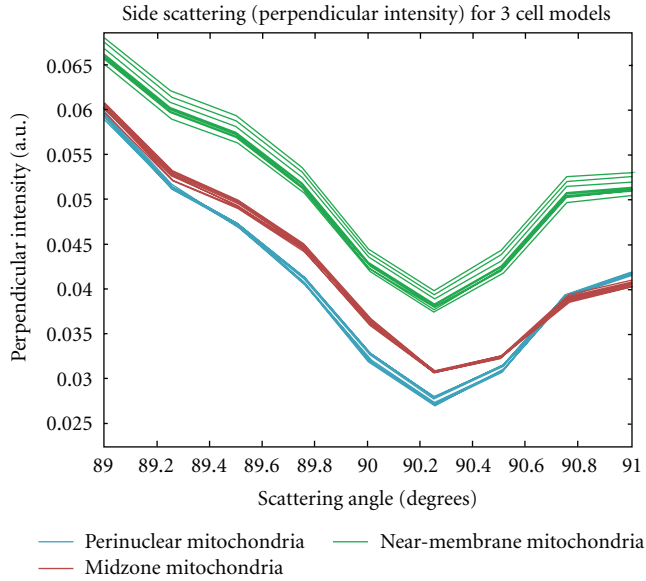


FIGURE 5: Side-scattering intensity  $i_2$  for different mitochondria distributions. For each different distribution (represented by different color) 10 realizations of the mitochondria positions were randomized to show the variance in scattering intensity.

similar results as the FDTD model for cases having spherical symmetry in the refractive index distribution in the cell. For both perinuclear distributed and near-membrane distributed mitochondria, there is a very reasonable equivalence between the simplified analytical multilayer Mie model and the more complicated FDTD model in case of spherical symmetry.

The effect of the mitochondria distribution and quantity on the cell's light scattering pattern is an example to a cellular-based optical diagnosis method [18]. It has been shown that mitochondrial aggregation near the nuclear periphery will occur in normal cells in preparation for mitosis, while in the rest of the normal cell's life the mitochondria is distributed randomly in the cytoplasm. It also has been observed that mitochondrial hyperplasia can be encountered in tumors from different organs, (also called oncocytoomas) [30]. In Figure 4, which plots the scattering patterns of the 3 cell types on a log scale, the scatter patterns of the 3 cell types appear similar. However, when the data is plotted on a linear scale, differences between normal (perinuclear mitochondria), precancerous (midzone mitochondria), and cancerous (near-membrane mitochondria) cells begin to emerge, mostly for the side scattering intensity (shown in Figure 5), with the fraction of scattered light being roughly 30% higher in cancerous cells than normal or precancerous cells. The forward scattering component is slightly less sensitive to the location of mitochondria.

These results are consistent with earlier findings in flow cytometry that show that the side scatter component is more sensitive to cell structure, while the forward scatter component is more sensitive to cell size [2]. Moreover, plotting the simulation output on a scatter plot, as is frequently done in flow cytometry data, reveals that the 3 cell groups can be easily classified. The ability to assess intracellular structures

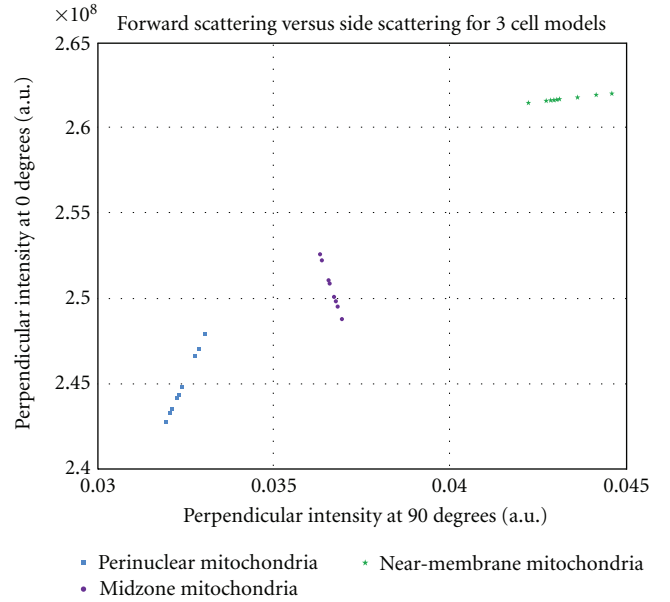


FIGURE 6: Scatter plot of the  $i_2$  forward scattering intensity versus the  $i_2$  side scattering intensity for the 10 realizations of each of the 3 different mitochondria distributions. This plot clearly shows the differentiation between the cases and spread of each distribution.

such as location of mitochondria using flow cytometry can add a new dimension to this well-established method.

Although the model is based on concentric spherical layers, the actual shape of cells frequently deviates from this geometry. If the cells had a more oblong, ellipsoidal shape (with the long axis perpendicular to the incoming incident wave), we suspect that the scatter patterns would deviate from Figures 4–6 in that there would be less light scattered in the  $90^\circ$  direction, while there would be more light scattered in the forward direction. Alternatively, if the cells had long dendritic-like processes, we expect higher intensity in the  $90^\circ$  direction and less light in the forward direction. Of note, many cancers originate in epithelial tissue that has more spherical/ellipsoidal shape than a dendritic shape [31].

While noncancerous cells often exhibit round or otherwise ordered shape, cancerous cells often appear with irregular shapes. The lack of symmetry of such cells prevents simple analytical modeling, enforcing regression to the more complex FDTD models. In such cases, the importance of the analytical Mie model is double. First, as explained in the introduction, scattering at large angles is related to sub-cellular organs and unrelated to the overall shape of the cell. Thus, the Mie model described here is a fair estimate of the scattering at large angles even for irregular-shaped cells. Second, since each cell is measured with respect to a random frame of reference, the average scattering from a population of irregular-shaped cells is similar to that of a hypothetical spherical cell described by the Mie model presented here.

Another example to a possible diagnostic feature is the nonuniformity of the refractive index in the cell nucleus. It is known that the refractive index in a certain point in the nucleus (and also in the cell) is a function of several factors,

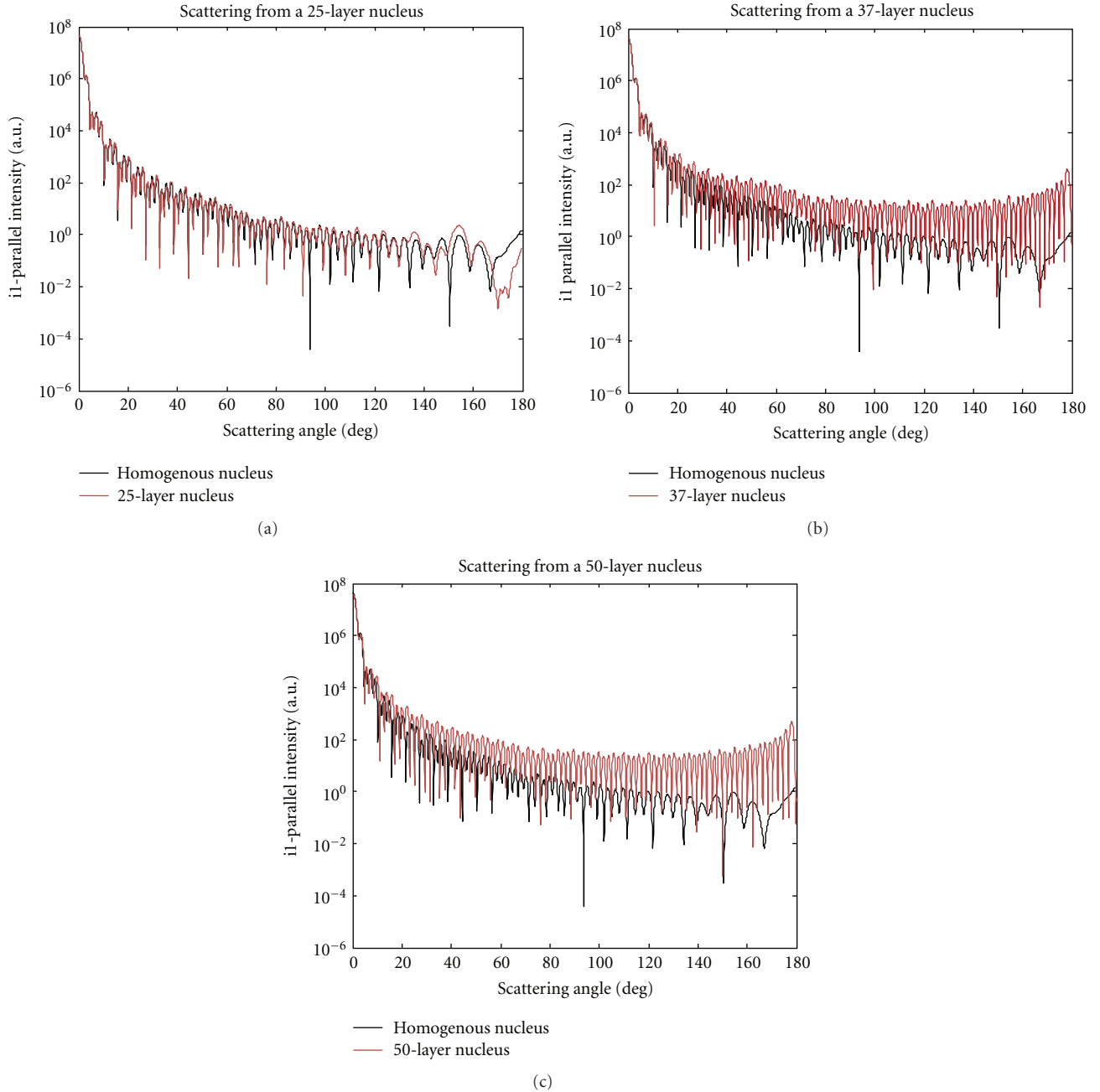


FIGURE 7: (a) Parallel component of the scattered intensity  $i_1$  as a function of the scattering angle for a nucleus with refractive index fluctuations (layers) of 5 cycles/micron spatial frequency. (b) Parallel component of the scattered intensity  $i_1$  as a function of the scattering angle for a nucleus with refractive index fluctuations of 7.5 cycles/micron spatial frequency. (c) Parallel component of the scattered intensity  $i_1$  as a function of the scattering angle for a nucleus with refractive index fluctuations of 10 cycles per micron spatial frequency.

including protein concentration [32]. As the cell goes through its life cycle, the protein concentration in the nucleus and hence the refractive index distribution is changing because of the preparation to and the beginning of the cell mitosis [33]. Nucleus refractive index nonuniformity effects on the light scattering pattern had been recently investigated using FDTD methods [17]. The main result was that higher frequency fluctuation in the nucleus refractive index results in more scattering in the angles between 50 and 160 degrees.

It was also shown in the literature [34] that the nucleus of cancer cells depicts internal structural changes, compared with normal cells. These changes are specific to the cancer type and can assist in diagnosis and staging.

Applying the multilayer Mie model, we can see that in general, the scattering becomes higher as the spatial frequency of the refractive index variation is higher. This is true for high scattering angle, not in the forward direction but from 10 to 20 degrees. This result is in general agreement

with Drezek et al. [17] that used the FDTD method for their simulation, although that in their simulation they used refractive index patterns in the cytoplasm rather than in the nucleus.

Another interesting feature that we see is the regular peaks pattern that becomes visible for higher spatial frequencies. This pattern is not present in the FDTD simulation [17]. The difference can be explained by the fact that we used very regular periodic spherically symmetric structure of refractive index distribution. The periodic structure is in fact like a 3D spatial diffraction grating, giving rise to many resonance peaks in the diffraction pattern. The FDTD simulation [17], on the other hand, used a non-periodic patterns like certain number of organelles of specific size and refractive index at specific locations or randomly generated refractive index patterns with a certain range and frequency of fluctuations. The randomness nature of the patterns they used was acted as an averaging component that prevents the creation of resonant peaks because of the random phase of the interference. The resulting scattering pattern is much less coherent as in our regular periodic case.

In the future, we intend to check its potential use in an algorithm for a cell classification system. A single-cell classification algorithms are used routinely, for example, in a cell cytometry equipment [2]. The behavior near the forward direction probably can be used as a discriminating feature in an automatic cell classifier.

Another potential application that can use this model is the calculation of the invivo back-scattering from a tissue bulk that composed of many cells, some of them depict a pathology in a certain level. The purpose of the calculations in this case is to enable a classification of invivo intracell level pathologies or the staging of pathology as a part of a therapy. In this case, one needs to compute the aggregate effect of the scattering from many cells and also incorporate the tissue matrix and the (possibly variable) blood effect on the back-scattering.

## References

- [1] R. A. Meyer and A. Brunsting, "Light scattering from nucleated biological cells," *Biophysical Journal*, vol. 15, no. 3, pp. 191–203, 1975.
- [2] H. M. Shapiro, *Practical Flow Cytometry*, John Wiley & Sons, New York, NY, USA, 4th edition, 2003.
- [3] C. Liu, C. Capjack, and W. Rozmus, "3-D simulation of light scattering from biological cells and cell differentiation," *Journal of Biomedical Optics*, vol. 10, no. 1, pp. 014007.1–014007.12, 2005.
- [4] M. Kerker, *The Scattering of Light and other Electromagnetic Radiation*, Academic Press, 1969.
- [5] H. C. van-de-Hulst, *Light Scattering by Small Particles*, Dover, New York, NY, USA, 1981.
- [6] C. F. Bohren and D. R. Huffman, *Absorption and Scattering of Light by Small Particles*, John Wiley & Sons, New York, NY, USA, 1983.
- [7] E. J. McCartney, *Optics of the Atmosphere*, John Wiley & Sons, New York, NY, USA, 1976.
- [8] M. I. Mishchenko, J. W. Hovenier, and L. D. Travis, *Light Scattering by Nonspherical Particles: Theory, Measurements, and Applications*, Academic press, 2000.
- [9] A. Brunsting and P. F. Mullaney, "Light scattering from coated spheres: model for biological cells," *Applied Optics*, vol. 11, no. 3, pp. 675–680, 1972.
- [10] R. Bhandari, "Scattering coefficients for a multilayered sphere: analytic expressions and algorithms," *Applied Optics*, vol. 24, no. 13, pp. 1960–1967, 1985.
- [11] N. G. Volkov and V. Y. Kovach, "Scattering of light by inhomogeneous spherically symmetrical aerosol particles," *Izvestiya Atmospheric and Oceanic Physics*, vol. 26, no. 5, pp. 381–385, 1990.
- [12] L. Kai and P. Massoli, "Scattering of electromagnetic plane waves by radially inhomogeneous spheres: a finely stratified sphere model," *Applied Optics*, vol. 33, no. 3, pp. 501–511, 1994.
- [13] A. Zharinov, P. Tarasov, A. Shvalov, K. Semyanov, D. R. van Bockstaele, and V. Maltsev, "A study of light scattering of mononuclear blood cells with scanning flow cytometry," *Journal of Quantitative Spectroscopy and Radiative Transfer*, vol. 102, no. 1, pp. 121–128, 2006.
- [14] A. Taflove and S. C. Hagness, *Computational Electrodynamics: the Finite-Difference Time-Domain Method*, Artech House, 2nd edition, 2000.
- [15] D. M. Sullivan, *Electromagnetic Simulation Using the FDTD Method*, John Wiley & Sons, IEEE, New York, NY, USA, 2000.
- [16] A. Z. Elsherbeni and V. Demir, *The Finite-Difference Time-Domain Method for Electromagnetics with MATLAB Simulation*, Scitech, 2009.
- [17] R. Drezek, A. Dunn, and R. Richards-Kortum, "Light scattering from cells: finite-difference time-domain simulations and goniometric measurements," *Applied Optics*, vol. 38, no. 16, pp. 3651–3661, 1999.
- [18] X. Su, K. Singh, W. Rozmus, C. Backhouse, and C. Capjack, "Light scattering characterization of mitochondrial aggregation in single cells," *Optics Express*, vol. 17, no. 16, pp. 13381–13388, 2009.
- [19] S. Tanev, W. Sun, J. Pond et al., "FDTD simulation of light interaction with cells for diagnostics and imaging in nanobiophotonics," in *Handbook of Photonics for Biomedical Science*, Medical physics & biomedical engineering, CRC Press, Taylor & Francis, 2011.
- [20] S. Tanev, Wenbo Sun, J. Pond et al., "Optical imaging of cells with gold nanoparticle clusters as light scattering contrast agents: a finite difference time domain approach to the modeling of flow cytometry configurations," in *Advanced Optical Flow Cytometry*, pp. 35–62, 2010.
- [21] P. J. Wyatt, "Scattering of electromagnetic plane waves from inhomogeneous spherically symmetric objects," *Physical Review*, vol. 127, no. 5, pp. 1837–1843, 1962.
- [22] B. R. Johnson, "Light scattering by a multilayer sphere," *Applied Optics*, vol. 35, no. 18, pp. 3286–3296, 1996.
- [23] A. Y. Perelman, "Scattering by particles with radially variable refractive indices," *Applied Optics*, vol. 35, no. 27, pp. 5452–5460, 1996.
- [24] M. R. Spiegel, *Schaum's Mathematical Handbook of Formulas and Tables*, McGraw Hill, 1968.
- [25] M. Abramowitz and I. A. Stegun, *Handbook of Mathematical Functions*, Dover, New York, NY, USA, 1972.
- [26] I. K. Ludlow and J. Everitt, "Systematic behavior of the Mie scattering coefficients of spheres as a function of order," *Physical Review E*, vol. 53, no. 3, pp. 2909–2924, 1996.

- [27] G. Chliveros and M. A. Rodrigues, *MATLAB Implementation of the Exact Solution for the n-Layer Sphere Problem*, Materials & Engineering Research Institute, Sheffield Hallam University, 2004.
- [28] W. J. Wiscombe, "Improved Mie Scattering Algorithms," *Applied Optics*, vol. 19, no. 9, pp. 1505–1509, 1980.
- [29] A. Dunn, *Light Scattering Properties of Cells*, University of Texas at Austin, Austin, Texas, 1997.
- [30] P. L. Gourley, J. K. Hendricks, A. E. McDonald et al., "Ultrafast nanolaser flow device for detecting cancer in single cells," *Biomedical Microdevices*, vol. 7, no. 4, pp. 331–339, 2005.
- [31] E. N. Marieb and K. Hoehn, *Human Anatomy & Physiology*, Pearson Education, 2007.
- [32] R. Barer and S. Joseph, "Refractometry of living cell part I: basic principles," *Quarterly Journal of Microscopical Science*, vol. 95, no. 4, pp. 399–423, 1954.
- [33] A. Brunsting and P. F. Mullaney, "Differential light scattering from spherical mammalian cells," *Biophysical Journal*, vol. 14, no. 6, pp. 439–453, 1974.
- [34] D. Zink, A. H. Fischer, and J. A. Nickerson, "Nuclear structure in cancer cells," *Nature Reviews Cancer*, vol. 4, no. 9, pp. 677–687, 2004.

## Research Article

# Dual-Source Swept-Source Optical Coherence Tomography Reconstructed on Integrated Spectrum

Shoude Chang, Youxin Mao, and Costel Flueraru

*Institute for Microstructural Sciences, National Research Council Canada, 1200 Montreal Rd, Ottawa, ON, Canada K1A 0R6*

Correspondence should be addressed to Shoude Chang, Shoude.chang@nrc.ca

Received 26 July 2011; Accepted 9 August 2011

Academic Editor: Nanguang Chen

Copyright © 2012 Shoude Chang et al. This is an open access article distributed under the Creative Commons Attribution License, which permits unrestricted use, distribution, and reproduction in any medium, provided the original work is properly cited.

Dual-source swept-source optical coherence tomography (DS-SSOCT) has two individual sources with different central wavelengths, linewidth, and bandwidths. Because of the difference between the two sources, the individually reconstructed tomograms from each source have different aspect ratio, which makes the comparison and integration difficult. We report a method to merge two sets of DS-SSOCT raw data in a common spectrum, on which both data have the same spectrum density and a correct separation. The reconstructed tomographic image can seamlessly integrate the two bands of OCT data together. The final image has higher axial resolution and richer spectroscopic information than any of the individually reconstructed tomography image.

Optical coherence tomography (OCT) is a powerful imaging technology for producing high-resolution cross-sectional images of the internal microstructure of materials and/or biological samples. It has been widely used in medical imaging and biological testing for more than ten years [1–4]. Swept-source optical coherence tomography (SS-OCT) [5, 6] has significant signal-to-noise ratio and speed advantages over time-domain OCT [7–9], in which, the broadband laser swept source plays an important role. The linewidth and output power of the source determinate the imaging depth and sensitivity of an SS-OCT system. The bandwidth of the light source determine the imaging axial resolution. At current stage, most commercial available swept sources have a bandwidth about 100 nm corresponding to an axial resolution around 7.4  $\mu\text{m}$  in air.

In some medical applications, when spectral feature appears at a wavelength differing from the central wavelength of the light source or the photo sensor, it could not be investigated by the single-band OCT system. In order to extract more spectral information and enhance the axial resolution, simultaneously imaging at two distinct spectral regions has been demonstrated by time-domain [10], full-field [11], and spectral-domain [12, 13] OCT systems. Actually, in all the reported dual-band OCT systems, the two sets of band data are produced from the same light source. In time-domain OCT, as the depth information is obtained by

means of depth scanning, both the reconstructed images of different bands have the same image dimensions. An effective and practical method for resolution enhancement in dual-beam time-domain OCT had been reported by Baumgartner et al. [14]. For the spectral-domain OCT, as two bands data produced by the same source, the imaging ranges also have the same depth range, if the spectrum data densities of those two bands (associated with linear CCD array, grating device) are the same.

In SS-OCT, the swept source stimulates the OCT system by a series of wavelengths in a time sequence; a photo detector then collects all the responses as Fourier series components of the testing sample. Because the detector is only sensitive to optical power, it loses the phase information in the reflected/back scattered signal. At any moment, the signal detected by sensor can be written as

$$I(k_i) \approx [E_0(k_i) + H(k_i)E_0(k_i)] \times [E_0(k_i) + H(k_i)E_0(k_i)]^*, \quad i = 1, 2, 3, 4, \dots, N, \quad (1)$$

where  $E_0(k_i)$  is the electrical field with  $i_{\text{th}}$  wavenumber sent from the source,  $H(k_i)$  represents the sample transfer function, and  $I(k_i)$  is the signal generated by the sensor.  $[ ]^*$  indicates conjugate, and  $N$  is the total number of the wavenumbers. Assuming  $P_{(k_i)} = |E_0(k_i)|^2$ , power spectrum

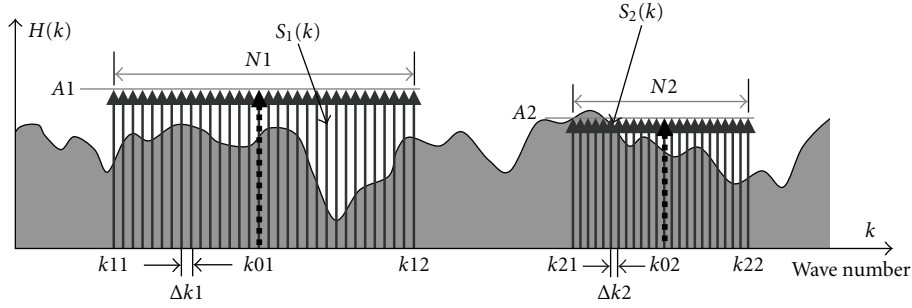


FIGURE 1: Spectrum of two swept sources,  $S_1(k)$  and  $S_2(k)$ , with different parameters: central wavelength ( $k_{01}$ ,  $k_{02}$ ); impulse interval ( $\Delta k_1$ ,  $\Delta k_2$ ); impulse intensity ( $A_1$ ,  $A_2$ ).

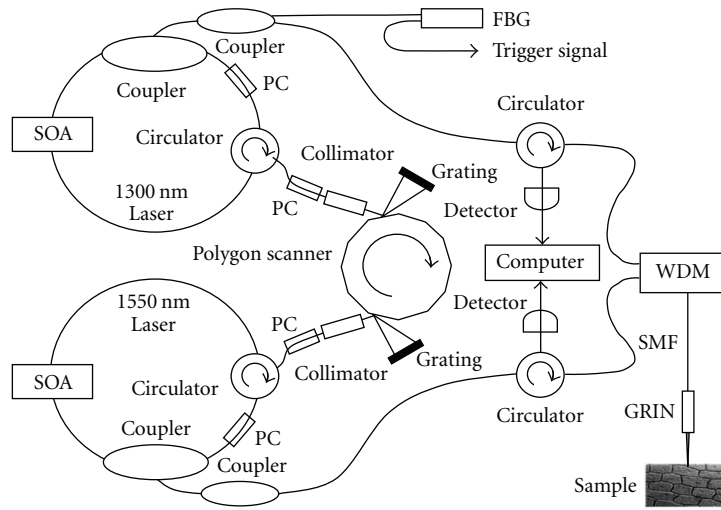


FIGURE 2: Schematic diagram of the dual-source swept-source OCT system. PC: polarization controllers, FBG: fiber Brag grating. SOA: semiconductor optical amplifiers; WDM: wavelength division multiplex; SMF: single-mode optical fiber.

of the light source, the output of OCT system can be expressed by

$$I_{(k_i)} = P_{(k_i)}H^2(k_i) + 2P_{(k_i)}\text{Re}[H(k_i)] + P_{(k_i)}. \quad (2)$$

$\text{Re}[H]$  represents the real part of  $H$ . Assuming  $P(k_i)$  is an ideal source which has a constant distribution and  $H^2(k_i)$  is low frequency component that could be ignored, the processed  $I(k_i)$  becomes

$$I_p(k_i) \propto \text{Re}[H(k_i)]. \quad (3)$$

The reconstruction of the sample in spatial domain (depth  $z$ ) is performed by an inverse Fourier transform:

$$h(z) = \text{IFT} \left[ I_p(k_i) \right]. \quad (4)$$

Because  $h(z)$  is the inverse Fourier transform of a real function, it contains a mirror portion. Many works have been done to remove this artifact [15]. The nature of these works is actually to make the intensity signal a complex signal. At any time moment, as (3) and (4) are the results from one

wavelength, when all the  $I_p(k_i)$ s with different wavenumbers form a sequence, the internal structure of the sample can then be extracted by

$$h(z) = \text{IFT}[\sum_n H(k_i)\delta(k_i - n)], \quad (5)$$

where unit impulse function  $\delta(k_i - n)$  is used to separate all Fourier series components with discrete  $k$  numbers.

In SS-OCT, each wavelength independently makes its contribution to the reconstruction as a Fourier series component. This feature gives SS-OCT a possibility to increase the bandwidth by combining multiple swept sources that have different central wavelengths. Figure 1 shows two swept sources,  $S_1(k)$  and  $S_2(k)$ , with different parameters: central wavelengths or wave numbers ( $k_{01}$ ,  $k_{02}$ ); spectral-line interval ( $\Delta k_1$ ,  $\Delta k_2$ ); impulse intensity ( $A_1$ ,  $A_2$ ). Spectral-line interval is given by the sweeping speed of the source and sampling rate of the interface. Impulse intensity is given by the output power of the source.

We have built a dual-source SS-OCT system, which is illustrated in Figure 2 [16]. This OCT system consists of

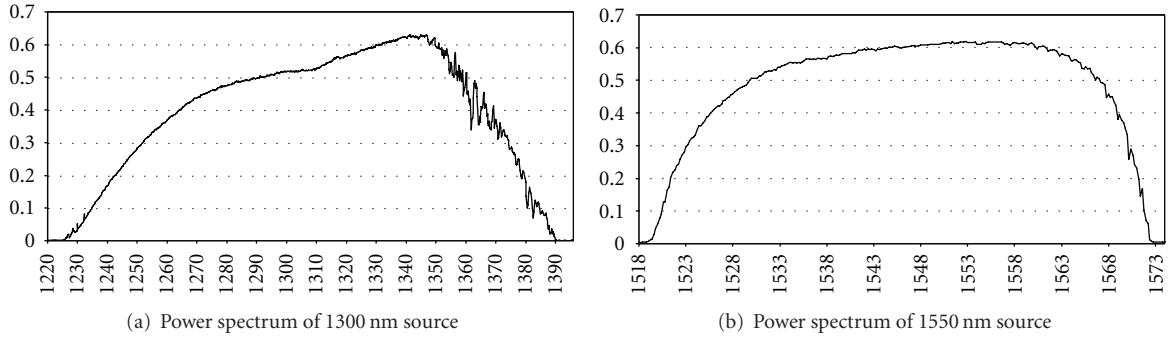


FIGURE 3: Power spectrums of (a) 1300 nm swept source; (b) 1550 nm swept source.

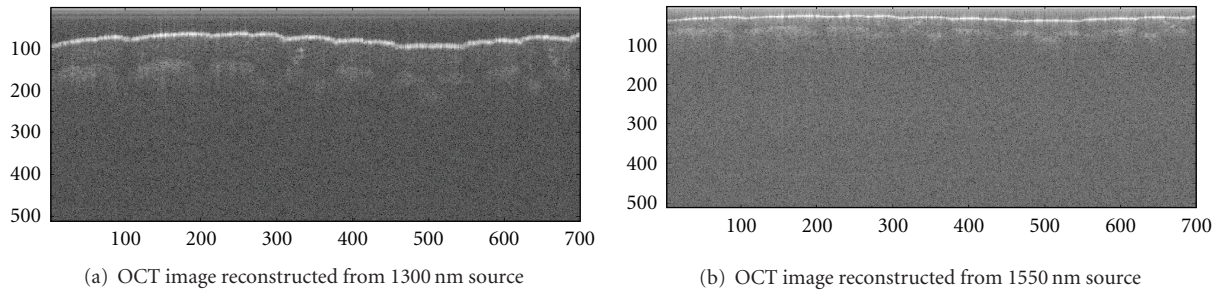


FIGURE 4: OCT images of a finger. (a) Reconstructed by 1300 nm swept source; (b) reconstructed by 1550 nm swept source.

two synchronized swept sources, a wavelength-division multiplexing, and a sharing common path fiber-lensed probe. The dual swept source comprises of two extended ring cavity semiconductor lasers and two high-speed optical narrow-band intracavity filters with a single polygonal scanner. The rotating polygon scanner simultaneously tunes the two wavelengths of two lasers synchronously. Two broadband semiconductor optical amplifiers (SOAs) at 1310 nm 1550 nm central wavelengths were used as the cavity gain medium. The inline miniature polarization controller (PC) can reduce cavity lengths. The ratio of the output coupler of 60/40 was used (60% of the power is coupled out) for both cavities, while a 10% output power of 1310 nm band was connected to a fiber Bragg grating (FBG) the swept trigger signal. The simultaneous swept laser outputs in 1310 and 1550 nm bands were connected to two matched optical circulators and then connected to a broadband 1310/1550 WDM that outputs two sources into a single-mode optical fiber (SMF). The SMF was fusion-spliced with a home-made GRIN focused lens. The light reflected from the glass-air surface of the GRIN lens, as a reference arm, together with the light reflected from inside sample forms a common-path configuration [17].

The power spectrums of two swept sources are shown in Figures 3(a) and 3(b), and two corresponding OCT images obtained from a human finger are shown in Figures 4(a) and 4(b). It is obvious that two OCT images have different aspect ratios in the imaging depth. In order to merge two OCT images together, one image has to be extended to the same dimension as the other one. One possible way is to find the imaging-depth ratio (IDR) of the two images by comparing two depth ranges of lasers. For a swept source

with a Gaussian-profile spectral envelope, the depth range  $\Delta z$  is given by [18],

$$\Delta z = \frac{\lambda_0^2 N_s}{(4n\Delta\lambda)}, \quad (6)$$

where  $\lambda_0$  is the central wavelength of the swept source,  $\Delta\lambda$  is the full-width at half-maximum (FWHM) of the spectral envelope (tuning range),  $N_s$  is the number of samples within FWHM range of the  $\Delta\lambda$ , and  $n$  is the group refractive index of the sample.

It is difficult and inaccurate to determine the  $\Delta\lambda$  by measuring FWHM of the spectrum, when the shape of the spectrum is irregular rather than a Gaussian profile. For example, if the profile slope at the half-maximum position is very low, a small change of the amplitude may introduce a very large change of  $\Delta\lambda$  value. As a matter of fact, the IDR of the two sources based on  $\Delta\lambda$ s calculated by FWHM does not reflect the real IDR of two reconstructed OCT images due to the inaccurately measured  $\Delta\lambda$ s. In order to find the real IDR of two sources, we made a simple experiment with the DS-SSOCT system. A small mirror is placed directly in front of the common path probe, and then the number of the interference fringe peaks in OCT signal of each source is counted. The ratio between two numbers represents the IDR of two OCT images.

For the system used in our experiments, the interference peak number from 1300 nm source is 45, and peak number from 1550 nm source is 18. Therefore, the IDR is 2.5. To verify this method, we have used a testing sample which has 4-layer glass slice. The A-scan OCT images obtained by

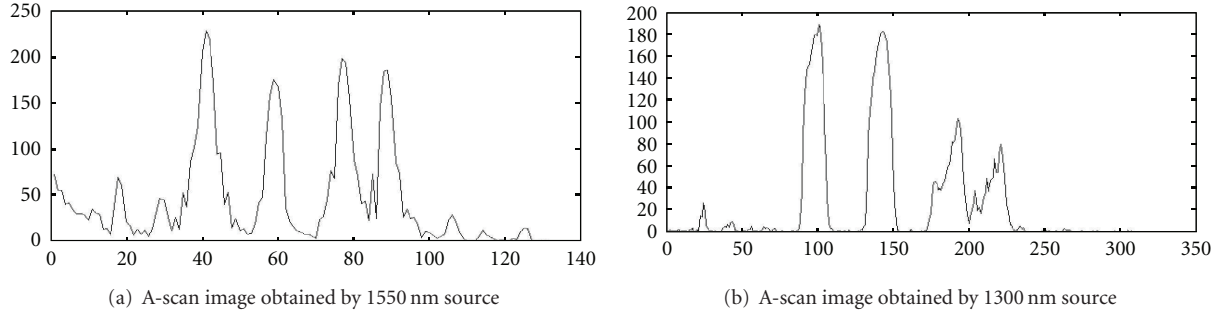


FIGURE 5: A-scan OCT images of a 4-layer glass sample. (a) A-scan image obtained by 1550 nm source; (b) A-scan image obtained by 1300 nm source.

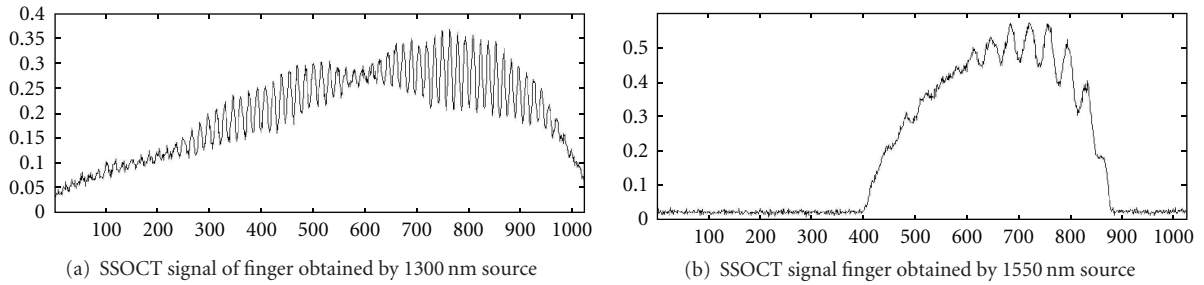


FIGURE 6: Raw SSOCT signals of finger. (a) SSOCT signal of finger obtained by 1300 nm source; (b) SSOCT signal finger obtained by 1550 nm source.

1550 nm source and 1300 nm source are shown in Figures 5(a) and 5(b), respectively. The IDRs of four-peak positions between Figures 5(a) and 5(b) are given by  $R1 = 101/41 \cong 2.5$ ;  $R2 = 143/59 \cong 2.4$ ;  $R3 = 193/77 \cong 2.5$ ;  $R4 = 221/89 \cong 2.5$ . Averagely, we take the IDR as 2.5.

As mentioned above, SS-OCT has capability to increase the bandwidth by combining multiple swept sources that have different central wavelengths. The integrated dual-source SS-OCT spectrum is given by

$$I(kc) = a_1 S'_1(kc)H(kc) + a_2 S'_2(kc)H(kc), \quad (7)$$

where  $kc$  is the new  $k$  scale in the integrated discrete spectrum, and  $S'_1(kc)$ ,  $S'_2(kc)$  are scaled  $S_1(k)$ ,  $S_2(k)$ , in the newly integrated spectrum. In order to adjust contribution of each source, the coefficients  $a_1$ ,  $a_2$  are introduced for each source.

According to the spatial-spectral scaling property of Fourier transform, to reduce the size in spatial domain, the size in spectral domain must be increased. For the DS-SSOCT described above, considering the IDR is 2.5, the SSOCT signal obtained by 1300 nm source should be scaled up by a factor 5, and the SSOCT signal from 1550 nm should be scaled up by a factor of 2. Here, to scale up a spectrum by a factor  $s$  means to zero-padding  $s-1$  zero/s between two neighboring spectral lines. Figures 6 and 7 show the SSOCT signals before and after spectrum scale changes. In Figures 6(a) and 6(b), the spectrums of the two SSOCT signals have different spectral densities: 160 nm/1024 points and 50 nm/480 points for 1300 source and 1550 source, respectively. Figures 7(a) and 7(b) have

been scaled up, so they have the same spectrum density, that is, the same wavelength difference  $\Delta w$  per interval  $\Delta kc$  in the integrated spectrum. Therefore, their reconstructed images have the same depth dimensions. The  $\Delta w$  per  $\Delta kc$  can be easily calculated by the ending wavelength  $w_e$  and starting wavelength  $w_s$  as well as the total spectral lines  $n_s$  in each source:  $\Delta w = |w_e - w_s|/n_s$ . The total spectral separation between two SSOCT signals in the integrated spectrum is given by:  $n_p = |w_{1e} - w_{2s}|/\Delta w$ , where  $w_{1e}$  and  $w_{2s}$  are ending wavelength of SSOCT from source number 1 and starting wavelength of SSOCT from source number 2, respectively.

In the DS-SSOCT described above, for the source number 1, 1300 nm swept source,  $\Delta w = 162 \text{ nm}/1024$  points (see Figure 3); hence, spectral lines per nm is 6.3. The wavelength separation between two bands: 1550 nm – 1300 nm = 250 nm. Considering the scale-up factor of 1300 nm source is 5, the separation spectral lines between two source signals:  $250 \times 6.3 \times 5 = 7875$  points. Figure 8 shows the integrated spectrum of the DS-SSOCT signal  $I(kc)$ , where the  $a_1 = a_2 = 1$ , as defined in (7). The final reconstructed OCT image is obtained by

$$h(z) = \log(|\text{Trunc}\{\text{IFT}[I(kc)]\}|), \quad (8)$$

where  $\text{IFT}[\ ]$  denotes inverse Fourier transform,  $\text{Trunc}$  means that, in the reconstructed OCT image, only the central piece of (2) is kept, and all other mirror pieces are truncated off, while  $\log(\ )$  is logarithm processing to nonlinearly emphasize the subtle details.

Figure 9 shows the reconstructed OCT image from the integrated spectrum. Two parts of the SSOCT signals are

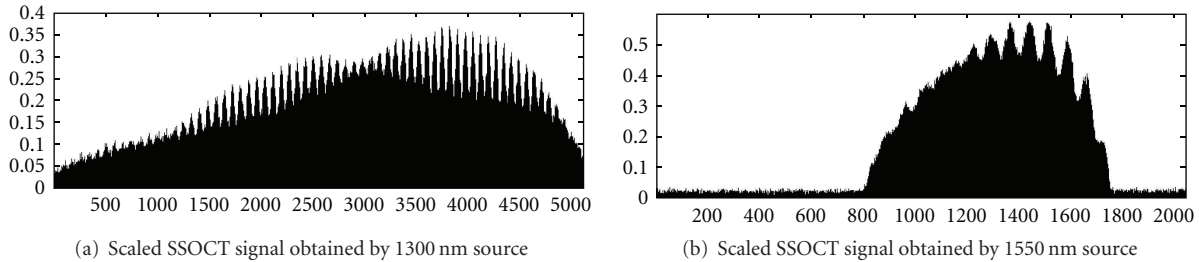


FIGURE 7: Scaled SSOCT signals of Figure 6. (a) scaled SSOCT signal obtained by 1300 nm source; (b) scaled SSOCT signal obtained by 1550 nm source.

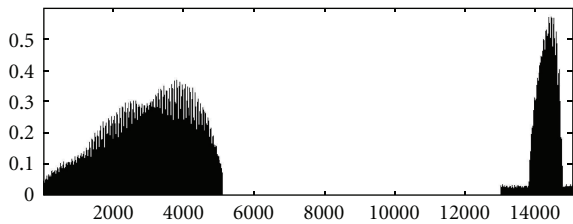


FIGURE 8: Integrated SSOCT signals obtained from two swept sources.

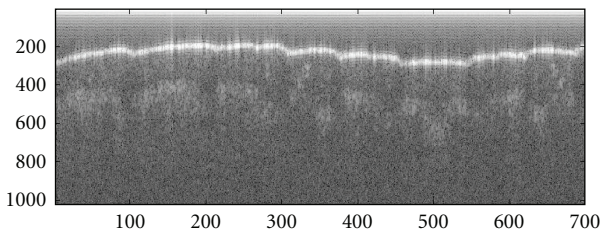


FIGURE 9: OCT image reconstructed from integrated spectrum.

seamlessly integrated together, which has richer spectrum information and depth resolution than any of the individually reconstructed OCT image, since the integrated spectrum has broader bandwidth than other individual two.

In this paper, a new method for integrating the SSOCT signals produced by a dual-source swept-source OCT system is proposed. The resulting OCT image based on the integrated spectrum contains richer spectral and resolution information than any of the individually reconstructed OCT images. This method can be extended to multiple sources of the synchronized swept-source OCT system.

## References

- [1] D. Huang, E. A. Swanson, C. P. Lin et al., "Optical coherence tomography," *Science*, vol. 254, no. 5035, pp. 1178–1181, 1991.
- [2] W. Drexler and J. G. Fujimoto, *Optical Coherence Tomography, Technology and Applications*, Springer, Berlin, Germany, 2008.
- [3] G. Smolka, *Optical Coherence Tomography: Technology, Markets, and Applications 2008–2012*, BioOptics World, Penn Well Corporation, 2008.
- [4] U. Morgner, W. Drexler, F. X. Kärtner, X. D. Li et al., "Spectroscopic optical coherence tomography," *Optics Letters*, vol. 25, no. 2, pp. 111–113, 2000.
- [5] S. R. Chinn, E. A. Swanson, and J. G. Fujimoto, "Optical coherence tomography using a frequency-tunable optical source," *Optics Letters*, vol. 22, no. 5, pp. 340–342, 1997.
- [6] S. H. Yun, G. J. Tearney, J. F. De Boer, N. Iftimia, and B. E. Bouma, "High-speed optical frequency-domain imaging," *Optics Express*, vol. 11, no. 22, pp. 2953–2963, 2003.
- [7] M. A. Choma, M. V. Sarunic, C. Yang, and J. A. Izatt, "Sensitivity advantage of swept source and Fourier domain optical coherence tomography," *Optics Express*, vol. 11, no. 18, pp. 2183–2189, 2003.
- [8] J. F. De Boer, B. Cense, B. H. Park, M. C. Pierce, G. J. Tearney, and B. E. Bouma, "Improved signal-to-noise ratio in spectral-domain compared with time-domain optical coherence tomography," *Optics Letters*, vol. 28, no. 21, pp. 2067–2069, 2003.
- [9] R. Leitgeb, C. K. Hitzenberger, and A. F. Fercher, "Performance of Fourier domain vs. time domain optical coherence tomography," *Optics Express*, vol. 11, no. 8, pp. 889–894, 2003.
- [10] F. Spöler, S. Kray, P. Grychtol et al., "Simultaneous dual-band ultra-high resolution optical coherence tomography," *Optics Express*, vol. 15, no. 17, pp. 10832–10841, 2007.
- [11] D. Sacchet, J. Moreau, P. Georges, and A. Dubois, "Simultaneous dual-band ultra-high resolution full-field optical coherence tomography," *Optics Express*, vol. 16, no. 24, pp. 19434–19446, 2008.
- [12] S. Kray, F. Spöler, M. Forst, and H. Kurz, "High-resolution simultaneous dual-band spectral domain optical coherence tomography," *Optics Letters*, vol. 34, no. 13, pp. 1970–1972, 2009.
- [13] P. Cimalla, J. Walther, M. Mehner, M. Cuevas, and E. Koch, "Simultaneous dual-band optical coherence tomography in the spectral domain for high resolution in vivo imaging," *Optics Express*, vol. 17, no. 22, pp. 19486–19500, 2009.
- [14] A. Baumgartner, C. K. Hitzenberger, H. Sattmann, W. Drexler, and A. F. Fercher, "Signal and resolution enhancements in dual beam optical coherence tomography of the human eye," *Journal of Biomedical Optics*, vol. 3, no. 1, pp. 45–54, 1998.
- [15] M. V. Sarunic, M. A. Choma, C. Yang, and J. A. Izatt, "Instantaneous complex conjugate resolved spectral domain and swept-source OCT using 3×3 fiber couplers," *Optics Express*, vol. 13, no. 3, pp. 957–967, 2005.
- [16] Y. Mao, S. Chang, E. Murdock, and C. Flueraru, "Simultaneous dual-wavelength-band swept source and dual-band common-path optical coherence tomography," *Optics Letters*, vol. 36, pp. 1990–1992, 2011.

- [17] J. Zhang, B. Rao, L. Yu, and Z. Chen, "High-dynamic-range quantitative phase imaging with spectral domain phase microscopy," *Optics Letters*, vol. 34, no. 21, pp. 3442–3444, 2009.
- [18] F. Lexer, C. K. Hitzenberger, A. F. Fercher, and M. Kulhavy, "Wavelength-tuning interferometry of intraocular distances," *Applied Optics*, vol. 36, no. 25, pp. 6548–6553, 1997.